Synthesis and Characterisation of Zinc Gallate Based Phosphors for Thin Film Electroluminescent Devices

Thesis submitted to
COCHIN UNIVERSITY OF SCIENCE AND TECHNOLOGY
in partial fulfillment of the requirements
for the award of the degree of
DOCTOR OF PHILOSOPHY

Mini Krishna K

Department of Physics
Cochin University of Science and Technology
Cochin - 682 022, Kerala, India

May 2008

Synthesis and Characterisation of Zinc Gallate Based Phosphors for Thin Film Electroluminescent Devices

Ph.D thesis in the field of Materials Science

Author:

Mini Krishna K
Optoelectronic Devices Laboratory
Department of Physics
Cochin University of Science and Technology
Cochin - 682 022, Kerala, India
Email: minikrishna@gmail.com

Supervisor:

Dr. M.K. Jayaraj
Reader
Optoelectronics Device Laboratory
Department of Physics
Cochin University of Science and Technology
Cochin – 682 022, Kerala, India
Email: mkj@cusat.ac.in

Front cover: Zinc gallate spinel structure
Back cover: Photo of the electroluminescent device fabricated

May 2008

Dr. M.K. Jayaraj
Reader
Department of Physics
Cochin University of Science and Technology
Cochin - 682 022

21st May 2008

Certificate

Certified that the work presented in this thesis entitled "*Synthesis and Characterisation of Zinc Gallate Based Phosphors for Thin Film Electroluminescent Devices*" is based on the authentic record of research carried out by Ms. Mini Krishna K under my guidance in the Department of Physics, Cochin University of Science and Technology, Cochin - 682 022 and has not been included in any other thesis submitted for the award of any degree.

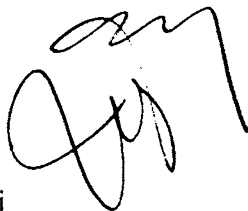

Dr. M. K. Jayaraj
(Supervising Guide)

Phone : +91 484 2577404 extn 33 Fax: 91 484 2577595 email: mkj@cusat.ac.in

Declaration

Certified that the work presented in this thesis entitled "*Synthesis and Characterisation of Zinc Gallate Based Phosphors for Thin Film Electroluminescent Devices*" is based on the original research work done by me under the supervision and guidance of Dr. M. K. Jayaraj, Reader, Department of Physics, Cochin University of Science and Technology, Cochin - 682 022 and has not been included in any other thesis submitted previously for the award of any degree.

Cochin - 22
21st May 2008

Mini Krishna K

Dedicated to my teachers and friends

Acknowledgements

I am deeply indebted to my guide, Dr. M. K. Jayaraj, for sharing his expertise and knowledge with me throughout these years of learning at CUSAT. In spite of his responsibilities and duties, he had the patience to share his valuable time with us, indulging in discussions and coming up with stimulating suggestions. I wish to express my deepest sense of gratitude and respect towards him for the forbearance, timely advice, constant encouragement, selfless support and inspiration that he extended towards me throughout. I heartfully thank him for making it possible for me the successful completion of this work.

I am deeply obliged to my teachers for their encouragement, inspiration and timely advice. I am greatful to Sr. Ritty for introducing me to the research atmosphere at CUSAT.

I would like to express my sincere gratitude to Prof. Godfrey Louis, Head of the Department and all the former Heads of the Department - Prof. K. P. Vijayakumar, Prof. V. C. Kuriakose and Prof. Ramesh Babu Thayyullathil - for permitting me to use the facilities. I also greatfully acknowledge the help and inspiration from all the other faculty members of the Department of Physics.

I am thankful to all the office and library staff of the Department of Physics and the technical staff at USIC for all the help and cooperation.

I am thankful to CSIR for financially assisting me during this endeavour.

I remember with gratitude the sincere support of Dr. Aldrin, Dr. Manoj and Dr. Nisha for all the guidance offered during the initial stages of my research.

I specially appreciate my dear friend Anoop for his sincere support and fruitful discussions during my research work.

I would like to express my sincere appreciation to my colleagues in the OED lab Reshmi, Saji, Ajimsha, Asha, Rahana, Vanaja Madam, Anila teacher, Joshy Sir, James Sir, Aneesh, Arun, Ratheesh, Krishna prasad and Sreeja for all the help they had extended.

I treasure my friendship with Vineetha, Ragitha, Maneesh chandran, Sukesh, Sarath, Manu, Sanjay, Veena Gopalan whom I got acquainted with at CUSAT.

I remember with gratitude the love expressed by my friends Sunisha, Ashitha and Soumya in every endeavour of mine from my college days.

I record my deep and utmost gratitude to my parents for their selfless support, encouragement, patience and tolerance during the entire period of my research work.

I remember with love my dear brother for motivating and encouraging me to pursue a science career in life.

I am greatly indebted for the love and support shown by my relatives-in-law.

I record my love and gratitude towards my husband Raghunath for being there for me always. My special appreciation and love towards my son Pranav for his patience.

Finally I thank all my well wishers…

I am thankful to God Almighty for benevolently showering upon me this blessing in life.

Mini Krishna K

Contents

Preface i

Chapter 1 – A general introduction

1.1. Introduction 11
1.2. The phenomenon of photoluminescence (PL) 11
1.2.1. Basic concepts 11
1.2.2. Intrinsic luminescence 14
1.2.2a. Band-to-band luminescence 14
1.2.2b. Exciton luminescence 14
1.2.2c. Cross luminescence 15
1.2.3. Extrinsic luminescence 16
1.2.3a. Unlocalized type 16
1.2.3b. Localized type 16
1.2.4. Energy transfer in luminescence: sensitization 18
1.2.4a. Emission-reabsorption 20
1.2.4b. Resonance radiationless energy transfer 21
1.2.4c. Non-resonance radiationless energy transfer 22
1.2.5. Concentration quenching (Self-quenching) 22
1.3. The phenomenon of electroluminescence (EL) 23
1.4. ACTFEL devices 24
1.4.1. ACTFEL device structure 28
1.4.2. The ideal model 31
1.4.3. ACTFEL device physics 32
1.4.3a. Electron injection 34
1.4.3b. High-field charge transport 35
1.4.3c. Impact excitation/ionization 37
1.4.3d. Electron capture 37
1.4.3e. Radiative de-excitation 38
1.4.3f. Radiative outcoupling 39
1.4.4. Space charge effects 40
1.4.5. Material requirements for ACTFEL devices 43
1.4.5a. Substrate 43
1.4.5b. Electrodes 44
1.4.5c. Insulating layer 46
1.4.5d. Phosphor layer 47
1.5. Oxide phosphors 50

1.6. White phosphors 53
1.7. The $ZnGa_2O_4$ phosphor system - a review 55
1.8. Relevance of the present work 62
References 62

Chapter 2 – Experimental and analytical techniques

2.1. Introduction 75
2.2. Bulk synthesis 76
2.3. Thin film growth techniques 78
2.3.1. Thermal evaporation by resistive heating 79
2.3.2. Sputtering 80
2.3.3. Pulsed laser deposition (PLD) 87
2.4. Device fabrication 94
2.5. Characterization tools 94
2.5.1. Thin film thickness 95
2.5.2. Structural characterization 96
2.5.3. Morphological analysis 98
2.5.3a. Scanning electron microscope (SEM) 98
2.5.3b. Atomic force microscopy (AFM) 100
2.5.4. Compositional analysis 103
2.5.4a. Energy dispersive x-ray (EDX) analysis 103
2.5.4b. X-ray fluorescence (XRF) analysis 105
2.5.5. Optical studies 106
2.5.5a. Determination of band gap energy 106
2.5.5b. Photoluminescence (PL) 109
2.5.5c. Color characterization 111
2.5.6. Device characterization 115
2.5.6a. Luminance-Voltage (L-V) characterization 116
References 120

Chapter 3 – Growth of $ZnGa_2O_4$ phosphor thin films by pulsed laser ablation

3.1. Introduction 125
3.2. Experimental 126
3.3. Room temperature deposition of crystalline $ZnGa_2O_4$ thin films 128
3.4. Effect of post-deposition annealing in air 136

3.5. Conclusion 142
References 143

Chapter 4– Synthesis of a novel white oxide phosphor: $ZnGa_2O_4:Dy^{3+}$

4.1. Introduction 149
4.2. Experimental 150
4.3. Results and discussion 151
4.4. Conclusions 167
References 167

Chapter 5 – Growth of RF magnetron sputtered $ZnGa_2O_4:Dy^{3+}$ thin films

5.1. Introduction 173
5.2. Experimental 174
5.3. Results and discussion 175
5.4. Conclusions 186
References 187

Chapter 6 – Fabrication of $ZnGa_2O_4:Dy^{3+}$ active ACTFEL devices on glass substrate

6.1. Introduction 193
6.2. Experimental 194
6.3. Results and discussion 197
6.3.1. Glass/ITO/ATO/ $ZnGa_2O_4:Dy^{3+}$/BTO/Al TFEL device 199
6.3.2. Glass/ITO/ATO/ZnO/$ZnGa_2O_4:Dy^{3+}$/BTO/Al TFEL device 205
6.3.3. Effect of the presence of the ZnO interfacial layer 209
6.4. Conclusions 212
6.5. References 212

Chapter 7 – Summary and future recommendations

7.1. Summary 219
7.2. Recommendations for future work 223

Preface

The flat panel display (FPD) technology emerged to replace the mature cathode ray tubes (CRTs) in the latter half of the 20th century. The need for a thinner display - physically smaller, more rugged and less power hungry than the venerable CRT - of comparable viewing area with an image quality comparable to that of the CRT ended up in the advent of FPDs. Today, a lot many FPD technologies are commercially available though significant amounts of research and development are still required to match the quality and affordability of the CRT. The FPD applications range from televisions and laptop computers to aircraft cockpits and helmet-mounted displays.

Thin film electroluminescent (TFEL) displays out-perform all other competing FPD's due to the fundamental differences in their technologies. TFEL displays are based on the phenomenon of high field electroluminescence where the luminescent materials emit light on being excited by an externally applied electric field (~10^6 V/cm). They are all solid, emissive display devices with superior characteristics such as fast response, wide viewing angles, high resolution, wide operating temperatures, light weight and good display qualities. These features ensure suitability to high information content flat panel screens of personal computers and workstations. The unique performance and visual characteristics of high performance EL displays make it an ideal solution for the most challenging and demanding applications where other display technologies are simply inadequate. Equipment and system designers use electroluminescent displays to fulfill the growing demands from their customers for improved

image quality, longer lifetime and higher reliability. The solid state emissive nature of EL displays is the unique feature making them relevant for today's embedded display solutions. Their ruggedness renders them the capacity to endure harsh environments making them suiable for medical, military, avionic, automotive and industrial applications.

Oxide phosphors are currently being investigated as better substitues to sulphide phosphors in display applications owing to their chemical and thermal stability. However, the refractory nature of oxide materials prompts one to go for high temperature processing during and/or post-deposition to achieve a high degree of polycrystallinity. This also limits their deposition by simple vacuum evaporation techniques. Moreover, instead of glass substrates, an inverted structure with a high temperature tolerant substrate is usually preferred for the fabrication of oxide phosphor based alternating current thin film electroluminescent (ACTFEL) devices. Therefore, the primary focus of the present study is to check the possibility of growing oxide phosphor thin films on glass substrates. Being a cubic spinel and a versatile phosphor host, zinc gallium oxide - $ZnGa_2O_4$ - has been chosen as the material of investigation. Thin films of zinc gallate based phophors were grown and characterised for EL device applications. Fabrication of an ACTFEL device on glass substrate has also been illustrated. The thesis has been organised into seven chapters.

Chapter 1 presents a brief description on the phenomenon of luminescence, photoluminescence and electroluminescence in particular. The working principle of ACTFEL devices - the phenomenon of high field electroluminescence - has

been presented in detail. The ideal model, structure and material requirements of ACTFEL devices have also been outlined. Remarks have been made on oxide phosphors, white phosphors and in particular on zinc gallium oxide phosphor system.

Chapter 2 describes in detail the thin film growth techniques and characterization tools employed in the present work. Powder phosphors were prepared via high temperature solid state reactions using horizontal tube furnaces. Thin film phosphor growth was accomplished using pulsed laser deposition (PLD) and radio frequency (rf) magnetron sputtering techniques. Structural characterization by x-ray diffraction technique helped in studying the crystallographic properties. Morphological analysis was done by scanning electron microscopy (SEM) and atomic force microscopy (AFM). Compositional analysis was carried out by energy dispersive x-ray analysis (EDX) and x-ray fluorescence (XRF) studies. Band gap investigations were done by recording the diffuse reflectance spectra (DRS) in case of powder samples and the transmission spectra for thin film samples. Photoluminescent (PL) investigations helped to gauge the chromatic identity of the bulk and thin film phosphors prepared. The thicknesses of the films were measured using stylus profilometer. The deposition conditions and the process parameters were optimized based on these characterizations. The best results were assimilated in fabricating an ACTFEL device with an oxide phosphor as the active layer. The luminescence-voltage (L-V) characterization of the device was done by applying trapezoidal pulses from a frequency generator and recording the luminescent output using a photo multiplier tube (PMT).

Chapter 3 deals with the pulsed laser deposition and characterization of $ZnGa_2O_4$ thin films. The present work checks whether it is possible to lower the processing temperature of oxide phosphors retaining their luminescent properties so as to serve as efficient phosphor systems. The zinc gallate target for laser ablation was synthesised in the laboratory by conventional methods. The second harmonic (532 nm) of a Nd:YAG laser was used as the laser source. It was observed that the growth of crystalline films were found to be highly dependent on the deposition parameters like ambient oxygen pressure inside the deposition chamber, duration of deposition, laser power and substrate to target distance. Structural and optical properties of the thin films were analyzed. Post-deposition annealing in air was done with the aim of improving the crystallinity and thereby the luminescent behavior of the as-deposited films. The results do confirm that room temperature deposition of $ZnGa_2O_4$ thin films is possible with PLD. Progressive research in this direction shall contribute to the realization of zinc gallate active ACTFEL devices on low temperature substrates.

Chapter 4 deals with the solid state synthesis of a novel white oxide phosphor, dysprosium (Dy) doped $ZnGa_2O_4$. The dopant concentration was varied in the range 0.25 atomic % to 3 atomic %. The powders synthesized by high temperature solid state reaction were structurally and optically characterized. The analysis of the photoluminescent (PL) emission and excitation (PLE) spectra suggested that white emission from bulk $ZnGa_{2(1-x)}O_4:Dy_{2x}$ samples is due to the host sensitized nonradiative resonant energy transfer via exchange interaction between the host and the activator. A tuning of color from blue to white was possible by varying the dopant content.

Chapter 5 deals with the growth of $ZnGa_2O_4:Dy^{3+}$ films on quartz substrates by rf magnetron sputtering. The deposition parameters such as substrate to target distance, duration of deposition, rf power and Argon flow inside the deposition chamber were optimized at room temperature. The thickness was optimized to lie above 1 μm so that the same layer would give excellent luminescent characteristics if used as the active layer in ACTFEL devices. No luminescence could be observed from the films deposited at room temperature. So the effect of substrate temperature on the structural and luminescent properties of $ZnGa_2O_4:Dy^{3+}$ thin films were investigated. The crystalline behavior, Zn/Ga ratio, and surface morphology of the films were found to be highly sensitive to substrate temperature. Under UV illumination, the as-deposited films at and above 300°C gave white luminescence even without any post-deposition treatments. The white luminescence was attributed to the cumulative effect of multicolor emissions from the luminescence center Dy^{3+} via host sensitization.

Chapter 6 describes the fabrication of ACTFEL devices on glass substrates with $ZnGa_2O_4:Dy^{3+}$ as the active layer. Every layer, except the rear electrode, of the MISIM (metal-insulator-semiconductor-insulator-metal) structured device was an oxide material. Devices were fabricated on commercially available transparent glass substrates - NEG/ITO/ATO (ie., ITO/ATO coated nippon electric glass). The transparent ITO (indium tin oxide) and ATO (aluminium titanium oxide) layers formed respectively the bottom electrode and bottom dielectric of the EL device. The standard MISIM structure of the device was therefore NEG/ITO/ATO/phosphor layer/$BaTa_2O_6$/Al. Devices were fabricated with and without a ZnO buffer layer. The devices gave an EL emission, when

electrically excited by trapezoidal pulses, even without any post-deposition annealing. The white emission resulted from the simultaneous occurrence of multicolor transitions characteristic of the dopant ion. The luminance versus voltage (L-V) curves was measured for a drive frequency of 1.5 KHz. The insertion of the ZnO buffer layer in between the substrate and the active layer was found to enhance the device performance.

Chapter 7 summarizes the main results in the thesis and recommends the scope for future works.

Part of the thesis has been published in internationally referred journals

1. Pulsed laser deposition of $ZnGa_2O_4$ phosphor films, R. Reshmi, **K. Mini Krishna**, R. Manoj and M. K. Jayaraj, *Surf. Coat. Technol.*, **198**, 345 (2005).
2. Host sensitized white luminescence in $ZnGa_2O_4:Dy^{3+}$ phosphor, **K. Mini Krishna**, G. Anoop and M. K. Jayaraj, *J. Electrochem. Soc.*, **154**, J310 (2007).
3. Effect of substrate temperature on the structural and luminescent characteristics of RF magnetron sputtered $ZnGa_2O_4:Dy^{3+}$ thin films, **K. Mini Krishna**, G. Anoop and M. K. Jayaraj, *J. Electrochem. Soc.*, **154**, J379 (2007).
4. White ACTFEL devices on glass substrates using $ZnGa_2O_4:Dy^{3+}$ active layer, **K. Mini Krishna**, G. Anoop and M. K. Jayaraj (to be communicated)

Other publications to which the author has contributed

1. Electrical and optical properties of $ZnGa_2O_4$ thin films deposited by pulsed laser deposition, **K. Mini Krishna**, M. Nisha, R. Reshmi, R. Manoj, A. S. Asha and M. K. Jayaraj, *Mater. Forum*, **29**, 243 (2005).
2. The effect of Mg incorporation on structural and optical properties of $Zn_2GeO_4:Mn$ phosphor, G.Anoop, **K. Mini Krishna** and M. K. Jayaraj, *J.*

Electrochem. Soc., **155**, J7 (2008).

3. Influence of a dopant source on the structural and optical properties of Mn doped $ZnGa_2O_4$ thin films, G. Anoop, **K. Mini Krishna** and M. K. Jayaraj, *Appl. Phys. A*, **90**, 711 (2008).
4. $Mg_{1.96-1.96x}Zn_{1.96x}GeO_4$:$Mn_{0.04}$ phosphors for electroluminescent display applications, G. Anoop, **K. Mini Krishna** and M. K. Jayaraj, *J. Alloys Compd.* (in press). doi: 10.1016/j.jallcom.2008.01.043
5. The effect of ZnO buffer layer on structural and optical properties of RF magnetron sputtered Zn_2GeO_4:Mn^{2+} thin films, G. Anoop, **K. Mini Krishna**, K. Rajeev Kumar and M. K. Jayaraj. (under revision in *J. Electrochem. Soc.*)

Conference proceedings

1. Growth of single phase In_2S_3 films by chalcogenisation of metallic indium films, Rahana Yoosuf, Aldrin Antony, Manoj R, **Mini Krishna**, Nisha M, M.K.Jayaraj, *Proc. DAE Solid State Physics Symposium*, DAE-SSPS '03, p.771, Delhi, India.
2. Alternating current powder electroluminescent device using $ZnGa_2O_4$:Mn phosphor, G. Anoop, **K. Mini Krishna**, R. Reshmi and M. K. Jayaraj, *Proc. Seventh International Conference on Optoelectronics, Fiber Optics and Photonics*, Photonics '04, Kochi, India.
3. Zinc gallate phosphor for electroluminescent device applications, G. Anoop, R. Manoj, M. Nisha, R. Reshmi, **K. Mini Krishna** and M. K. Jayaraj, *Proc. National Conference on Luminescence and its Applications*, NCLA '05, Bangalore, India.
4. Photoluminescent studies in co-sputtered $ZnGa_2O_4$:Mn phosphor thin films, G. Anoop, **K. Mini Krishna** and M. K. Jayaraj, *Proc. Ninth Asian Symposium on Information Display*, ASID '06, p.280, Delhi, India.
5. Red shift in the photoluminescence emission of SrS:Cu, Cl phosphor, E. I. Anila, G. Anoop, **K. Mini Krishna**, I. P. Sanjay Kumar and M. K Jayaraj, *Proc. Eighth International Conference on Optoelectronics, Fiber Optics and Photonics*, Photonics '06, Hyderabad, India.
6. Hydrothermal synthesis and characterization of $ZnGa_2O_4$ nanophosphor, **K. Mini Krishna**, K. Manzoor, P. M. Aneesh and M. K. Jayaraj, *Proc. National Conference on Current Trends in Materials Science*, CTMS '07, p.60, Kottayam, India.

Chapter 1

A general introduction

1.1. Introduction

Luminescence or 'weak glow' [1] is the radiation emitted by a material excessive in comparison to thermal radiation. It results from the transition of an excited electronic state to a ground state or another state lower in energy, the duration of which is much longer than the period of light vibrations (10^{-10} sec). The competing radiationless transitions results from interactions with the lattice or a transfer of energy to other ions. Luminescence, depending on the mode of excitation, is reflected in expressions such as photo-, electro-, chemi-, thermo-, sono-, or triboluminescence. In practice, most often the excitation is via x-rays, cathode rays, or UV emission of a gas discharge. The position of the band in the luminescence spectrum is independent of the method of excitation and is determined only by the interlevel spacing. Two other terms quite often used to classify luminescent materials are fluorescence ($\tau < 10$ ms) and phosphorescence ($\tau > 0.1$ s). As the mechanism of luminescence is associated with the duration of glow, the decay law of luminescence is exponential in fluorescence, and hyperbolic or still more complicated for phosphorescence.

1.2. The phenomenon of photoluminescence (PL)

1.2.1. Basic concepts

The luminescent emission from the mineral barite on exposure to sunlight was identified as 'photoluminescence' (PL) first by Vincenzo Cascariolo. A material photoluminesces when excited by monochromatic light or by UV radiation with

a spectrum broad enough to overlap the ion absorption bands. The phenomenon is pictorially illustrated using either a unidimensional diagram of energy levels (in the form of straight lines) or a bidimensional pattern (energy versus interionic distance) of the same levels in the form of configuration curves [2].

The three elementary processes between an ion's states are: excitation, emission and radiationless transitions. If the interaction between the ion and the lattice is weak, the wavelength of the emission band matches that of the absorption band. For example, the f electrons in trivalent rare-earth (RE^{3+}) ions are shielded from the interactions with the lattice. If the interaction is fairly strong, as in transition metal ions, the emission band shifts towards longer wavelength with respect to the absorption band - a relation known as the empirical Stoke's law [3]. Generally, a rise in the temperature of the system makes it conducive to radiationless transitions and to falling intensity of emission.

Excitation and emission are separated by a time interval ie. by the lifetime of the excited state ($\sim 10^{-8}$ sec or more). This time interval is sufficient for the system to adapt itself to the given excited electronic state which includes shifting of the surrounding (ligand) ions to a new equilibrium position, rearranging the interionic distance and transition to the lowermost of the vibrational levels ($\sim 10^{-12}$ sec) i.e., to the excited electronic level. If a transition occurs between the levels, say, m (excited electronic state) and n (ground state or state of lower energy), the lifetime τ_m is expressed as,

$$\tau_m = \frac{1}{(\Sigma A_{mn} + \Sigma C_{mn})} \qquad (1.1)$$

where, A_{mn} and C_{mn} denote the probability for radiative and nonradiative transitions between the levels. The summation is relevant whenever the transition occurs not over a single but over several sub-adjacent levels.

The fraction of emission transitions with respect to the sum total of emission and radiationless transitions gives the quantum yield η:

$$\eta = \frac{\Sigma A_{mn}}{(\Sigma A_{mn} + \Sigma C_{mn})} \qquad (1.2)$$

If there are N_m photons in the excited state initially, the exponential law of luminescence decay states that after a time t,

$$N(t) = N_m e^{-t/\tau_m} \qquad (1.3)$$

A direct relation exists between the emission intensity and the probability A_{mn} of emission transition given by,

$$I_{em} = N_m h\nu_{mn} A_{mn} \qquad (1.4)$$

Thus, shorter the lifetime of the excited state i.e. time for photon emission, more intensive shall be the glow. Conversely, the greater the probability C_{mn} of radiationless transition, the lesser the intensity of glow and hence the quantum yield. The greater the oscillator strength for a given transition, higher shall be the intensity of the emission, provided radiationless transitions are absent.

Photoluminescence is divided into two major kinds: intrinsic and extrinsic depending on the nature of electronic transition producing it.

1.2.2. Intrinsic luminescence

There are three kinds: band-to-band luminescence, exciton luminescence and cross luminescence.

1.2.2a. Band-to-band luminescence:

The recombination of an electron in the conduction band with a hole in the valance band generates band-to-band luminescence. This kind of luminescence is observed in pure crystals at relatively high temperatures. Eg: Si, Ge and IIIb-Vb compounds such as GaAs. The light emission from bright light emitting diodes and semiconductor lasers is usually due to band-to-band transition process.

1.2.2b. Exciton luminescence:

An exciton moves in a crystal conveying energy and produces luminescence owing to the recombination of the electron and the hole. There are two kinds of excitons: Wannier exciton and Frenkel exciton.

The Wannier exciton model expresses an exciton as composed of an electron in the conduction band and a hole in the valence band bound together by the Coulomb interaction. The expanse of the wavefunction of the electron and hole is much larger than the lattice constant. This kind of luminescence is observed in inorganic semiconductors such as IIIb-Vb and IIb-VIb compounds. Wannier

excitons are stable only at relatively low temperatures, where the binding energies of excitons are higher than the thermal energy. At higher temperatures, excitons are no longer stable, and band-to-band luminescence appears instead.

The Frenkel exciton model is used in cases where the expanse of the electron and hole wave function is smaller than the lattice constant. Typical examples are organic molecular crystals and inorganic complex salts. In these materials, the excited state of an isolated molecule or a complex ion transfers from molecule to molecule or from complex ion to ion usually owing to dipole-dipole interactions. It is therefore regarded as the exciton state. Luminescence characteristics are similar to those of isolated molecules or complex ions.

1.2.2c. Cross luminescence:

Cross luminescence is produced by the recombination of an electron in the valance band with a hole created in the outer most core band [4]. This is observed in a number of alkali and alkaline earth halides and double halides. This occurs only when the energy difference between the top of valance band and that of the outermost core band is smaller than the band gap energy. Or else, an auger process occurs selectively. The shape of the spectra reflects the grouping of the molecular orbitals in the clusters involving cations with a hole in the core shell and nearest neighbour halide ions. For crystals with more than one type of cation, the spectrum reveals information about the 'active' cation which contains the core hole and also about the other cations. A notable characteristic of cross luminescence is that the decay time is very fast, of the order of

nanoseconds or less, and hence such luminescent systems are used as scintillators.

1.2.3. Extrinsic luminescence

Luminescence caused by intentionally incorporated impurities (or activators) is classified as extrinsic luminescence. Most of the observed types of luminescence that have practical applications belong to this category. Extrinsic luminescence in ionic crystals and semiconductors is classified into two types: unlocalized and localized.

1.2.3a. Unlocalized type:

In the unlocalized type, the electrons and holes of the host lattice, i.e., free electrons in the conduction band and free holes in the valence band, participate in the luminescence process. This includes two kinds of luminescence transitions, namely the transition of a free carrier to a bound carrier and the transition of a bound electron at a donor to a bound hole at an acceptor. These kinds of luminescence lines and bands are usually observed in compound semiconductors such as IIIb-Vb and IIb-VIb compounds.

1.2.3b. Localized type:

Here, the luminescence excitation and emission process are confined in a localized luminescence center. Various kinds of metallic impurities intentionally

incorporated in ionic crystals and semiconductors often create efficient localized luminescence centers. Localized type centers are classified into allowed and forbidden transition type in terms of electric dipole transitions. The electric dipole transition can take place between energy levels only with different parities ie. $\Delta l = \pm 1$, l being the azimuthal quantum number. When atoms and ions are incorporated in crystals, the forbidden character of the dipole transition is altered by the perturbation of the crystal electric field, so that the forbidden transition becomes allowed to some degree.

(i) Allowed transition type:

1. s $\leftrightarrow$ p transition - F centre $\leftrightarrow$ (an electron trapped at an anion vacancy), Tl^0
2. $s^2 \leftrightarrow$ sp transition - Tl^+ ,Sn^{2+}, Pb^{2+}, Sb^{3+}, Bi^{3+}
3. f $\leftrightarrow$ d transition - Eu^{2+}, Ce^{3+}

Oscillator strength for this type of transition is of the order of 10^{-1}-10^{-3} and the luminescence spectra have a broad bell shaped appearance.

(ii) Forbidden transition type:

1. d $\leftrightarrow$ d transition - Ti^{3+} , Cr^{3+} , Cr^{2+} , Mn^{4+} , Mn^{2+} , Fe^{3+} , Fe^{2+}

Iron group ions show luminescence owing to the $3d^{n*} \leftrightarrow 3d^n$ (n = 2-8) transition in the visible to infrared region. Among them, Cr^{3+} and Mn^{4+} ions with $3d^3$ configuration and Mn^{2+} ion with $3d^5$ configuration are important for phosphor

applications. Spectra of transition metal ions comprise of either broad bands or characteristic lines.

2. f $\leftrightarrow$f transition - Pr^{3+} , Nd^{3+} , Sm^{3+} , Eu^{3+} , Tb^{3+} , Tm^{3+}, Dy^{3+} (and other trivalent rare earth ions)

Most trivalent rare earth (RE) ions give efficient line spectra owing to the $4f^{n*} \leftrightarrow 4f^{n}$ transition in the visible to near IR region. Among them, Eu^{3+} ion (red) and Tb^{3+} ion (green) are excellent activators for various practical phosphors. Absorption and emission spectra due to f-f transitions are rather sharp lines. As the 4f energy levels are well shielded by the 5s5p shells, they are weakly influenced by crystal field perturbations. So their emission does not change much with host lattice. Oscillator strengths of this type of transition, made allowed, are of the order of 10^{-4}-10^{-8}.

1.2.4. Energy transfer in luminescence: sensitization

If the phosphor host itself is self-luminescent or if there are two or more activators in a phosphor, an interaction can take place between the luminescent centers which shall be expressed in their luminescence spectra. The absorption spectra of the phosphor, in such cases, shall be a superposition of each of their absorption spectra. As for the emission spectra, the position of emission lines of each of them does not change in the presence of the other, i.e., superposition of the emission spectra occurs but with any of the following changes:

(1) the luminescent intensity of one ion can gain in strength at the expense of the diminishing intensity of the other,

(2) an ion not luminescent at a given concentration in a phosphor system becomes luminescent in the presence of the other ion in a different system,

(3) luminescence of an ion can be observed under conditions of an excitation (in the absorption band of another ion) in which it was not luminescent without the presence of the other ion,

(4) sometimes an ion even exhibits an intensified luminescence with complete quenching of the other.

Such luminescence observed in ions excited as a result of energy transfer from other ions that are excited in the absorption band is termed **sensitized luminescence**, i.e.,

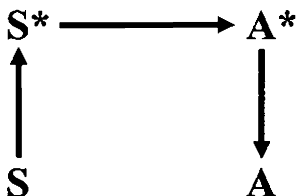

Here, S is the sensitizer (energy donor) and A is the activator (energy acceptor); asterisks denote their excited states. It is usually observed in phosphor systems, with Mn^{2+} and RE^{3+} ions as activators, which do not possess suitable excitation bands (band-to-band excitation is possible only at very high energies and merely narrow and weak absorption lines are associated with forbidden f-f transitions). This limitation is overcome by incorporating into the system a sensitizing ion with a suitable absorption band. Conversely, Cr^{3+}, RE^{2+} and other ions

themselves have the ability to present broad intensive absorption bands suitable for inducing luminescence.

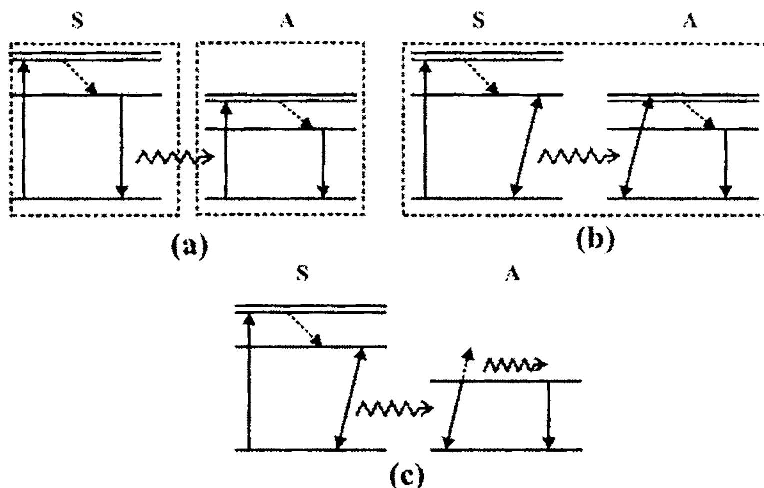

Figure 1.1. Sensitized luminescence: (a) Emission-reabsorption, (b) Resonance radiationless and (c) Nonresonance radiationless

In sensitized luminescence, the absorption band of the activator ions must overlap with the emission band of the sensitizer ions. In other words, the energy absorbed in the absorption band of the sensitizer ion is emitted in the emission band of the activator ion. Energy transfer from sensitizer to activator can occur in three different ways, the illustrations of which are shown in figure 1.1.

1.2.4a. Emission-reabsorption:

In this case, the light emitted by the sensitizer ion (primary luminescence) is re-absorbed and later emitted (secondary luminescence) by the activator ion. Both the sensitizer and the activator have intense absorption bands and behave as

independent systems which interact directly. The closer the emission energy of one to the absorption energy of the other, the more probable is the energy transfer to occur. An example is the intensification of Nd^{3+} luminescence in the presence of Sm^{3+}, Eu^{3+}, Tb^{3+} and Dy^{3+}.

1.2.4b. Resonance radiationless energy transfer

The resonance radiationless energy transfer mechanism is effected between interacting ions behaving like a single system. The sensitizer may not be necessarily emissive and the activator ions may not have sufficiently intensive absorption bands suitable for inducing luminescence. But the broad absorption bands of the sensitizer and the emission transitions of the activator together comprise a system capable of effective luminescence. Since a resonant energy transfer can be obtained between an allowed transition in the sensitizer and forbidden transition in the activator, this kind of mechanism is the prime cause of sensitized luminescence in inorganic luminescent systems.

The process of energy transfer is effected by dipole-dipole or dipole-quadrupole interactions between ions, the probability of the transfer being proportional to r^{-6} or r^{-8} respectively, where r is the mean distance between the interacting ions. Here, the reduced duration and decreased quantum yield of the sensitizer emission is compensated by the longer duration and greater quantum yield of the activator's luminescence. The probability of the energy transfer increases proportionally to the diminution of the mean distance between ions, reduction of the lifetime of sensitizer in an excited state and to a greater overlap of the

sensitizer's emission and activator's absorption. The decay curve, instead of being purely exponential, is a sum of exponential curves.

1.2.4c. Nonresonance radiationless energy transfer

The nonresonance radiationless energy transfer mechanism occurs in the event of a substantial nonconcurrence of distances between the levels of ion transferring the energy and the levels of the ion receiving the energy. This involves an exchange interaction between ions and comes into play over very short distances. Sensitization is therefore accomplished by impurity incorporation or lattice modifications. The energy is transferred to any pair of the acceptor levels (which need not be long living and emissive) whose distance is the closest to the energy transmitted by the sensitizer ion. Regardless of the fact to which pair of the acceptor levels the energy is transferred they become deactivated by means of rapid radiationless transitions to the radiation level from which the final emission ocurrs.

1.2.5. Concentration quenching (self-quenching)

If the energy transfer occurs from an emitting center to a nonradiative center, luminescence gets quenched. Such a change in luminescent intensity is manifested in various ways for different activators. Generally, the intensity of the glow passes through a maximum and then diminishes with growing concentration of the activator. This depends on the mechanism of interaction between these ion activators of the same kind.

(1) The emission-reabsorption energy transfer between ions of the same kind can lead to self-absoption, for eg., self-absorption of Cr^{3+} ion.

(2) The most common means of concentration quenching is nonradiative resonance multipole energy transfer between ions of the same type, as in many trivalent REs.

(3) An exchange mechanism of concentration quenching becomes apparent in the case of ions that fail to have coincident differences of the emission and radiationless levels of transitions (as for Eu^{3+}).

1.3. The phenomenon of electroluminescence (EL)

Electroluminescence is the direct, nonthermal conversion of electrical energy into luminous energy. The first observation on the effect of electric fields on luminescence was reported by Gudden and Pohl in 1920 [5]. Still, the famous paper by George Destriau in 1936 [6] is often cited as the first published report on electroluminescence. Destriau observed light emission from a suspension of ZnS:Cu dispersed in castor oil when subjected to ac fields.

A breakthrough in EL technology was made in 1974 by Inoguchi et al. (Sharp Corporation) [7], who was able to establish thin film EL (TFEL) cells based on ZnS:Mn, which had both higher efficiency and a reasonable lifetime. The key to this approach was the concept put forward by Russ and Kennedy [8] which described a three layer sandwich design. The highlight of the Inoguchi structure was that the insulators completely encapsulate the active layers and serve as buffers, shielding the device from breakdown when local current densities are

high. The high reliability of the structure and the fair reproducibility of the device characteristics due to improved thin film deposition techniques helped one to investigate the physical aspects of high field EL more precisely from the aspect of fundamental research. This innovation is credited with transforming the research and development of electroluminescence into a viable display technology.

Today, both thin film and powder EL displays are active in the market place. While both ac and dc driven devices have been explored for display applications, the interest in ac driven thin film electroluminescent devices has dominated. Since the thesis is focused on ac thin film EL devices, the structure and physics of ACTFEL devices are discussed briefly.

1.4. ACTFEL devices

There are two classes of EL devices - Injection EL or low field EL ($\sim10^4$ V/cm) based light emitting diodes (LED) and high field EL ($>10^6$ V/cm) based TFEL displays. Both are distinct physically and fundamentally. The TFEL devices differ in principle from standard LEDs and diode lasers. In the former, the generation of light is by the impact excitation of light emitting centers by high energy electrons accelerated by an electric field whereas in the latter, electron-hole recombination near a p-n junction is responsible for luminous emission. To achieve sufficient diffusion length of the minority carriers and radiative recombination in the low field regime, single crystalline materials are needed for

LEDs and diode lasers. Polycrystalline films can be used in high field EL, which is a considerable advantage of thin film EL displays.

Ac drive	Ac thin film	• High resolution, matrix drive • Long lifetime • Multicolor and full color capabilities
	Ac powder	• Backlight for liquid crystal displays (LCD) • High luminous efficiency • Short lifetime.
Dc drive	Dc thin film	• Reliability problem
	Dc powder	• Low voltage matrix drive • Multicolor capability

Table 1.1. Comparison between the four types of EL displays

High field EL devices have been categorized into four based on the drive voltage waveform and the phosphor configuration: ac thin film EL (ACTFEL), ac powder EL (ACPEL), dc thin film EL and dc powder EL. Table 1.1 outlines some comparative remarks on the four kinds of EL devices.

DCEL has been widely used for small displays on glass in automotive environments usually as yellow fixed messages and for backlighting purposes. ZnS:Mn based ACTFEL displays used as flat screens of laptop personal computers and word processors and ACPEL devices used as backlights for liquid crystal displays are today commercially available.

Powder EL displays have virtually unlimited potential, i.e., uniform light emission, thin profile and low power consumption [9]. Flexible powder EL devices can be made on polyethylene terephthalate (PET) coated indium tin oxide (ITO) substrates [10, 11]. Powder EL lights have been used for architectural and decorative lighting and as backlights in cellular phones, personal digital assistants (PDA) and palmtop computers. But they also possess multiplexing limitations and suffer from low luminance, high operating voltage, poor contrast and significant luminance degradation over fairly short time (~ 500 hrs). With the development of thin film technology in the 1960's, the initial efforts to utilize the phenomenon of electroluminescence on powder EL devices turned to developing thin film EL devices.

Thin film phosphors have several advantages in comparison to the powders, such as higher lateral resolution from smaller grains, better thermal stability, reduced outgassing, and better adhesion to the solid surface [12]. However, the biggest drawback in the use of phosphor thin films is their low brightness and efficiencies in comparison to those of bulk powder materials which are primarily associated with factors such as internal reflection, the small interaction volume between incident beam and solid and absorption of generated light by substrate materials.

An ACTFEL display possesses several unique features:

Solid state nature: The solid state construction renders an ACTFEL device extreme ruggedness making them more resistant to shocks and vibrations. They

can, therefore, withstand aggressive environments, such as cold, heat, wind, dust, sunlight, a characteristic desirable for displays used in military equipments and spacecrafts. The luminous emission in a solid state environment also eliminates the risks involved in maintaining a vacuum or plasma environment. Moreover, the solid state nature enables it to be fully integrated onto the substrate of the drive electronics.

Wide viewing angle: The emissive EL displays offer a viewing angle greater than 160° which has been an inherent problem with LCDs. The absence of optical elements in the light path (other than the glass substrate) renders them this property and so very useful for medical and industrial applications.

Wide operating temperature: EL panels can be operated over a wide temperature range (-25°C to 65°C), often limited by the drive electronics, and therefore can serve in many critical military and industrial applications. They don't freeze or get get slow or dim even at low temperatures.

Long life: The panel itself has no significant wearout mechanism. Display panels have demonstrated device lifetimes of over 50,000 hours with less than 10% luminance change.

High contrast: This property gives EL displays what we call "at a glance" readability. This property makes them highly efficient in a very high ambient illumination environment such as in industrial instrumentation. Such high legibility is the strongest selling point of TFEL displays.

Better display qualities: Fast response, high resolution and small pixel size are some of the best qualities of an EL display. They operate at video rates high enough to produce high information content flat panel displays (FPDs) with the image quality of the cathode ray tubes (CRTs).

ACTFEL displays overrule LCD's, that make almost 90% of the current FPD industry, in their ability to pattern much smaller pixels, performance over a wide temperature range, wide viewing angle and readability with much greater intensity background light. The disadvantages of ACTFEL displays over LCD's are larger power consumption, much larger driving voltages and the lack of adequate chromaticity of the three primary colors.

1.4.1. ACTFEL device structure

There are three general configurations for thin film EL device structures as shown in figure 1.2 - (a) doubly insulated standard MISIM (metal-insulator-semiconductor-insulator-metal) structure, (b) doubly insulated inverted MISIM structure and (c) singly insulated structure.

The most frequently used ACTFEL structure is the 'standard' double insulating layered structure on a transparent glass substrate. Here, the phosphor material is sandwiched in between two dielectric layers. The bottom electrode is transparent and the top electrode is opaque. In the 'inverted' double insulating layer structure, the electrodes are simply inverted and so the light emission now takes place in the opposite direction unlike that in the standard case. The advantage is

that opaque substrates like silicon which could withstand higher temperatures can be used as in active matrix electroluminescent (AMEL) [13] displays as well as thick film dielectric hybrid electroluminescent (TDEL) displays [14].

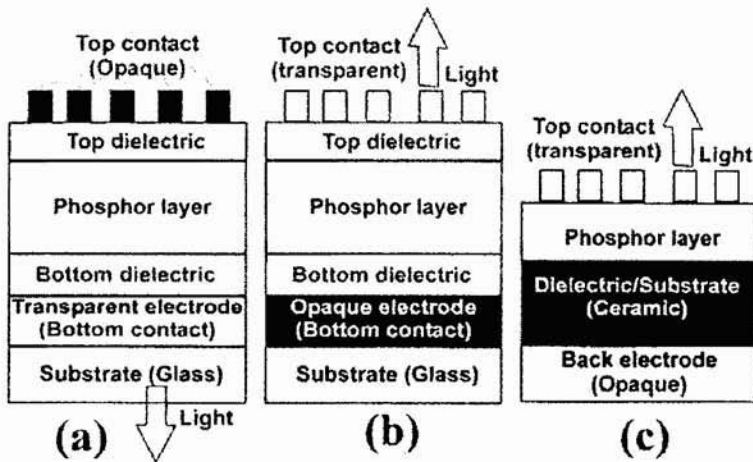

Figure 1.2. (a) Standard MISIM (b) Inverted MISIM and (c) Single insulating ACTFEL structures

AMEL displays typically use silicon substrates that allow the drive electronics and the EL device to be manufactured on the same substrate. High performance displays with a resolution of 2000 lines per inch (LPI) have been manufactured with this technology. AMEL technology is employed in helmet mounted or heads-up display applications, which include commercial virtual reality games and military flight simulators. The TDEL technology uses an opaque alumina substrate on which they screen print an opaque high dielectric constant ferroelectric thick film as one of the insulating layers. There are several advantages of the thick film hybrid EL approach, namely (1) the alumina substrate is stable at high temperatures above the softening point of a glass

substrate, (2) higher dielectric constant insulators can be used, and (3) thick film processing is inherently cheaper than thin film processing. Most ACTFEL phosphors become brighter and more efficient as the annealing temperature increases. In multicolor displays, color filters are often employed to provide saturated or pure red, blue, and green color components. These filters, typically dyed organic materials, are usually positioned in between the phosphor and the emitting side of the display. Because the filters cannot withstand the temperatures needed to process the other layers of an ACTFEL device, they must be deposited last on the top of the device and this necessitates the use of the inverted structure. One disadvantage of this approach is that the pixel resolution is limited due to the surface roughness of the substrate.

Apart from these, single insulating layered structures are also practiced. Here, the EL oxide phosphor is directly deposited either onto a thick $BaTiO_3$ insulating layer or onto a $BaTiO_3$ ceramic sheet. The former structure avoids chemical reaction of the phosphor layer with the $BaTiO_3$ substrate during post-annealing. In the latter structure, the ceramic substrate serves a double function of the device substrate and of an insulating layer between the substrate and the EL phosphor. Moreover, the $BaTiO_3$ ceramic sheet substrate can be utilized primarily for high temperature annealing above 1000^0C.

The replacement of a Si substrate for the $BaTiO_3$ ceramic sheet is beneficial to avoid undesirable chemical interactions with the EL phosphor. Furthermore, Si is suitable for high resolution electrodes for active/passive matrix addressing, whereas $BaTiO_3$ substrate is impractical to do so.

1.4.2. The ideal model

The basic ACTFEL device structure can be modeled as a simple circuit where the insulators are represented by perfect capacitors and the phosphor layer is represented by a capacitor below threshold and a pair of back-to-back diodes above threshold [15]. The equivalent circuit model shown in figure 1.3 very well demonstrates the essential phenomenological physics of a thin film EL device.

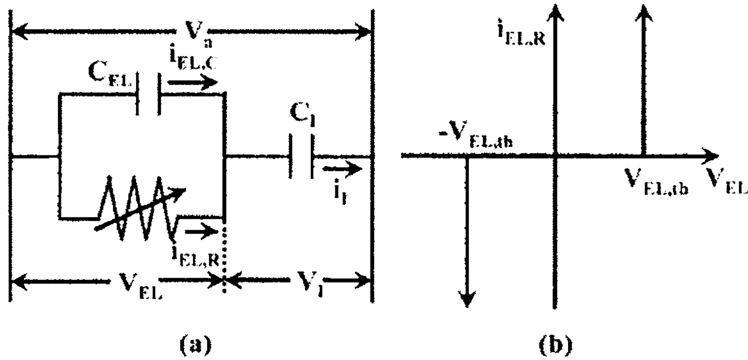

Figure 1.3. (a)Equivalent circuit of an ideal ACTFEL device and (b) Ideal I-V characteristics of the nonlinear resistor of the phosphor layer

Below threshold, the model treats the TFEL device as a three series capacitor circuit where the voltage drop across each layer is proportional to the dielectric constant and the layer thickness. The first and second insulating layers are incorporated into one effective insulating layer with the effective capacitance per unit area, C_I, given by

$$C_I = \frac{C_{I1}C_{I2}}{C_{I1} + C_{I2}} \qquad (1.5)$$

where C_{I1} and C_{I2} are capacitances per unit area of the first and second insulating layers, respectively. The thin film phosphor behaves as a capacitor below the threshold voltage V_{th} with the capacitance per unit area C_{EL}. However, above the threshold voltage real (dissipative) current flows in the phosphor layer and gives rise to the light emission. Therefore, the phosphor layer is described as a capacitor in parallel with a nonlinear resistor with the ideal I-V characteristic as shown in figure 1.3. In an ideal case, this nonlinear resistor can be simulated by back-to-back Zener diodes. The luminance of the device is proportional to the power consumed in this resistive branch with the proportionality constant being the experimentally determined luminous efficiency η in units of lumens per watt (lm/W).

Factors like transferred charge density, power dissipation and luminance that determine the device performance can be expressed in terms of device parameters such as layer thickness, dielectric constant, dielectric breakdown strength, threshold field and luminous efficiency based on the ideal model considerations [16]. The model even explains most of the observed thin film EL device characteristics except the time dependence of charge transport [17, 18].

1.4.3. ACTFEL device physics

The basic function of each layer of a TFEL device is the same irrespective of whether the structure used is the standard or the inverted MISIM. The solid state processes are summarized in figure 1.4. The vertical axis represents energy. The band is tilted from the cathode side of the phosphor layer to the anode side as a

voltage drop is applied across the phosphor layer. The physical processes involved in high field EL are [9]:

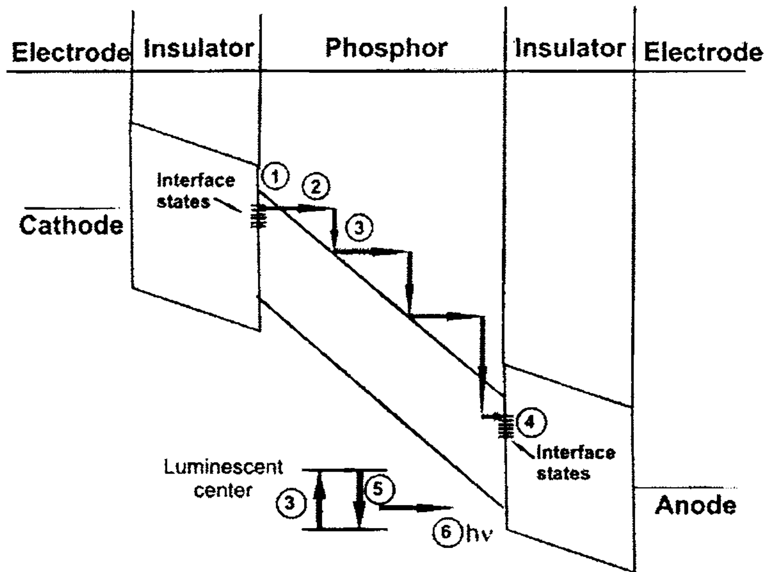

Figure 1.4. Mechanisms that occur in an ACTFEL device

(1) **Electron injection** from insulator/phosphor (IS) interface states into the conduction band of the active layer

(2) **High field charge transport** i.e., the subsequent acceleration of the carriers in the phosphor layer at high electric fields to optical energies

(3) **Impact excitation** of luminescent centers by energetic electrons

(4) **Electron re-capture** at the opposite IS interface leading to polarization effects

(5) **Radiative de-excitation** of the luminescent centers

(6) **Radiative out-coupling** of the generated photons

1.4.3a. Electron injection

In capacitive coupled ACTFEL devices, the carriers are injected from the IS interfaces rather than from the external electric circuit when the phosphor field exceeds a threshold value. There are several reasons to state that the interface is the source of carriers. The discontinuity in the periodic lattice structure at the IS interface results in dangling chemical bonds that creates electronic states within the forbidden gap (Tamm states). The depth and concentration of the available interface states changes significantly with the choice of the dielectric. Also, the threshold field for charge transfer gets modified with a change in the nature of the insulator or its deposition methods [19]. Moreover, it has been observed that devices with different top and bottom insulators generate asymmetric device currents and threshold fields as a function of the polarity of the applied voltage [20]. Deeper the interface state, least probable is the electron injection process until extremely high fields are reached. Conversely, if they are too shallow, electrons will inject at low fields and will not be accelerated to high enough energies to promote luminescence. The optimum interface trap depth is a rather delicate balance between the two competing processes. Electron state depths 0.6 to 1.3 eV below the conduction band minimum have resulted in good device performance [19, 21].

The electron injection into the conduction band of the phosphor layer can occur via tunnel injection or field assisted thermal ionization (Schottky emission). But the fact that the electrical properties of an ACTFEL device are only a weak function of temperature, compared to what one would expect for Schottky

emissions, rules out a strict thermionic emission process [19, 22]. So the predominant carrier injection mechanism is assumed to be Fowler-Nordheim tunneling (temperature insensitive) [21]. Reports [23] also say that pure tunneling is the dominant electron ejection process from deep traps at the interface during the leading edge of the applied voltage pulse while phonon assisted tunneling (PAT) of electrons from shallower interface states is the relevant mechanism at the trailing edge and between the pulses. Pure tunneling, however, is the more dominant process above fields ≥ 1 MV/cm and PAT prevails for relatively small residual fields (~ 0.3 – 0.4 MV/cm) [23].

As tunneling was the dominant mechanism of electron injection, one can expect an improved device performance on increasing the density of occupied states by modifying the phosphor/insulator interface. Several groups have reported an increase in the charge injected into the phosphor layer in yellow ZnS:Mn [24-26] and blue $Ca_xSr_{1-x}Ga_2S_4$:Ce [27] phosphors by introducing a thin interfacial layer between the phosphor and the insulating layer. Rack *et al.* even reports that the addition of a ZnS layer (30 nm) beneath the $Ca_xSr_{1-x}Ga_2S_4$:Ce phosphor layer even facilitated the crystallization of the amorphous as-deposited phosphor material during the post-deposition anneal, that inturn improved the device performance.

1.4.3b. High field charge transport

The electron energy distribution inside the active phosphor layer is a complicated function of high field scattering mechanisms such as intervalley

scattering, polar optical phonon scattering, acoustic phonon scattering, ionized impurity scattering, band-to-band impact ionization and impact excitation [28]. These scattering mechanisms governing the electronic transport in high field EL materials solely depend on the energy band properties of the host phosphor. Most studies show that electron-electron interaction does not play a significant role in high field charge transport. The electrons are transported across the active layer under the combined force of the electric field and the scattering potential mainly by electron-phonon (e-ph) interactions. Polar longitudinal optical scattering, referred to as Frohlich scattering [29], with phonons of low momentum causes only small changes in electron momentum so as to scatter them along the direction of the electric field. Scattering with neutral impurities is negligible at 300 K as the corresponding scattering rates are very low compared to e-ph scattering rates [28]. Ionized impurity scattering plays an important role for mobility in the low field region (<0.1 MV/cm) but scattering rate decreases with electron energy and therefore doesn't affect the transport behavior at fields ≥ 1 MV/cm.

Several models have been proposed to explain high field electron transport in sulphide based ACTFEL devices. Brennan's Monte Carlo simulations [30] predict that only 1% of the carriers gain energy > 2 eV at an electric field of 1 MV/cm and 50% at 2 MV/cm. The modified Monte Carlo simulations of Bhattacharya *et al.* [28] predicts 26% of the carriers to gain energy > 2 eV at 1 MV/cm and 65% at 2 MV/cm. The lucky drift theory modified by Bringuier [31, 32] suggests that 27% of the carriers gain energy above 2 eV at 1 MV/cm and

72% at 2 MV/cm. Only the model by Mach and Muller [33], based on ballistic acceleration, predicts that all electrons turn hot for fields around 1 MV/cm.

1.4.3c. Impact excitation/ionization

Under the influence of the high applied electric fields (~10^6 MV/cm), the accelerated charge carriers turn 'hot' (referred so as their energy is much higher than the mean energy at thermal equilibrium). Those that gain sufficient energy promotes an electron in the ground state of the luminescent center either into a higher atomic state of the luminescent center or into the conduction band of the host material, referred to as impact excitation [31] or impact ionization [34] respectively. When the electron is impact excited, it relaxes back into its ground state either radiatively or nonradiatively. For a given dopant concentration and free charge carrier density, the impact excitation probability depends on the radiative cross section of the luminescent center and the energy distribution of the charge carriers. When an electron is impact ionized, the excited electron is immediately accelerated toward the anode by the electric field. Subsequent light emission from the ionized luminescent center requires that an electron be recaptured from the conduction band. Such a two step EL process alters the relaxation kinetics as compared to impact excited centers [32].

1.4.3d. Electron capture

In contrast to dc driven EL devices, the carriers do not leave the semiconductor because of the potential barrier at the IS interface. At the end of the voltage

pulse, the carriers get thermalized (releases energy as heat to the lattice) and are trapped in deep levels at the anodic phosphor-dielectric layer interface. The resultant "polarization charge" has two profound effects on device operation.

First, these charges counteract the applied voltage, acting as a negative feedback mechanism making it increasingly more difficult to inject more charge from the cathode. Second, a non-zero polarization field exists even when the external applied voltage is zero. This field, however, has two consequences. On the one hand, it is responsible for the "leakage charge" that flows across the device when the applied voltage is zero in the charge-voltage characteristics of the device. On the other hand, this polarization field adds to the external field if the subsequent pulse applied across the device has an opposite polarity. Thus, the phosphor threshold field is now reached at a lower external applied voltage than the threshold voltage, a voltage termed the 'turn on voltage'. The lowering of the turn on voltage and the transferred charge amplification is repeated in the following half cycles of an ac supply. This process continues until a steady state operating condition is established.

1.4.3e. Radiative de-excitation

When an impurity center is in an excited state, the energy will eventually be dissipated. The relaxation process can occur by either 1) emission of a photon, 2) nonradiative relaxation which can be in the form of emission of one or more phonons to the lattice etc, or 3) energy transfer to another center. For display

applications, it is desirable to maximize the first process and to minimize the second. The third case can be useful or harmful in different situations.

1.4.3f. Radiative outcoupling

Only a fraction of the generated photons are out-coupled from the system through the transparent surface along a direction normal to the emitting surface. If one assumes that charge injection and storage occur only at the IS interfaces [35], the total efficiency η_{tot} is the product of three partial efficiencies, i.e.,

$$\eta_{tot} = \eta_{exc}\eta_{rad}\eta_{out} \quad (1.6)$$

Of all the electrons that traverses the active layer, not all excites the luminescent centers. Hence, the excitation efficiency η_{exc} gives the ratio of the number of luminescent centers excited to the total charge transferred across the active layer. Of all the impact excitations that occur within the phosphor, not all decays radiatively. The radiative efficiency η_{rad} expresses the ratio of the number of centers decaying radiatively to the total number of luminescent centers excited. Once the photons are generated, all of them do not escape the device in the direction of the viewer. Some undergo total internal reflection and some photons may be lost by absorption and some by reflection. The optical outcoupling efficiency η_{out} is therefore a measure of the number of photons outcoupled to the total number of photons generated within the system.

η_{exc} and η_{rad} are related to the physical processes in the semiconductor layer. η_{out} can be improved by increasing the surface roughness and thereby reducing

internal reflection. However, too rough a surface can reduce contrast because of increased diffuse scattering.

1.4.4. Space charge effects

One of the major deviations from the ideal operation of ACTFEL devices is the formation of space charge within the phosphor layer. Electric field in a ACTFEL device shall be uniform if (1) only IS interface states are involved in free charge carrier supply and trapping and (2) field distortion provoked by the charge flow is low. But there are situations where ionized centers remain in the semiconductor when bulk contributes to charge via thermal or field induced effects, generating a fixed space charge large enough to create a significant field distortion. The removed electron is swept from the ionized trap towards the anode while the trap itself is now positively charged and therefore acts to bend the energy bands locally downwards. The ionized center is usually an intentionally added impurity which acts as a donor due to valence mismatch, a luminescent impurity whose excited state lies close in energy to the conduction band, a vacancy, or another point defect. A second common source of space charge is band-to-band impact ionization of the lattice whereby an additional electron is promoted to the conduction band as a delocalized charge carrier. The hole, left in the valence band, drifts towards the cathode a short distance before it is trapped, resulting in a localized positive charge which, as above, pulls the energy bands downward. The space charge induced curvature of the phosphor layer energy bands is depicted in figure 1.5 for a device under bias. The dotted lines show the spatial dependence of the phosphor layer energy band locations in

the absence of space charge. The linearity of the bands indicates that a uniform electric field exists across the phosphor in the absence of space charge.

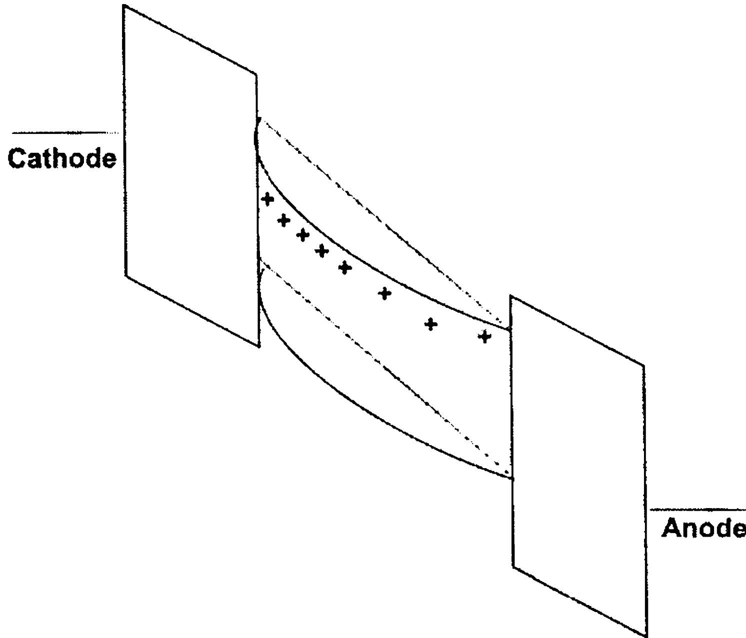

Figure 1.5. Space charge induced band bending of phosphor layer in ACTFEL device

A positive space charge enhances the field at the cathodic end than at the anodic side resulting in a nonuniform electric field across the ACTFEL device. As the tunnel emission rate of electrons is a strong function of electric field, it occurs at a lower external voltage (i.e. the ACTFEL device has a smaller turn on voltage) due to the enhanced electric field at the cathodic IS interface. And the reduced electric field at the anodic IS interface results in lesser density of energetic electrons in this region, which reduces the likelihood of impact excitation in this region but may preclude hot electron induced damage to the anodic phosphor-

dielectric interface. Marello *et al.* [36] has found that the excitation efficiency is lower in the anodic field region in the presence of space charge. Additional higher order effects may also result from the nonuniform electric field. For instance, efficient carrier trapping occurs at the low field anodic region, which may not occur appreciably in the high field cathode region. Moreover, the charge-voltage and luminance-voltage curves of an ACTFEL device exhibit a hysteretic behavior on account of the presence of space charge within the device.

Space charge in ACTFEL devices can be either 'static' or 'dynamic' in nature. Normally the space charge created will be annihilated at some characteristic rate. The annihilation may be due to recombination of an electron with an ionized trap or the re-emission of trapped hole. If the annihilation proceeds at a slow rate compared to ac drive wave form, the space charge forms a steady state distribution and is denoted as static. Dynamic space is that portion of total space charge that is not in steady state but both created and annihilated with in one period of the drive waveform.

All well known ACTFEL phosphor systems have been found to exhibit space charge effects. On the one hand, the presence of space charge reduces the voltage necessary for device operation. This should improve reliability and efficiency while reducing driver circuit complexity. On the other hand, the energy expended creating and maintaining the space charge may reduce efficiency, especially when the space charge is dynamic. Once the effects of space charge in a particular system are understood, it may be possible to engineer the space charge in an advantageous way.

1.4.5. Material requirements for ACTFEL devices

TFEL displays are complex optoelectronic devices with challenging material requirements. The multilayered ACTFEL device structure includes two electrodes (of which one is transparent), two insulators, and a semiconducting phosphor layer. Each layer has unique electronic and optical properties that must be satisfied for device operation.

1.4.5a. Substrate

Choice of the substrate checks the EL characteristics and device reliability. Smoothness of the substrate surface influences adhesion and optical properties of the ACTFEL stack. The properties of the substrate often put restrictions on subsequent fabrication steps, such as high temperature annealing and chemical cleaning. The substrate should not interact chemically with other layers of the device and should withstand exposure to processing chemicals and conditions.

Glass substrates, usually employed in EL device fabrication, must satisfy the following physical properties:

(1) high transmission coefficient in the visible region,
(2) thermal expansion coefficient that matches that of the deposited films,
(3) high softening temperature,
(4) low or no alkali metal content, and
(5) high electrical resistivity.

Glass substrates are used because of their transparency, cost and thermal expansion coefficient match to common materials. The commonly used Corning 7059 and NEG substrates are devoid of alkali content, which if diffused into the semiconducting phosphor layer, would result in device degradation with time. But the low softening temperature of the glass substrate restricts high temperature post-deposition treatments that lead to low luminance output. High temperature glass ceramics are also available that typically cost 10 times that of the standard 7059 glass. Si wafers and thick $BaTiO_3$ ceramic sheets are also used as substrates for fabricating EL devices with inverted MISIM structure.

1.4.5b. Electrodes

Two kinds of electrical contacts are needed in ACTFEL devices: opaque and transparent. Atleast one contact needs to be transparent to outcouple the light generated from the device. The materials chosen as electrodes should adhere well to its neighboring layers to prevent delamination. The resistance of the contacts should be minimized to prevent resistive heating of the device and unnecessary power consumption.

(i) Transparent contacts

Transparent conducting electrodes (TCOs) with high conductivity and high transmittance in the visible region are generally used as the transparent electrode of an ACTFEL device. The common example is indium tin oxide (ITO: In_2O_3 with 10 wt% of SnO_2) with a typical sheet resistance of 5-10 ohms/square. Since ITO can be easily etched by normal lithographic techniques, it is suitable for fine

patterning (~ 8 lines/mm) necessary for high information content FPDs. Other TCO's used are $CdSnO_3$, ZnO:Al or amorphous indium gallium zinc oxide.

(ii) Opaque contacts

The requirements of the rear metal electrode for EL applications are:

(1) good adhesion to the insulating layer,
(2) no metal ion migration at high electric field,
(3) no propagating breakdown, and
(4) low resistivity.

For the standard structure, the requisites of the opaque electrode are not stringent as it is the last layer deposited. Some of the opaque/metal electrode materials used are Al, Mo, Ta and W. Of these, Al is most frequently used as it can be deposited easily by thermal evaporation. Moreover, Al is inexpensive, highly conductive and reasonably immobile at high fields. However, its high optical reflectivity is undesirable. The engineering tradeoff is that ambient light is also reflected back towards the viewer, apart from the device emission, which can cause contrast problems. The low melting temperature (660°C) of Al is advantageous because Al gets easily vaporized if a short develops within the device; thereby open circuiting the device over a small portion instead of resulting in catastrophic device failure. But this feature of Al restricts its use as the opaque contact in inverted structure ACTFEL devices. Mo and W, preferred in the inverted TFEL structure, must satisfy the additional requirements like:

(1) high melting point,
(2) thermal expansion coefficient that matches that of the substrate,
(3) small reflection coefficient in the visible region to obtain good contrast.

1.4.5c. Insulating layer

The chief objective of an ACTFEL insulating layer is to protect the phosphor layer from catastrophic breakdown under high electric fields. They ensure high stability to the device protecting the phosphor layer against impurities and moisture from outside. The insulating layers must be able to withstand high temperature treatments during fabrication. Also, they must prevent metal ion diffusion into the phosphor layer and provide interface states at the boundary of the phosphor and the insulating layer. The insulator requirements for reliable and efficient ACTFEL devices are:

(1) high dielectric constant,
(2) high dielectric breakdown electric field,
(3) small number of pinholes and defects,
(4) good adhesion, and
(5) small loss tangent.

There are two groups of dielectric materials used in TFEL devices: (a) amorphous oxides and nitrides, such as Al_2O_3, SiO_2, Y_2O_3, TiO_2, Si_3N_4, Ta_2O_5, $BaTa_2O_6$; (b) ferroelectric materials, such as $BaTiO_3$, $PbTiO_3$. But dielectric materials with high dielectric constant have low breakdown electric field and

viceversa. So a product of the two quantities, referred to as the figure of merit of a dielectric material, is introduced. Moreover, insulating layer materials with a self-healing breakdown mode is generally preferred to those with a propagating breakdown mode.

1.4.5d. Phosphor layer

The active component of the device, that is, the light emitting layer (termed phosphor) consists of two constituents: (1) the host material which dominates the electrical properties of the phosphor layer, and (2) the luminescent center or the activator which dominates the optical properties of the phosphor layer. The host material provides a lattice for the substitutional incorporation of the activator atoms. The activator concentration is of the order of one percent of the host material, which are several orders of magnitude larger than that typically used for semiconductor doping. The essential requisites of an EL phosphor host material are:

(1) A large enough band gap to emit visible light without significant absorption,
(2) Capability to sustain a high electric field ($>10^6$ V/cm) without breakdown,
(3) Insulating characteristics below the threshold voltage, and
(4) Must be able to withstand the requisite post annealing treatments.

Luminescent impurity requirements are:

(1) Be properly incorporated into host material and emit visible light,

(2) Have a large cross section for impact excitation, and

(3) Be stable in the high electric field (>10^6 V/cm).

The crystalline quality and stoichiometry of the phosphor host are critical for efficient incorporation of the activator atoms into the lattice, which inturn determines the efficiency of light emission. The host lattice can influence the color spectrum because different phosphor hosts present different local crystal fields in terms of both field strength and field symmetry. Depending upon the nature of the luminescent transition, the crystal field or a small perturbation may be very important in determining the spectrum of the phosphor.

A good EL phosphor host has the additional and often harder to meet requirement of being able to provide a medium for the efficient transport of high energy (> 2 eV) electrons. This limits the class of possible materials to large band gap (E_g > 2.5 eV) semiconductors and insulators. The classical EL phosphor consists of a ZnS host lattice doped with Mn atoms for the light emission centers.

The nature of the luminescent impurity also determines the spectral emission from a phosphor. For effective incorporation, it is essential that the ionic radii and valency of the activator ion match well with that of the host lattice cation that it replaces. Larger the ionic size of the activator ion, more difficult is the ionic diffusion into the host lattice inhibiting polycrystalline grain growth. Smaller the size, they serve as potential interstitial impurities, subsequently affecting device stability. Moreover, the defects act as nonradiative centers

thereby reducing the device luminance and efficiency. In case of valence mismatch, charge compensation can be achieved intrinsically via vacancy creation (Schottky defects). Charge neutrality by extrinsic compensation can also be achieved by co-doping with monovalent ions such as Na, K or Li occupying divalent cation sites. Such extrinsic charge compensating impurities are referred to as co-activators.

A co-activator functions as a flux agent, compensator or luminescence co-activator, and helps in modifying the luminescent properties of the phosphor. The most effective flux agents are non-isovalent with the constituent atoms of the phosphor host and generate vacancies, thereby improving the atomic diffusion and the host crystallinity. Compensating co-activators are added to accomplish charge compensation in the phosphor host. When activator ions complexes with such defects, a color shift in the luminescence spectra is observed. Blue emitting Ce^{3+} and Cu^{+} are efficient luminescent co-activators of red Eu^{2+} activator that strongly absorbs blue light. The presence of 'killer centers' in the phosphor host can also degrade its overall performance [37].

The commercially available sulfide based phosphors often degrade under high energy electron bombardment due to dissociation of the cation-sulphur bonds. This process generates corrosive sulphur bearing gas species that contaminate emission tips and shortens the device lifetime. Due to their hygroscopic characteristics and short term reliability, better substitutes to sulphide phosphors are widely under research. The thermodynamic stability of oxides over sulphides has triggered extensive studies in oxide phosphor materials.

1.5. Oxide phosphors

Oxide thin film phosphors have received considerable attention for use in FPDs owing to their excellent luminescent characteristics, stability in high vacuum, and absence of corrosive gas emission under electron bombardment when compared to sulphide based phosphors. Some long standing problems of sulfide phosphor based TFEL devices such as the lack of primary color emissions and their chemical stability, especially in regard to moisture, have been remedied with the advent of oxide phosphor TFEL devices. They are insensitive to storage and handling in air. Their synthesis is generally easier and safer as no reactive gases are needed during their synthesis whereas reactive gases that other families of materials require for synthesis, sintering and annealing are invariably dangerous and toxic.

But there are several factors that prevent oxides from becoming the dominant class of ACTFEL phosphor. Oxide phosphors, with their large band gaps (compared to sulphides), are generally considered to be incapable of transporting significant current densities of hot electrons, and as such are not traditionally considered as good candidates for efficient EL phosphor hosts. Over the last few decades, a number of efficient oxide EL phosphors have been discovered capable of accelerating electrons to energies 'hot' enough to impact excite the luminescent centers.

Another issue regarding oxide phosphors is that their luminance-voltage curves are much less steep than those of sulphides. This inefficient carrier injection is

attributed to their larger effective mass and deeper interface state trap depth that, in turn, leads to non-abrupt device thresholds and larger driving voltages of oxide based ACTFEL devices.

Another serious drawback of oxide phosphors is that they require high temperature processing during and/or post-deposition to achieve a high degree of polycrystallinity, their crystallization temperature lying above 1000°C. This refractory nature limits their deposition by thermal evaporation. Moreover, instead of glass substrates, an inverted structure with a high temperature tolerant substrate and a refractory insulator is therefore preferred for the fabrication of oxide phosphor based ACTFEL devices. In comparison, the deposition of sulphides is less complicated owing to their lower melting point. So they can be easily grown by simple evaporation without the addition of a gaseous species to provide the lost anionic atoms, as sulphur is significantly more condensable than oxygen.

There are several binary and ternary oxides that serve as attractive ACTFEL phosphor candidates. Y_2O_3 [38, 39] and Ga_2O_3 [40, 41] are two binary oxides widely investigated as phosphor hosts. A series of undoped and rare earth doped ZnO electroluminors have also been studied [42, 43]. Ternary oxides used in phosphor applications include borates, phosphates, vanadates, tungstates, molybdates, aluminates, silicates, sulphates, germanates, gallates, niobates, titanates and tantalates [44-51]. Among these, silicates and gallates are widely studied, the phosphates and germanates to follow. The alkaline earth phosphates, though investigated, are probably not the best choice for ACTFEL applications

because both the binary alkaline earth oxides and P_2O_5 are moisture sensitive and so shall their compounds be. So they can serve as excellent fluorescent lamp and CRT phosphors due to the presence of an evacuated space for these applications.

Among silicates, $Zn_2SiO_4:Mn^{2+}$ [52, 53] and $Y_2SiO_5:Ce^{3+}$ [54] are widely investigated as low voltage green and blue phosphor respectively. In 1990, Minami *et al.* fabricated a bright electroluminescent device with an efficiency of 0.15 lm/W by sandwiching a thin film of $Zn_2SiO_4:Mn^{2+}$ between a $BaTiO_3$ sheet and a transparent conducting electrode ZnO:Al [55]. Since then, progressive research efforts were triggered in the field of high brightness, high stability oxide phosphor electroluminescence. Ouyang *et al.* [56] reported on the fabrication of a multilayered rf sputtered TFEL device using Mn activated Zn_2SiO_4 and Ce activated Y_2SiO_5.

The substitution of Si by Ge was found to lower the processing temperature. Stuyven *et al.* [57] reports on the fabrication of ACTFEL devices using the green emitting $Zn_2Si_{0.5}Ge_{0.5}O_4:Mn^{2+}$ phosphor on glass substrates (0.44 lm/W @ 60 Hz) and $BaTiO_3$ ceramic sheets. $Zn_2GeO_4:Mn^{2+}$ have been extensively studied as an efficient green germanate phosphor. An efficiency of 0.45 lm/W has been reported [58] for $Zn_2GeO_4:Mn^{2+}$ active ACTFEL devices fabricated on NEG/ITO/ATO substrates.

Recently, red $Ga_2O_3:Eu^{3+}$ ACTFEL devices have been realized on transparent ITO/ATO glass substrates using pulsed laser deposition [59]. Even higher

efficiencies of up to 10 lm/W have been reported in yellow emitting $Y_2O_3:Mn^{2+}$ and $(Y_2O_3)_{1-x}(GeO_2)_x:Mn^{2+}$ [60, 61]. With continued research, commercial oxide phosphor ACTFEL devices may become a reality in the not so distant future.

1.6. White phosphors

White light emitting EL displays have aroused great interest among researchers for producing full color flat panel displays using filters as well as ergonomically suitable white screens, e.g., for word processing displays. It is believed that the latter application would ease the strain on eyes, for instance for a person looking back and forth at black-on-white text and the screen [62].

The color TFEL technology has the potential to produce high performance color FPDs without the complexity of the TFT (thin film transistor) color LCD approach. The development of efficient primary EL phosphors has been the basic challenge for the realization of a practical full color TFEL display technology.

Two parallel avenues are explored for color EL: 1) the development of an efficient white (or broad band phosphor) that can be filtered to produce an RGB display or 2) the development of efficient red, green and blue primary color EL phosphors. The former approach has the advantage of maintaining the simple device fabrication sequence of a monochrome TFEL display (i.e., no patterning of the thin film phosphor or insulator layers) and achieving RGB colors by laminating a patterned color filter to the EL device at the end of the process.

Also, relative to patterning three different phosphors for an RGB or white display, the filtered approach is much simpler to process.

White EL phosphors based on rare earth doped alkaline earth sulfides for filtered color TFEL devices were first reported by the group at Totorri University in 1987 [63]. Since then, white TFEL displays with singly and doubly activated alkaline earth sulfide phosphor layers have been widely investigated [64-66]. White light emitting EL devices have been fabricated by stacking several combinations of the active layers: · SrS:Ce/SrS:Eu, SrS:Ce/CaS:Eu [67] SrS:Ce/ZnS:Mn [68]. The highest white luminance of 470 nits @ 60 Hz drive frequency has been reported by Planar International using dual layers of SrS:Ce/ZnS:Mn phosphor deposited by atomic layer epitaxy (ALE).

White light emission has also been realized in certain oxide phosphor systems like $CaIn_2O_4$, Sr_2SiO_4 and $SrIn_2O_4$. Partial energy transfer from Ce^{3+} to Eu^{2+} is responsible for white light generation in Sr_2SiO_4:Eu^{2+}, Ce^{3+} [69]. Eu^{2+} has been identified as an efficient sensitizer that transfers energy to Mn^{2+} to result in white light emission under near UV excitation in several phosphor host lattices [70-72]. Singly doped $CaIn_2O_4$:Eu^{3+} [73] emits white by an appropriate selection of the dopant concentration. The combination of multicolor emissions from a single luminescence center leads to white light generation in $SrIn_2O_4$:Dy^{3+} [74].

The present work suggests a novel white oxide phosphor system - $ZnGa_2O_4$:Dy^{3+} - for use in EL devices.

1.7. The $ZnGa_2O_4$ phosphor system - a review

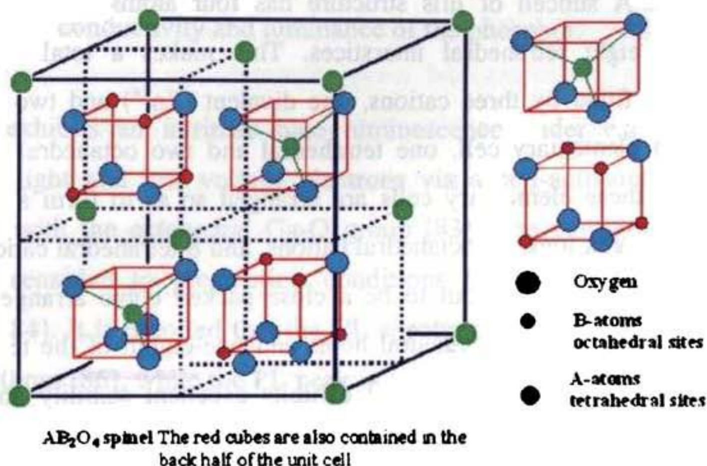

Figure 1.6. Spinel cubic crystal structure of $ZnGa_2O_4$ phosphor

In 1991, Itoh *et al.* [75] was the first to report on a new spinel phosphor system - the $ZnGa_2O_4$. It is a ternary oxide compound of ZnO and Ga_2O_3 comprising of only the fourth row cations. The n-type semiconducting [76] $ZnGa_2O_4$ is unique, being a phosphor with cubic symmetry and having an optical band gap of 4.4 eV rendering the material transparency into the UV region of the electromagnetic spectrum.

Zinc gallium oxide crystallizes in the normal spinel structure that has been interpreted as a combination of rock salt and zinc blende structures (figure1.6) The spinel unit cell belongs to the cubic space group Fd3m (Oh^7) [77] with eight formula units per cell and contains two kinds of cation sites. In this normal spinel, Zn^{2+} ions occupy tetrahedral sites and Ga^{3+} ions occupy octahedral sites

with lattice constant a = 8.37 A^0. The oxygen ions are in face centered cubic closed packing. A subcell of this structure has four atoms, four octahedral interstices and eight tetrahedral interstices. This makes a total of twelve interstices to be filled by three cations, one divalent (Zn^{2+}) and two trivalent (Ga^{3+}). In each elementary cell, one tetrahedral and two octahedral sites are filled. Eight of these elementary cells are arranged so as to form a unit cell containing 32 oxygen ions, 16 octahedral cations, and 8 tetrahedral cations. The spinel structure, hence, turns out to be a close packed cubic arrangement of anions with one-half of the octahedral holes and one-eighth of the tetrahedral holes filled with cations. The material exhibits excellent stability and cubic symmetry in spite of the fact that almost three fourth of the structure is vacant. This is because spinel structures have the ability to accept structural vacancies, thus forming a defect solid solution while remaining as single phase [78].

It is known that oxides with $M^{2+}M_2^{3+}O_4$ spinel structure, in which at least one type of the cation had $d^{10}s^0$ electronic configuration, are promising transparent electroconductive materials. $ZnGa_2O_4$ possess interesting UV transparent electroconductive characteristics and therefore can be used for low voltage applications like FEDs. The conductivity of the material at low energy electron excitation can be improved by modifying the phosphor surface, controlling the activator concentration in the phosphor, and adding conductive material to the host material. Moderate conductivity of 30 S/cm has been reported [76] on annealing bulk $ZnGa_2O_4$ in a reducing atmosphere at high temperatures. Doping with In [79, 80], W [80], Li [81], Sn [82] and Zn [81] has been reported to generate free carriers in the material by increasing the oxygen vacancy creation,

thereby improving its electrical conductivity. Cu [81] doping was found to increase the scattering and trapping probabilities of electrons, subsequently decreasing the conductivity and luminance of the phosphor.

$ZnGa_2O_4$ exhibits an intrinsic blue luminescence under excitation by both ultraviolet light and low voltage electrons via a self-activated optical center associated with the octahedral Ga-O group [83]. The emission properties are relatively sensitive to preparation conditions and Ga/Zn ratio in $ZnGa_2O_4$ phosphor [84]. It is reported that the CL spectra of $ZnGa_2O_4$ has a peak at 457 [85] or 470 nm [86], while the PL peak is located at about 432 [83], 450 [87] or 470-490 nm [88]. The blue emission can be enhanced by In_2O_3 doping [79], replacing the cations in the lattice by Li^+, Na^+ and Ag^+ [89, 90] or the anion in the lattice by S, Se and Te [91]. Moon *et al.* [92] demonstrated that the mixture molar ratio of its constituents, ZnO and Ga_2O_3, also influences the structural and optical properties of $ZnGa_2O_4$ phosphor. Excess ZnO has limit solubility in $ZnGa_2O_4$ phosphor whereas excess Ga_2O_3 is insoluble in $ZnGa_2O_4$ phosphor. Also, the presence of Zn vacancies in the phosphor system causes a blueshift in the luminescent emission.

Kim *et al.* [93] reported that the color of the emission oscillated between ultraviolet (360 nm) and blue (430 nm) by reduction (hydrogen ambient) and oxidation (air ambient), respectively. This ultraviolet luminescence was first considered to originate from the optical center related to gallium at the tetrahedral site in the host [83]. But Kim *et al.* [93] attributed the origin of the 360 nm emission to the Ga-O transition at distorted octahedral sites due to the

presence of oxygen vacancies (V_O*) in $ZnGa_2O_4$ in the reducing ambient and the 430 nm emission to the Ga-O transition at regular octahedral sites without V_O* presence. His arguments were very well supported by electron paramagnetic resonance (EPR) experiments and x-ray photoelectron spectroscopic (XPS) studies. He also observed the 680 nm emission in reduced $ZnGa_2O_4$ arising from oxygen vacancies.

$ZnGa_2O_4$ can be made to emit in the different regions of the visible spectrum by suitably doping it with transition metals or rare-earth elements. Mn^{2+} activated $ZnGa_2O_4$ has been widely investigated as an efficient green emitting phosphor [87]. The material emits green even when doped with Tb [94] or Tm. Activation with Co [95], Cr and Eu [96, 97] gives red and by Ce gives blue. There are reports stating that a systematic tuning (usually, a redshift) of the luminescent properties of self-activated $ZnGa_2O_4$ phosphors is possible by Cd [98] or Si [99] substitution.

Zinc gallate powder phosphors are synthesized by the conventional solid state reaction method which employs high temperature firing (> 1200°C) for highly extended heating times (~ 12 hrs) [88]. Several chemical methods have also been proposed to yield doped and undoped $ZnGa_2O_4$ phosphor particles with improved morphology and luminescent performance. Some of them are multistage precipitation method [100], microencapsulation method [101], combustion synthesis [102], co-precipitation of metal salts [103], aerosol pyrolysis [104] and spray pyrolysis [105] techniques. Citrate-gel [97] and sol-gel [106] techniques have been used in synthesizing zinc gallate phosphors with

high homogeneity and crystallinity at low temperatures. The identification of organic precursors [107] with specific and controlled properties that could finally yield transparent $ZnGa_2O_4$ coatings has also been reported.

Thin films of doped and undoped $ZnGa_2O_4$ are usually deposited by rf magnetron sputtering and pulsed laser ablation techniques. Films are also being deposited using electrophoresis [108] and plasma enhanced chemical vapor deposition (PECVD) [109].

The choice of the substrate had a profound influence on the structural and luminescent properties of $ZnGa_2O_4$ thin film phosphor. The luminescence of the doped or undoped sputtered $ZnGa_2O_4$ thin films improved when deposited on ITO coated glass substrates than on amorphous or Si substrates [110]. As compared to randomly oriented polycrystalline deposits on glass substrates, pulsed laser deposited thin films grown on single crystalline substrates - Si (100), Al_2O_3 (0001) and MgO (100) - gave better luminescence even without post-deposition annealing [111, 112]. This, in fact, reflected the adverse effect of grain boundaries on luminescence properties and suggested that lower defect densities result when films are grown on low energy surfaces. These works also proposed that MgO (100) served as a promising substrate for high quality $ZnGa_2O_4$ film growth.

The crystallinity, morphology and luminescent characteristics of the thin films were found to be highly sensitive to the substrate temperature, Zn/Ga ratio, ambient gas (oxygen) pressure and the temperature and atmosphere chosen for

post-deposition treatments. The films deposited at substrate temperatures ≥ 500°C with (311) spinel peaks showed excellent luminescent performance irrespective of the deposition technique chosen. Slightly Zn deficient films were found to exhibit better luminescent response in comparison to stoichiometric films. Zn/Ga stoichiometry can further be controlled by using mosaic $ZnGa_2O_4$/ZnO ablation targets to compensate for the Zn loss during deposition. The microstructural characteristics of sputter deposited $ZnGa_2O_4$:Mn thin films were also influenced by the energetic particle bombardment on varying the oxygen partial pressure [113]. Post-deposition annealing improved the crystallinity and inturn the luminescent properties of the as-deposited films [114]. The presence of a ZnO [115] or In_2O_3 [116] buffer layer also improved the crystallinity of the as-deposited sputtered films and inturn influence its luminous properties. The incorporation of S [117] and Se [118], as in the bulk, was reported to enhance the PL output of Mn doped zinc gallate thin film phosphors compared to the undoped material by a factor > 3. The addition of Li also was found to enhance the PL and CL properties of undoped and Mn doped $ZnGa_2O_4$ [119].

$ZnGa_2O_4$ has been demonstrated as an excellent host material for multicolor emitting phosphor layers in ACTFEL devices [120]. Minami and his group have fabricated $ZnGa_2O_4$:Mn active ACTFEL devices using the single insulating layered structure. The phosphor layers were sputter deposited onto thick ceramic sheets of $BaTiO_3$. ZnO:Al/ITO and Al/Ag were used as top and bottom electrodes respectively. The as-deposited devices were post-annealed at 1020°C for 5 hrs in argon ambient [120-122] or subjected to insitu RTA (rapid thermal

annealing) [123] to improve their performance. These devices gave a green EL emission with luminance over 600 cd/m^2 and an efficiency approaching 1 lm/W when driven at 1 KHz. Devices were also fabricated using low pressure chemical vapor deposition [100] and dip-coating [124] techniques for depositing the light emitting layers. Flynn et al. [125] has reported TFEL studies of $ZnGa_2O_4$:Mn with an effort to investigate the EL characteristics of the phosphor when post-annealed at lower temperatures. ACPEL devices have also been fabricated by several groups using Mn (Cr) activated $ZnGa_2O_4$ as the active layer with luminescent efficiency approaching 15 (13) lm/W [126, 127].

White luminescence have been reported in Li doped $ZnGa_2O_4$ for the composition [$0.9ZnGa_2O_4$ + $0.1LiGaO_2$], the chromaticity coordinates being (0.25, 0.34) [128]. Bismuth ion doped lithium zinc gallate ($ZnGa_2O_4$:$0.001Bi^{3+}$, $0.175Li^{+}$) [129] also gives white emission with color coordinates (0.31, 0.33). Yang *et al.* [130] reports on the luminescence properties of a white $ZnGa_2O_4$/ZnO/ITO/glass phosphor screen deposited via sputtering.

Being an oxygen deficient spinel, $ZnGa_2O_4$ system has been studied to design a liquid petroleum gas sensor with high selectivity and sensitivity [131]. Recently, Risbud *et al.* [132] reported that a long range ferromagnetic order can be observed in Fe doped $ZnGa_2O_4$ at a relatively high temperature of 200 K. Long period phosphorescence has also been reported in $ZnGa_2O_4$:Mn phosphors [133]. $ZnGa_2O_4$: Mn^{2+}, a well known green emitter, is widely used in cathode ray tubes, image intensifiers, television screens, etc. Zinc gallate phosphors have gained much attention for use in VFDs and FEDs, being an efficient low voltage

cathodoluminescent (LVCL) phosphor. The cubic spinel $ZnGa_2O_4$ therefore shows excellent potential for incorporation in future display systems.

1.8. Relevance of the present work

There is a continuing potential for commercialization of spinel oxide phosphors. In the present work, attempts are made to reduce the processing temperature of $ZnGa_2O_4$ so that the relatively inexpensive glass substrates and plastics can, in future, be used in ACTFEL device fabrication. Also, a novel white phosphor system - singly activated $ZnGa_2O_4$ - was investigated since the identification of new multicolor or white light emitting phosphor materials is a major challenge in the area of FPD technology.

References

1. G. Wiedemann, *Ann. Phys. Chem.*, **34**, 446 (1888).
2. A. S. Marfunin, *Spectroscopy, Luminescence and Radiation Centers in Minerals*, translated by V. V. Schiffer, p.151, Springer-Verlag, New York (1979).
3. D. R. Vij (Ed.), *Luminescence of Solids*, p.109, Plenum Press, New York (1998).
4. C. W. E. van Eijk, *J. Lumin.*, **60-61**, 936 (1994).
5. H. Gudden, R. W. Pohl, *Z. Phys. A: Hadrons Nucl.*, **2**, 192 (1920).
6. G. Destriau, *J. Chim. Physique* (France), **33**, 587 (1936).

7. T. Inoguchi, M. Takeda, Y. Kakihara, Y. Nakata and M. Yoshida, *Digest of 1974 SID International Symposium* (1974) 84.
8. M. J. Russ and D. I. Kennedy, *J. Electrochem. Soc.*, **114**, 1066 (1967).
9. P. D. Rack, A. Naman, P. H. Holloway, S. S. Sun, R. T. Tuenge, *MRS Bull.*, **21**, 49 (1996).
10. B. Qiao, Z. L. Tang, Z. T. Zhang, L. Chen, *Mater. Lett.*, **61**, 401 (2007).
11. J. S. Kim, S. G. Lee, H. L. Park, J. Y. Park and S. D. Han, *Mater. Lett.*, **58**, 1354 (2004).
12. G. A. Hirata, J. Mckittrick, M. A. Borja, J. M. Siqueiros, D. Devlin, *Appl. Surf. Sci.*, **113/114**, 509 (1997).
13. R. Khormaei, S. Thayer, K. Ping, C. Kin g, G. Dolney, A. Ipri, F. L. Hsueh, R. Stewart, T. Keyser, G. Becker, D. Kagey and M. Spitzer, *Digest of 1994 SID International Symposium* (1994) 137.
14. P. Bailey, D. Carkner and X. Wu, *Digest of 1995 SID International Symposium* (1995) 484.
15. P. M. Alt, *Digest of 1984 SID International Symposium* (1984) 79.
16. Y. A. Ono, *Electroluminescent displays*, p.26, World scientific, Singapore (1995).
17. J. D. Davidson, J. F. Wager and I. Khormaei, *Digest of 1991 SID International Symposium* (1991) 77.
18. A. A. Douglas and J. F. Wager, *Digest of 1992 SID International Symposium* (1992) 356.
19. D. H. Smith, *J. Lumin..*, **23**, 209 (1981).
20. K. W. C. Yang and S. J. T. Owen, *IEEE Trans. El. Dev.*, **30**, 452 (1983).

21. S. Kobayashi, J.F. Wager and A. A. Dayah, *Proc. Sixth International Workshop on Electrolminescence* (1992) 234.
22. K. Miyashita and M. Shibata, *Japan Display '93* (1993) 100.
23. S. Bhaskaran, V. P. Singh and D. C. Morton, *IEEE Trans. El. Dev.*, **42**, 1756 (1995).
24. H. Kobayashi, R. Tueta, and R. Menn, *IEEE Trans. El. Dev.*, **29**, 1626 (1982).
25. J. Ohwaki, H. Kozawaguchi. B. Tsujiyama, *J. Electrochem. Soc.*, **137**, 340 (1990).
26. J. D. Britton, J. C. McClure and V. P. Singh, *Proc. Sixth International Workshop on Electrolminescence* (1992) 286.
27. P. D. Rack, P. H. Holloway, L. Pham, J. F. Wager and S. S. Sun, *Digest of 1995 SID International Symposium* (1995) 480.
28. K. Bhattacharypa, S.M. Goodnick and J.F. Wager, *J. Appl. Phys.*, **73**, 3390 (1993).
29. H. Frohlich, *Adv. Phys.*, **3**, 325 (1954).
30. K. Brennan, *J. Appl. Phys.*, **64**, 4024 (1988).
31. E. Bringuier, *J. Appl. Phys.*, **70**, 4505 (1991).
32. E. Bringuier, *J. Appl. Phys.*, **75**, 4291 (1994).
33. R. Mach and G. O. Muller, *J. Cryst. Growth*, **101**, 967 (1990).
34. E. Bringuier, *J. Appl. Phys.*, **67**, 7040 (1990).
35. R. Mach and G. O. Muller, *Phys. Status Solidi A*, **81**, 609 (1984).
36. V. Marello, L. Samuelson, A. Onton and W. Reuter, *J. Appl. Phys.*, **52**, 3590 (1981).
37. P. D. Keir, M.S. thesis, Oregon State University, p.78, 1999.

38. S. L. Jones, D. Kumar, R. K. Singh and P. H. Holloway, *Appl. Phys. Lett.*, **71**, 404 (1997).
39. J. S. Bae, J. H. Jeong, S. S. Yi and J. C. Park, *J. Appl. Phys.*, **82**, 3629 (2003).
40. T. Minami, H. Yamada, Y. Kubota and T. Miyata, *Jpn. J. Appl. Phys.*, **36**, L1191 (1997).
41. T. Xiao, A. H. Kitai, G. Liu, A. Nakua and J. Barbier, *Appl. Phys. Lett.*, **72**, 3356 (1998).
42. S. Bhushan, A. N. Pandey and B. R. Kaza, *J. Lumin.*, **20**, 29 (1979).
43. S. Takata, T. Minami and H. Nanto, *Jpn. J. Appl. Phys.*, **20**, 1759 (1981).
44. P. Thiyagarajan, M. Kottaisamy and M. S. R. Rao, *J, Electrochem. Soc.*, **154**, H297 (2007).
45. Z. Lou and J. Hao, *Appl. Phys. A*, **80**, 151 (2005).
46. L. Xiao, M. He, Y. Tian, Y. Chen, T. Karak, L. Zhang and N. Wang, *Jpn. J. Appl. Phys.*, **46**, 5871 (2007).
47. K. N. Kim, H. K. Jung, H. D. Park and D. Kim, *J. Lumin.*, **99**, 169 (2002).
48. Y. D. Jiang, F. Zhang, C. J. Summers and Z. L. Wang, *Appl. Phys. Lett.*, **74**, 1677 (1999).
49. V. P. Singh, T. K. G. Rao and J. J. Zhu, *J. Lumin.*, **128**, 583 (2008).
50. V. P. Singh, T. K. G. Rao and J. J. Zhu, *J. Lumin.*, **126**, 1 (2007).
51. S. Itoh, H. Toki, K. Tamura and F. Kataoka, *Jpn. J. Appl. Phys.*, **38**, 6387 (1999).
52. K. S. Sohn, B. Cho, H. D. Park, Y. G. Choi and K. H. Kim, *J. Eur. Ceram. Soc.*, **20**, 1043 (2000).

53. Q. Y. Zhang, K. Pita, W. Ye and W. X. Que, *Chem. Phys. Lett.*, **351**, 163 (2002).
54. S. H. Shin, D. Y. Jeon and K. S. Suh, *Jpn. J. Appl. Phys.*, **40**, 4715 (2001).
55. T. Minami, T. Miyata, S. Takata and I. Fukuda, *Jpn. J. Appl. Phys.*, **30**, L117 (1991).
56. X. Ouyang, A. H. Kitai and T. Xiao, *J. Appl. Phys.*, **79**, 3229 (1996).
57. G. Stuyven, P. D. Visschere, K. Neyts, and A. Kitai, *J. Appl. Phys.*, **93**, 4622 (2003).
58. J. P. Bender, J. F. Wager, J. Kissick, B. L. Clark and D. A. Keszler, *J. Lumin.*, **99**, 311 (2002).
59. P. Wellenius, A. Suresh and J. F. Muth, *Appl. Phys. Lett.*, **92**, 021111 (2008).
60. T. Minami, Y. Kobayashi, T. Shirai, T. Miyata and S. Suzuki, *Jpn. J. Appl. Phys.*, **41**, L478 (2002).
61. T. Minami, Y. Kobayashi, T. Miyata and S. Suzuki, *Jpn. J. Appl. Phys.*, **41**, L577 (2002).
62. Y. A. Ono, M. Fuyama, K. Onisawa, K. Tamura and M. Ando, *J. Appl. Phys.*, **66**, 5564 (1989).
63. S. Tanaka, H. Yoshiyama, J. Nishiura, S. Ohshio, H. Kawakami and H. Kobayashi, *Appl. Phys. Lett.*, **51**, 1661 (1987).
64. S. Okamoto, E. Nakazawa and Y. Tsuchiya, *Jpn. J. Appl. Phys.*, **29**, 1987 (1990).
65. S. Tanaka, S. Ohshio, J. Nishiura, H. Kawakami, H. Yoshiyama and H. Kobayashi, *Appl. Phys. Lett.*, **52**, 2102 (1988).

66. W. Kong, J. Fogarty, R. Solanki and R. T. Tuenge, *Appl. Phys. Lett.*, **66**, 419 (1995).
67. Y. A. Ono, M. Fuyama, K. Onisawa, K. Tamura and M. Ando, *J. Appl. Phys.*, **66**, 5564 (1989).
68. J. A. Ruffner, R. T. Tuenge, S. S. Sun, P. D. Grandon and P. F. Hlava, *Thin Solid Films*, **310**, 123 (1997).
69. N. Lakshminarasimmhan and U. V. Varadaraju, *J. Electrochem. Soc.*, **152**, H152 (2005).
70. W. J. Yang, L. Luo, T. M. Chen and N. S. Wang, *Chem. Mater.*, **17**, 3883 (2005).
71. W. J. Yang and T. M. Chen, *Appl. Phys. Lett.*, **88**, 101903 (2006).
72. S. H. Lee, J. H. Park, S. M. Son, J. S. Kim and H. L. Park, *Appl. Phys. Lett.*, **89**, 221916 (2006).
73. X. Liu, C. Lin and J. Lin, *Appl. Phys. Lett.*, **90**, 081904 (2007).
74. X. Liu, C. Lin, Y. Luo and J. Lin, *J. Electrochem. Soc.*, **154**, J21 (2007).
75. S. Itoh, H. Toki, Y. Sato, K. Morimoto and T. Kishino, *J. Electrochem. Soc.*, **138**, 1509 (1991).
76. T. Omata, N. Ueda, K. Ueda and H. Kawazoe, *Appl. Phys. Lett.*, **64**, 1077 (1994).
77. K. E. Sickafus, J. M. Wills, and N. W. Grimes, *J. Am. Chem. Soc.*, **82**, 3279 (1999).
78. A.F. Wells, *Structural Inorganic Chemistry*, Fifth edition, p.334, Clarendon Press, Oxford (1984).
79. S. H. Yang and M. Yokoyama, *J. Vac. Sci. Technol. A*, **19**, 2463 (2001).
80. S. H. Yang, *J. Electron. Mater.*, **33**, L1 (2004).

81. S. H. Yang and M. Yokoyama, *Jpn. J. Appl. Phys.*, **37**, 6429 (1998).
82. K. Mini Krishna, M. Nisha, R. Reshmi, R. Manoj, A.S. Asha and M.K.Jayaraj, *Mater. Forum*, **29**, 243 (2005).
83. I. K. Jeong, H. L. Park and S. I. Mho, *Solid State Commun.*, **105**, 179 (1998).
84. M. Yu, J. Lin, Y. H. Zhou and S. B. Wang, *Mater. Lett.*, **56**, 1007 (2002).
85. C. F. Yu and P. Lin, *J. Appl. Phys.*, **79**, 7191 (1996).
86. I. J. Hsieh, M. S. Feng, K. T. Kudo, P. Lin, *J. Electrochem. Soc.*, **14**, 1617 (1994).
87. L. E. Shea, R. K. Datta and J. J. Brown, Jr., *J. Electrochem. Soc.*, **141**, 1950 (1994).
88. K. H. Hsu, M. R. Yang and K. S. Chen, *J. Mater. Sci.- Mater. Electron.*, **9**, 283 (1998).
89. J. S. Kim, H. L. Park, G. C. Kim, T. W. Kim, Y. H. Hwang, H. K. Kim, S. I. Mho and S. D. Han, *Solid State Commun.*, **126**, 515 (2003).
90. K. G. Lee, K. H. Park, B. Y. Yu, C. H. Pyun, C. H. Kim, H. L. Park and S. I. Mho, *Mater. Res. Bull.*, **37**, 1071 (2002).
91. H. I. Kang, J. S. Kim, H. L. Park, G. C. Kim, T. W. Kim, Y. H. Hwang, S. I. Mho and C. Lee, *Mater. Res. Bull.*, **37**, 1923 (2002).
92. J. W. Moon, H. S. Moon, E. S. Oh, H. I. Kang, J. S. Kim, H. L. Park and T. W. Kim, *Int. J. Inorg. Mater.*, **3**, 575 (2001).
93. J. S. Kim, H. I. Kang, W. N. Kim, J. I. Kim, J. C. Choi, H. L. Park, G. C. Kim, T. W. Kim, Y. H. Hwang, S. I. Mho, M. C. Jung and M. Han, *Appl. Phys. Lett.*, **82**, 2029 (2003).
94. Z. Xu, Y. Li, Z. Liu and D. Wang, *J. Alloys Compd.*, **391**, 202 (2005).

95. T. Abritta and F.H. Blak, *J. Lumin.*, **48/49**, 558 (1991).

96. P. D. Rack, J. J. Peterson, M. D. Potter and W. Park, *J. Mater. Res.*, **16**, 1429 (2001).

97. M. Yu, J. Lin, Y. H. Zhou, S. B. Wang, *Mater. Lett.*, **56**, 1007 (2002).

98. T. M. Chen and Y. W. Chen, *J. Solid State Chem.*, **150**, 204 (2000).

99. H. I. Kang, J. S. Kim, M. Lee, J. H. Bahng, J. C. Choi, H. L. Park, G. C. Kim, T. W. Kim, Y. H. Hwang, S. I. Mho, S. H. Eom, Y. S. Yu, H. J. Song and W. T. Kim, *Solid State Commun.*, **122**, 633 (2002).

100. H. K. Jung, D. S. Park and Y. C. Park, *Mater. Res. Bull.*, **34**, 43 (1999).

101. K. H. Hsu and K. S. Chen, *Ceram. Int.*, **26**, 469 (2000).

102. J. Y. Kim, J. H. Kang, D. C. Lee and D. Y. Jeon, *J. Vac. Sci. Technol. B*, **21**, 532 (2003).

103. J. G. Kho, H. D. Park and D. P. Kim, *Bull. Korean Chem. Soc.*, **20**, 1035 (1999).

104. Y. K. Yoo, G. Y, Hong, S. H. Cho and J. S. Yoo, *J. Electrochem. Soc.*, **148**, H109 (2001).

105. H. S. Roh, Y. C. Kang, S. B. Park and H. D. Park, *Jpn. J. Appl. Phys.*, **41**, 4559 (2002).

106. Jong S. Kim, Jin S. Kim, T. W. Kim, S. M. Kim and H. L. Park, *Appl. Phys. Lett.*, **86**, 091912 (2005).

107. D. H. Jo, H. K. Jung, S. Seok and D. S. Park, *Bull. Korean Chem. Soc.*, **18**, 609 (1997).

108. S. H. Yang, *J. Electrochem. Soc.*, **150**, H250 (2003).

109. T. Minami, Y. Kuroi and S. Takata, *J. Vac. Sci Technol. A*, **14**, 1736 (1996).

110. Y. J. Kim, Y. H. Jeong, K. D. Kim, S. G. Kang, K. G. Lee, J. I. Han, Y. K. Park and K. I. Cho, *J. Vac. Sci. Technol. B*, **16**, 1239 (1998).
111. S. S. Yi, I. W. Kim, H. L. Park, J. S. Bae, B. K. Moon and J. H. Jeong, *J. Cryst. Growth*, **247**, 213 (2003).
112. Y. E. Lee, D. P. Norton and J. D. Budai, *Appl. Phys. Lett.*, **74**, 3155 (1999).
113. J. H. Kim and P. H. Holloway, *J. Vac. Sci. Technol. A*, **24**, 2164 (2006).
114. S. M. Chung and Y. J. Kim, *J. Vac. Sci. Technol. A*, **22**, 140 (2004).
115. Y. J. Kim, S. M. Chung, Y. H. Jeong and Y. E. Lee, *J. Vac. Sci. Technol. A*, **19**, 1095 (2001).
116. S. H. Yang, C. Y. Lu and S. J. Chang, *J. Electrochem. Soc.*, **154**, J229 (2007).
117. J. S. Bae, Y. H. Kim, J. K. Jang, K. S. Shim, J. K. Lee, J. H. Jeong, S. S. Yi and H. L. Park, *Appl. Phys. A,* **78**, 1073 (2004).
118. J. H. Jeong, B. K. Moon, H. J. Seo, J. S. Bae, S. S. Yi, I. W. Kim and H. L. Park, *Appl. Phys. Lett.*, **83**, 1346 (2003).
119. Y. E. Lee, D. P. Norton, J. D. Budai, P. D. Rack, J. Peterson and M. D. Potter, *J. Appl. Phys.*, **91**, 2974 (2002).
120. T. Minami, Y. Kuroi, T. Miyata, H. Yamada and S. Takata, *J. Lumin.*, **72-74**, 997 (1997).
121. T. Minami, T. Maeno, Y. Kuroi and S. Takata, *Jpn. J. Appl. Phys.*, **34**, L684 (1995).
122. T. Minami, S. Takata, Y. Kuroi and T. Maeno, *J. Soc. Inf. Disp.*, **4**, 53 (1996).

123. T. Minami, H. Toda and T. Miyata, *J. Vac. Sci Technol. A*, **19**, 1742 (2001).

124. T. Minami, T. Miyata and Y. Sakagami, *Surf. Coat. Technol.*, **108-109**, 594 (1998).

125. M. Flynn and A. H. Kitai, *J. Electrochem. Soc.*, **148**, H149 (2001).

126. J. S. Kim, S. G. Lee, H. L. Park, J. Y. Park and S. D. Han, *Mater. Lett.*, **58**, 1354 (2004).

127. B. Qiao, Z. L. Tang, Z. T. Zhang and L. Chen, *Mater. Lett.*, **61**, 401 (2007).

128. K. H. Park, H. L. Park and S. I. Mho, *J. Lumin.*, **93**, 205 (2001).

129. W. N. Kim, H. L. Park and G. C. Kim, *Mater. Lett.*, **59**, 2433 (2005).

130. S. H. Yang, T. J. Hsueh and S. J. Chang, *Jpn. J. Appl. Phys.*, **46**, 4166 (2007).

131. L. Satyanarayana, C. V. Gopal Reddy, S. V. Manorama and V. J. Rao, *Sens. Actuators B*, **46**, 1 (1998).

132. A. S. Risbud, R. Seshadri, J. Ensling and C. Felser, *J. Phys.: Condens. Matter*, **17**, 1003 (2005).

133. K. Uheda, T. Maruyama, H. Takizawa and T. Endo, *J. Alloys Compd.*, **262-263**, 60 (1997).

Chapter 2

Experimental and analytical techniques

2.1. Introduction

Growth techniques do play a significant role in influencing the physico-chemical characteristics of bulk powders as well as thin films. It is also observed that various physical constants, characteristic to a bulk material, need not remain the same in their corresponding thin films. The structural, electrical and optical properties of thin films are found to be highly sensitive to the technique adopted, the substrate chosen, deposition conditions, the presence of defects and impurities and the film thickness. The appropriate choice of an experimental technique thereby helps in tailoring a material with controlled, reproducible and well defined properties so as to suit a technological application.

The present work was aimed at the growth of oxide phosphors for thin film electroluminescent (TFEL) applications. Vacuum deposition techniques such as pulsed laser deposition (PLD), radio frequency (rf) magnetron sputtering and thermal evaporation were employed for thin film growth. PLD was used for growing pristine zinc gallate thin films at room temperature. Rf magnetron sputtering served to deposit dysprosium doped zinc gallate thin films. The active layer, buffer layer and the insulator layers of the TFEL device fabricated were also accomplished via rf magnetron sputtering technique. Thermal evaporation was used to deposit metal electrodes (aluminum, indium) to complete the device structure for optical characterization. The present chapter discusses the various methodologies adopted for bulk synthesis and thin film growth. It also briefs on the different analytical tools used in the present study.

2.2. Bulk synthesis

The targets of source materials, for both PLD and sputtering techniques, were synthesized in the laboratory from highly pure starting materials. A one inch pellet of pure $ZnGa_2O_4$ was used as the target for the PLD work. Powder targets were used for the sputter deposition of $ZnGa_2O_4:Dy^{3+}$, ZnO and $BaTa_2O_6$.

For preparing bulk phosphor powders, stoichiometric quantities of the starting materials were thoroughly hand mixed in alcohol medium using an agate mortar and pestle. The dried mixture was then placed in an alumina boat and introduced into the hot temperature zone of a horizontal tube furnace equipped with a proportional integral differential (PID) controller. The firing was done at the requisite temperature over a fixed time.

A two step firing process is usually adopted for pellet synthesis. The constituent materials, after thorough mixing, are pre-fired before being pressed into a pellet to allow the complete reaction of the powder mixture. This powder is then taken in a 1" diameter steel die and pressed into a one inch diameter pellet using a hydraulic press applying a force of 2 tons. The pellet is then post-fired for sintering to ensure better thin film growth. During the second firing process, the temperature is to be raised in steps to completely remove moisture from the target. Moisture, if trapped inside the target, leads to cracking during firing. Normally, the outer part of a target heats up faster than the inner part. If the temperature were increased too quickly from room temperature to the high

processing temperature, the outer part of the target would become dense before the moisture in the inner part escapes.

A solid and highly condensed pellet with reduced porosity is desirable for pulsed laser deposition to arrest cracking due to high thermal conductivity on exposure to the high energy laser. A large press loading can reduce porosity in the target but overloading during pressing results in a cracked target. The pore density can be measured from the following relation,

Pore density = Actual mass density / Theoretical mass density

where,

Actual mass density = Target weight / Target Volume

Theoretical mass density = Weight of all atoms in the primary cell / Volume of the primary cell

The $ZnGa_2O_4$ primary unit contains eight $ZnGa_2O_4$ molecules and each $ZnGa_2O_4$ molecule contains one Zn atom, two Ga atoms and four O atoms. For the synthesized $ZnGa_2O_4$ pellet crystallizing in the cubic spinel structure,

Actual mass density = Weight of the target / (π* (radius of the target)^2 * height of the target)

Theoretical mass density = 8*{At. wt. (Zn) + 2*At. wt. (Ga) + 4*At. wt. (O)}/a^3

The pore density was hence found to be 0.33.

Box furnace annealing was used for the post-deposition annealing treatments of the grown films. Such heat treatments were needed for re-crystallization of phosphor thin films for enhanced luminescent output.

2.3. Thin film growth techniques

A 'thin film' has one of its linear dimensions very small compared to the other two and is characterized by a large surface to volume ratio. Any thin film deposition process involves the following sequential steps:

1) Transition of the condensed phase (solid or liquid) into the gaseous state (atomic/molecular/ionic species)
2) Transport of the vapor from the source to the substrate
3) Condensation of the vapor upon arrival on the substrate

The deposition techniques are broadly classified into two - physical and chemical - depending on how the atoms/molecules/ions/clusters of species are created for condensation process [1].

Various chemical methods have been realized for thin film deposition of phosphor materials. Some of them are sol-gel synthesis [2, 3], solvent evaporation epitaxy method [4], electrophoresis [5], spray pyrolysis [6, 7] and dip-coating [8]. Thermal and electron beam evaporation, pulsed ion beam evaporation [9], chemical vapor deposition (CVD) [10], PLD, rf sputtering, and atomic layer epitaxy (ALE) falls under the stream of physical methods generally adopted for thin film phosphor growth.

The following sections briefs the various thin film deposition techniques used in the present work.

2.3.1. Thermal evaporation by resistive heating

Thermal evaporation is a simple and convenient technique widely used for the deposition of thin films of metals, alloys and many compounds. The process, in general, involves heating up of a source material until it evaporates and condenses on a cold target surface, referred to as the substrate.

If carried out in vacuum, the evaporation temperature can be considerably lowered and the formation of oxides and incorporation of impurities in the growing layer can be avoided. Moreover, at pressures as low as 10^{-6} or 10^{-5} Torr, the mean free path of vapor atoms shall be of the same order as the vacuum chamber dimensions. Hence, the particles can travel in straight lines from the evaporation source towards the substrate without being significantly scattered [11].

In thermal evaporation technique, the average energy of vapor atoms reaching the substrate surface is generally low (of the order of kT ie. tens of eV). Here, a refractory metal (tungsten or tantalum) strip or shaped filaments are heated directly by attaching the ends to a low voltage, high current supply to evaporate the charge. The characteristics and quality of the deposited film shall depend on the substrate temperature, rate of deposition, substrate to target distance, base pressure, etc. The homogeneity of the film depends on the geometry of the evaporation source and the distance from the source material to the substrate. Excellent and detailed reviews on the know-how of the technique have been discussed by Holland [12].

In the present work, the deposition of metal electrodes (Al) was done using thermal evaporation via resistive heating.

2.3.2 Sputtering

Sputtering is one of the most versatile techniques used for the deposition of high quality thin films over a larger area with better control of composition and thickness, greater adhesion and homogeneity. The process involves the creation of inert gas plasma, usually of argon [13], by applying a high voltage between electrodes. The target holder is generally taken as the cathode and the substrate holder as the anode. The source material is subjected to intense bombardment by heavy argon ions. By momentum transfer, particles are knocked out from the target surface and they travel across the system to condense onto the substrate surface. The process, if carried out in vacuum, becomes more efficient since the sputtered material will arrive at the substrate surface without suffering collisions with the residual gas with energy enough to produce a fine coating. Sputtering is normally performed at a pressure of 10^{-2} to 10^{-3} Torr. At such high residual gas pressures, the sputtered material is seldom transferred towards the substrate without many collisions. This gives rise to very slow deposition rate and poor quality coating.

Sputtering may be carried out in a variety of systems, which may differ in sputtering configuration, geometry, target type etc. Experimental sputtering systems usually have small targets and low production rates, whereas commercial production systems have large targets and rapid substrate transport

to maximize production rate. Irrespective of the sputtering system used, the basic sputtering process remains the same. A schematic diagram of the rf sputtering system is shown in figure 2.1.

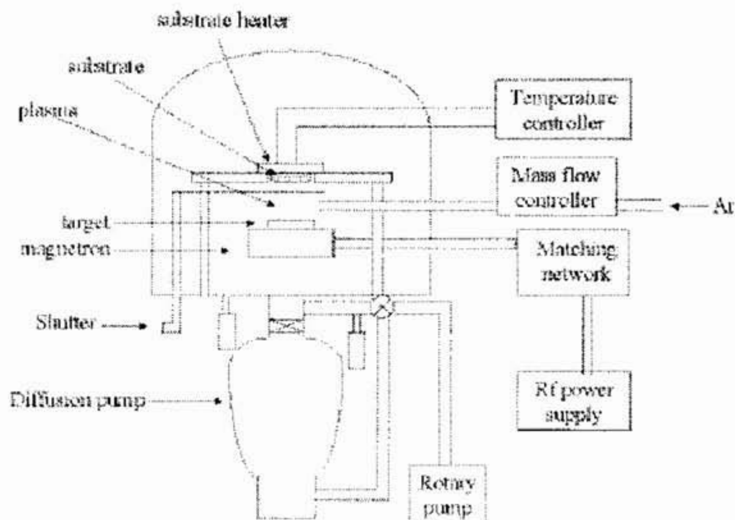

Figure 2.1. Rf sputter deposition system

Normally there are two modes of powering the sputtering system - dc and rf biasing. In dc sputtering, a direct voltage is applied between the cathode and the anode. This method is restricted for conducting materials only. The process is inadequate for the deposition of dielectric films because of charging, arcing, and very low deposition rates. Radio frequency (rf) sputtering is suitable for both conducting and nonconducting materials. A high frequency generator (13.56 MHz) is connected between the electrodes of the system. The oscillating rf potential applied between the anode and cathode modifies the electron motions, which produces better energy coupling to the electrons as well as higher plasma

densities. A large capacitor (500-2000 pF), placed in series between the rf power supply and the powered electrode, allows a significant negative bias to develop on the cathode, typically half of the value of the applied peak-to-peak rf voltage. This bias is then the acceleration voltage for ions from the plasma, which move much too slowly to respond to the applied rf potentials. In addition to the series capacitor, usually, two other tuning components help in matching the impedance of the plasma to the output impedance of the rf power supply. These components, usually a shunt capacitor to ground and a series inductor, are located along with the series capacitor in the "matching network". The inductor is fixed, and both of the capacitors (shunt and series) are variable. The reflected power is minimized by adjusting these variable capacitors in the tuning network. In rf sputtering, the substrate functions as partial cathodes in the circuit and are bombarded by ions from the plasma, albeit at a lower rate than the primary cathode.

Magnetron sputtering uses a magnetic field to confine the electrons close to the cathode, making it easier to sustain an electrical discharge at low pressure. The conventional, circular planar cathode is characterized by high levels of erosion on the cathode surface in the form of a ring. This technique is particularly useful when high deposition rates and low substrate temperatures are required [14]. Both reactive and nonreactive forms of dc, rf and magnetron sputtering have been employed for the deposition of compound semiconductors. In reactive sputtering, the reactive gas is introduced into the sputtering chamber along with argon to deposit thin films. For example to deposit metal oxide thin films pure metal target is sputtered in a mixture of argon and oxygen atmosphere. The

deposition rates and properties of the films strongly depend on the sputtering conditions such as the partial pressure of the reactive gas, the sputtering pressure, substrate temperature and substrate to target spacing.

In sputter deposition, the material arrives at the substrate mostly in atomic or molecular form. The atom diffuses around the substrate with a motion determined by its binding energy to the substrate, which is influenced by the nature and temperature of the substrate. The depressions on the substrate surface act as adsorption sites for the diffusing atoms. At each hop, the atom will either jump over the barrier into an adjacent site or will re-evaporate. After a certain time, the atom will either evaporate from the surface or will join another diffusing single atom to form a doublet. These doublets will be joined by other single atoms to form triplets, quadruplets and so on. This stage is known as the nucleation stage of thin film growth and it leads to the formation of quasi-stable islands. The islands will grow in size and it will lead to the coalescent stage. Coalescence proceeds until the film reaches continuity.

The process of rf sputter deposition is made possible due to the large difference in mass, and hence mobility, of electrons and inert gas ions. Being less massive than ions, electrons attain much greater velocities and travel much further than ions during each cycle of the applied rf voltage waveform. Hence they eventually accumulate on the target, substrate and chamber walls such that the plasma is the most positive potential in the system. These induced negative voltages or "sheath voltages" [15] causes acceleration of positive ions toward the negatively charged surfaces, which subsequently leads to sputtering events. The

volume adjacent to the cathode surface relatively free of electrons leads to a "dark space" because electrons are not available to excite gas atoms. The target is selectively sputtered by controlling the relative surface areas of the target and the substrate holder. If space charge limited current is assumed, the ion current flux, J can be estimated by the Child-Langmuir equation [16],

$$J = \frac{KV^{3/2}}{D^2 m_{ion}} \tag{2.1}$$

where, D is the dark space thickness, V is the sheath voltage, m_{ion} is the ionic mass and K is the proportionality constant. Since the positive ion current must be equal at both the electrodes,

$$\frac{A_A V_A}{D_A^2} = \frac{A_B V_B}{D_B^2} \tag{2.2}$$

where, A_A and A_B are the surface areas of cathode and anode A and B respectively. If positive ion current densities were assumed to be equal, there would be a much greater positive ion current flowing during one half cycle of the applied voltage waveform than the other due to the much greater area of the grounded substrate electrode. Here, as the system is assumed to be in steady state, the total positive ion current per half cycle should be the relevant quantity.

The glow discharge itself is a region where large quantities of positive and negative charge exist and can be modelled as a wire. Since most of the voltage in the glow discharge is dropped across the dark space, and they have small conductivities, they can be modelled as capacitors such that the capacitance C,

$$C \alpha\ A/D \tag{2.3}$$

Furthermore, an ac voltage will divide across the two series capacitors such that,

$$\frac{V_A}{V_B} = \frac{C_B}{C_A} \tag{2.4}$$

$$\therefore \frac{V_A}{V_B} = \left(\frac{A_B}{A_A}\right)^2 \tag{2.5}$$

This equation tells that smaller area will see larger sheath voltage, whereas larger area will see a smaller sheath voltage by a power of 2. The usefulness of this result is that $A_B > A_A$ must hold to selectively sputter the target. This is done in practice by grounding the substrate holder to the entire chamber resulting in a very large A_B. For this reason it is extremely important that the substrate holder and the system are well grounded to ensure that re-sputtering of the growing film does not occur.

Sputtering yield is defined as the quantity of the material sputtered per ion (atoms/ion or grams/ion) [17]. Main features observed for the sputtering technique are:

1) Sputtering yield differs with the nature of the element ie., the yield increases as the reciprocal of the binding energy of the surface atoms.
2) Sputtering yield decreases as the surface damage increases i.e. the yield from a rougher surface is lower than that from a smoother surface.
3) As the mass of the sputtering species increases, the sputtering yield increases.
4) Lighter mass ions penetrate deeper into the target than heavier mass ions.

5) As sputtering energy increases, the sputtering yield increases up to 10-100 keV. At higher energies, the sputtering yield again decreases since the ions penetrate into the target. Since smaller particles penetrate further into the target, the energy when the yield starts to decrease is lower for lighter particles.
6) For multicomponent samples, the lightweight particle is usually preferentially sputtered if the binding energies of the components are similar. The sputtering rate of each component increases as the reciprocal of the binding energy and mass of that component.
7) Sputtering of oxide targets result in preferential depletion of oxygen.
8) Sputtering yield of metal oxide is less than that of corresponding metals.
9) For oxide samples, sputtering in an oxygen rich environment decreases the sputtering yield; the sputtering yield does not vary in other environments (for example, CO and N_2) indicating that adsorption without chemical bonding is not enough to reduce the sputtering yield.

In the present study, an in-house assembled magnetron has been used for rf magnetron sputtering of dysprosium doped zinc gallium oxide and barium tantalum oxide. A magnet of 2000 gauss was used to deflect the ions. A schematic diagram of the magnetron is shown in figure 2.2. The vacuum system consists of a 6" diameter diffusion pump backed by a rotary pump (make - Indovision, Bangalore). The rf supply was connected to the magnetron through a capacitive matching network (make–Digilog Instruments, Bangalore). The flow of argon gas into the vacuum chamber was controlled using a mass flow controller (make Bronkhorst, Holland).

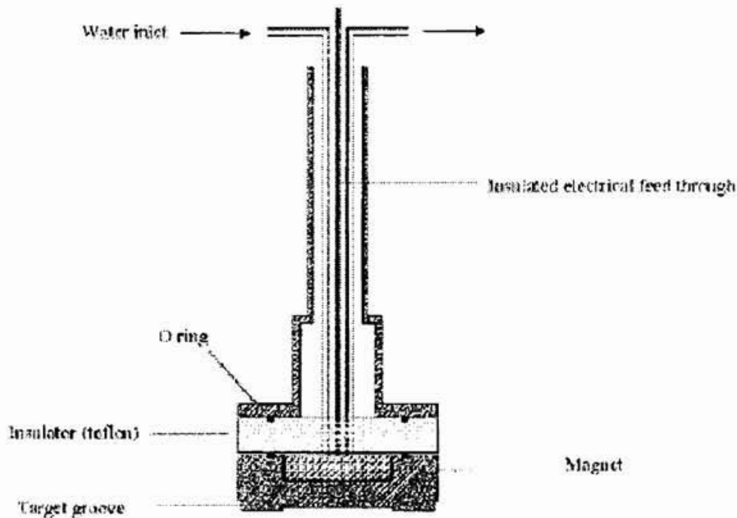

Figure 2.2. Schematic structure of the magnetron

2.3.3 Pulsed laser deposition (PLD)

Lasers are energy sources in the form of monochromatic and coherent photons, enjoying ever increasing popularity in diverse and broad applications. The laser has become an irreplaceable tool in metallurgy, medical technology and electronic industry. In material science, lasers play a significant role either as a passive component for process monitoring or as an active tool by coupling its radiation energy to the material being processed. Lasers, are therefore, extremely useful in a wide variety of applications such as localized melting during optical pulling, laser annealing of semiconductors, surface cleaning by desorption and ablation, laser induced rapid quench to improve surface hardening. Finally, pulsed laser deposition (PLD) has emerged as one of the premier thin film deposition technologies [18].

PLD is the deposition method of choice when one needs to deposit materials with complex stoichiometry. PLD was the first technique successfully used to deposit a superconducting $YBa_2Cu_3O_{7-d}$ thin film. Since then, many materials, especially multielement oxides, normally difficult to be deposited by other methods, have been deposited by PLD. This technique offers many potential applications, from integrated circuits and optoelectronics to micro mechanics and medical implants.

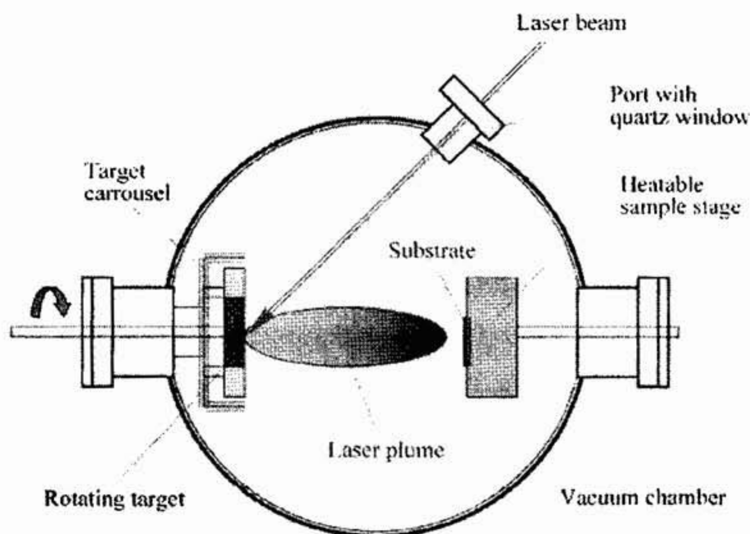

Figure. 2.3. Shematic diagram of PLD chamber

In a typical PLD process, a focused train of high energy laser pulses, derived from a UV nanosecond pulse width laser source, such as the frequency tripled (355 nm) or quadrupled (266 nm) solid state Nd:YAG laser, or the KrF (248 nm) or ArF (193 nm) excimer laser, is rastered over either a metal, a single crystal oxide or a compressed oxide powder target in a vacuum chamber. The high

energy laser pulses interact with the target generating a plume comprised of atomic and molecular species ablated from the target. A substrate, often heated, is placed at a short distance from the target in the direction of the advancing plume (figure 2.3). Though the actual physical process of material removal is quite complex, one can consider the ejection of material to occur from rapid explosion of the target surface by superheating. Unlike thermal evaporation, which produces a vapor composition dependent on the vapor pressures of elements in the target material, the laser induced expulsion produces a plume of material with stoichiometry similar to the target. The best quality films can be deposited by controlling the fundamental criteria such as the substrate temperature, the relative and absolute arrival rates of atoms and the energy of the depositing flux. PLD offers the best control over these criteria than other vacuum deposition techniques.

The main advantages of pulsed laser deposition are:

1) **conceptually simple**: a laser beam vaporizes a target surface, producing a film with the same composition as the target.
2) **versatile**: many materials can be deposited in a wide variety of gases over a broad range of gas pressures.
3) **cost effective**: one laser can serve many vacuum systems.
4) **fast**: high quality samples can be grown reliably in 10 or 15 minutes.
5) **scalable:** as complex oxides move toward volume production.

The mechanism of pulsed laser deposition, in contrast to the simplicity of the setup, is a very complex physical phenomenon. It not only involves the physical

process of the laser-material interaction, but also the formation plasma plume with high energetic species and even the transfer of the ablated material through the plasma plume onto the substrate surface. Thus the thin film formation in PLD generally can be divided into the following four stages.

1) Laser radiation interaction with the target
2) Dynamics of the ablated materials.
3) Deposition of the ablation materials on the substrate.
4) Nucleation and growth of a thin film on the substrate surface

Each stage in PLD is critical to the formation of quality epitaxial, crystalline, stoichiometric and uniform thin films.

In the first stage, the laser beam is focused onto the surface of the target. At sufficiently high flux densities and short pulse duration, all elements in the target are rapidly heated up to their evaporation temperature. Materials are dissociated from the target surface and ablated out with stoichiometry as in the target. The instantaneous ablation rate is highly dependent on the fluences of the laser shining on the target. The ablation mechanisms involve many complex physical phenomena such as collisional, thermal, and electronic excitation, exfoliation and hydrodynamics.

During the second stage, the emitted materials tend to move towards the substrate according to the laws of gas dynamics and show the forward peaking phenomenon. The spatial thickness varies as a function of cosθ. The spot size of the laser and the plasma temperature has significant effects on the deposited film

uniformity. The target-to-substrate distance is another parameter that governs the angular spread of the ablated materials. A mask placed close to the substrate could reduce the spreading. Typical plasma temperature measured by emission spectroscopy during initial expansion of the plume is ≈ 10,000 K, which is well above the boiling point of most materials (≈ 3000 K). Heating of the plasma to these temperatures is thought to occur by inverse Bremsstrahlung absorption of the laser light in a free - free transition of electron ion pair. This high temperature would evaporate the surface layer of the target thereby producing exact composition in the thin films.

The third stage is important to determine the quality of thin film. The ejected high energy species impinge onto the substrate surface and may induce various type of damage to the substrate. These energetic species sputter some of the surface atoms and a collision region is formed between the incident flow and the sputtered atoms. Film grows after a thermalized region is formed. The region serves as a source for condensation of particles. When the condensation rate is higher than the rate of particles supplied by the sputtering, thermal equilibrium condition can be reached quickly and film grows on the substrate surface at the expense of the direct flow of the ablation particles and the thermal equilibrium obtained.

The effect of increasing the energy of the adatoms has a similar effect of increasing substrate temperature on film growth. Typical power densities involved in PLD are approximately 50 $MWcm^{-2}$ for a reasonable growth rate. (> 1 A^{o}/shot) If plasma is formed during laser target interaction in vacuum or in air

then an explicit laser-plasma interaction occurs due to which ions in the plasma are accelerated to as much as 100-1000 eV [19].

Nucleation and growth of crystalline films depends on many factors such as the density, energy, ionization degree, and the type of the condensing material, as well as the temperature and the physico-chemical properties of the substrate. The two main thermodynamic parameters for the growth mechanism are the substrate temperature T and the supersaturation D_m related by the following equation:

$$D_m = kT \ln(R/R_e) \qquad (2.6)$$

where, k is the Boltzmann constant, R is the actual deposition rate, and R_e is the equilibrium value at the temperature T.

The nucleation process depends on the interfacial energies between the three phases present - substrate, the condensing material and the vapour. The critical size of the nucleus depends on the driving force, i.e. the deposition rate and the substrate temperature. For the large nuclei, a characteristic of small supersaturation, they create isolated patches (islands) of the film on the substrate, which subsequently grow and coalesce together. As the supersaturation increases, the critical nucleus shrinks until its height reaches on atomic diameter and its shape is that of a two dimensional layer. For large supersaturation, the layer-by-layer nucleation will happen for incompletely wetted foreign substrates.

The crystalline film growth depends on the surface mobility of the adatom (vapour atoms). Normally, the adatom will diffuse through several atomic

distances before sticking to a stable position within the newly formed film. The surface temperature of the substrate determines the adatom's surface diffusion ability. High temperature favours rapid and defect free crystal growth, whereas low temperature or large supersaturation crystal growth may be overwhelmed by energetic particle impingement, resulting in disordered or even amorphous structures.

The mean thickness, (N_{99}), at which the growing thin and discontinuous film reaches continuity, is given by the formula:

$$N_{99} = A(1/R)^{1/3} \exp(-1/T) \qquad (2.7)$$

where A is a constant related to the materials. In the PLD process, due to the short laser pulse duration (~ 10 ns) and hence the small temporal spread ($\leq$ 10 ms) of the ablated materials, the deposition rate can be enormous (~10 nm/s). Consequently a layer-by-layer nucleation is favoured and ultra-thin and smooth film can be produced. In addition, the rapid deposition of the energetic ablation species helps to raise the substrate surface temperature. In this respect, PLD tends to demand a lower substrate temperature for crystalline film growth.

In the present study, PLD was used to deposit phosphor films at room temperature. The process was carried out in a vacuum chamber pumped by a 6" diffusion pump backed by a rotary pump (Indovision, Bangalore). The laser used was the second (532 nm) harmonic of a Nd:YAG laser (Spectra Physics model GCR 150). The flow of oxygen into the chamber was controlled using a mass flow controller (Bronkhorst, Holland).

2.4. Device fabrication

Alternating current thin film electroluminescent (ACTFEL) devices can be fabricated in vacuum and non-vacuum environments. Practical TFEL devices are expensive as a consequence of using vacuum assisted techniques for film growth. To resolve the problem of cost, new techniques have been explored to eliminate the need for vacuum processes. As oxide phosphors are less moisture sensitive, solution coating techniques [20] and sol-gel synthesis [21] can be used for fabricating devices.

In the present work, rf magnetron sputtering was used to deposit the light emitting layer and the top insulating layer of the fabricated ACTFEL devices. The top electrode was thermally evaporated onto the device to complete the standard metal-insulator-semiconductor-insulator-metal (MISIM) structure. Commercially available nippon electric glass (NEG) substrates coated with indium tin oxide (ITO) and aluminium titanium oxide (ATO) were used for device fabrication. These substrates could withstand a temperature of upto 650°C.

2.5. Characterization tools

Once the films are grown, the structural, compositional, morphological, optical and electrical analytical tools give a better understanding of the film behavior and characteristics. On the reverse, the characterization techniques help in optimizing the growth conditions to get device quality films. In the following

sections, the techniques used for the film characterizations in the present study are discussed briefly.

2.5.1. Thin film thickness

Film thickness has a crucial role in determining its properties unlike a bulk material. The properties of the thin films can be reproduced if thickness, along with other deposition parameters, is kept constant. Film thickness may be measured either by insitu monitoring of the rate of deposition or after the film deposition. The thicknesses of the thin films prepared for the work presented in this thesis were measured by a stylus profiler (Dektak 6M).

The stylus profiler takes measurements electromechanically by moving the sample beneath a diamond tipped stylus. The high precision stage moves the sample according to a user defined scan length, speed and stylus force. The stylus is mechanically coupled to the core of a linear variable differential transformer (LVDT). While in contact over the moving sample surface, surface variations cause the stylus to be translated vertically. Electrical signals corresponding to the stylus movement are produced as the core position of the LVDT changes. The LVDT scales an ac reference signal proportional to the position change, which in turn is conditioned and converted to a digital format through a high precision, integrating, analog-to-digital converter [22].

To measure the film thickness, a region of the substrate has to be masked during film deposition. This creates a step on the sample. The thickness of the sample

can then be measured accurately by measuring the vertical motion of the stylus over the step.

2.5.2. Structural characterization

The crystallographic nature of a sample very well influences its electrical and optical properties. X-ray diffraction (XRD) studies are generally used for structural analysis. Any material has a characteristic diffraction pattern, whether present in pure state or as one constituent of a mixture of substances. This fact is made useful in the diffraction method of chemical analysis. The advantage of the technique is that it discloses the presence of a substance, as that substance actually exists in the sample and not in terms of its constituent chemical elements. Hence, diffraction analysis is useful whenever it is necessary to know the state of chemical combination of the elements involved or the particular phase in which they are present. Compared with ordinary chemical analysis the diffraction method has the advantage that it is usually much faster, requires only very small quantity of sample and is non-destructive.

The basic law involved in the diffraction method of structural analysis is the Bragg's law. When monochromatic beam of x-rays impinge upon the atoms in a crystal lattice, each atom acts as a scattering source. The crystal lattice presents a series of parallel reflecting planes to the incident x-ray beam. The intensity of the reflected beam at certain angles will be maximum when the path difference between two reflected waves from two different crystal planes is an integral multiple of λ. This condition is termed as Bragg's law and is given by,

$$n\lambda = 2d\sin\theta \qquad (2.8)$$

where, n is the order of diffraction, λ is the wavelength of x-rays, d is the spacing between consecutive parallel planes and θ is the glancing angle (or the complement of the angle of incidence) [23].

X-ray diffraction studies give a whole range of information about the crystal structure, orientation, average crystalline size and stress in the powder. Experimentally obtained diffraction patterns of the sample are compared with the standard powder diffraction files published by the International Centre for Diffraction Data (ICDD).

In the present study, the bulk and thin film samples were structurally characterized by recording their XRD patterns using an automated Rigaku x-ray diffractometer. The filtered copper K_α radiation (λ = 1.5414 A^0) was used for recording the diffraction pattern. The average grain size, t, of the film can be calculated using the Scherrer's formula,

$$t = \frac{0.9\lambda}{\beta\cos\theta} \qquad (2.9)$$

Here, β is the full width at half maximum in radians.

The lattice parameter values for a cubic crystallographic system can be calculated from the following equation using the (hkl) parameters and the interplanar spacing d.

Cubic system, $$\frac{1}{d^2} = \frac{h^2 + k^2 + l^2}{a^2} \qquad (2.10)$$

2.5.3. Morphological analysis

Surface morphology is an important property while going for multilayer device fabrication. Roughness of the thin film surface plays a vital role, especially while making interfaces. Some of the characterization tools used to study about the surface of thin films is described below.

2.5.3a. Scanning Electron Microscope (SEM)

The scanning electron microscope (SEM) uses electrons rather than light to form an image. SEM has several advantages over an ordinary light microscope [24]. The SEM has a large depth of field, which allows a large amount of the sample to be in focus at a time. The SEM also produces images of high resolution, which means that closely spaced features can be examined at a high magnification. Preparation of the samples is relatively easy since most SEMs only require that sample should be conductive. The combination of higher magnification, larger depth of focus, greater resolution, and ease of sample observation makes the SEM one of the most heavily used instruments in current research areas.

In a typical SEM, electrons are thermionically emitted from a tungsten or lanthanum hexaboride (LaB_6) cathode and are accelerated towards an anode. Alternatively, electrons can be emitted via field emission. The most common is the Tungsten hairpin gun. Tungsten is used because it has the highest melting

point and lowest vapour pressure of all metals, thereby allowing it to be heated for electron emission.

A voltage is applied to the loop, causing it to heat up. The anode, which is positive with respect to the filament, forms powerful attractive forces for electrons. This causes electrons to accelerate toward the anode. The anode is arranged, as an orifice through which electrons would pass down to the column where the sample is held.

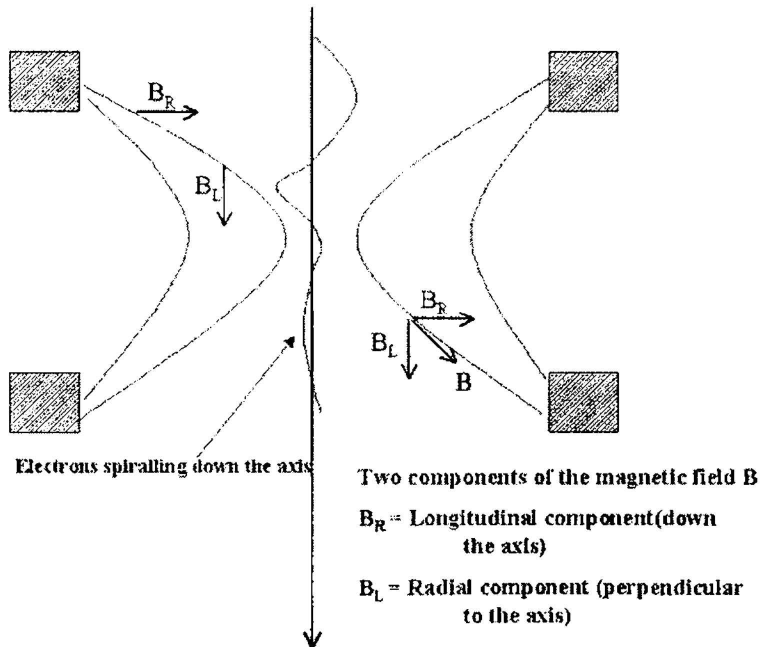

Figure 2.4. The focusing of electrons in SEM

The electron beam, which typically has an energy ranging from a few hundred eV to 100 keV, is attracted through the anode are made to pass through a

condenser lens, and are focused to very fine point on the sample by the objective lens (figure 2.4). The electron beam hits the sample, producing secondary electrons from the sample. These electrons are collected by a secondary detector or a backscatter detector, converted to a voltage, and amplified. The amplified voltage is applied to the grid of the CRT that causes the intensity of the spot of light to change. The image consists of thousands of spots of varying intensity on the face of a CRT that correspond to the topography of the sample.

The spatial resolution of the SEM depends on the size of the electron spot, which inturn depends on the electron energy and the magnetic electron-optical system which produces the scanning beam. To ensure that the information recorded in the image arises only from the sample surface, the column must always be at vacuum. Or else, there are chances for contamination of the sample and the electron beam, instead of being directed onto the sample, would induce ionisation in any background gas that would effect the measurement being made on the sample.

In the present thesis, JEOL JSM 5600 was used for SEM analysis.

2.5.3b. Atomic Force Microscopy (AFM)

The atomic force microscope (AFM) is a very high resolution type of scanning probe microscope, with resolution of fractions of a nanometer, more than 1000 times better than the optical diffraction limit. It can, therefore, probe into understanding the fine details of a sample surface [25].

In atomic force microscopy, a tip integrated to the end of a spring cantilever, is brought within the interatomic separations of a surface, such that the atoms of the tip and the surface are influenced by interatomic potentials. As the tip is rastered across the surface, it bounces up and down with the contours of the surface. By measuring the displacement of the tip (*i.e.* the deflection of the cantilever), one can theoretically map out the surface topography with atomic resolution.

The AFM is essentially identical in concept to the scanning profilometer, except that the deflection sensitivity and resolution are improved by several orders of magnitude. The AFM can operate well in ambient air or in a liquid environment making it an important tool in studying biological systems, polymers and a host of insulator and semiconductor materials.

An AFM images a surface in a manner analogous to the gramophone stylus sensing the groves of gramophone disk. The essential elements of an AFM are shown in the figure 2.5. The tip is attached to a cantilever type spring as shown in the figure 2.6. As the tip and sample interact, forces act on the tip and cause the cantilever (spring) to deflect. The cantilever position is monitored by a position detector. The output of the detector is connected to a feedback controller that regulates the force between the sample and the tip by moving the sample up or down. The sample is moved by a PZT scanning actuator. The cantilever must be soft enough to deflect a measurable amount without damaging the surface features of the sample. The amount of deflection is proportional to the force acting on the tip:

$$F_{spring} = -k \cdot \Delta Z \qquad (2.11)$$

where, F is the force on the sample, k is the spring constant of the cantilever, and, ΔZ is the deflection of the cantilever.

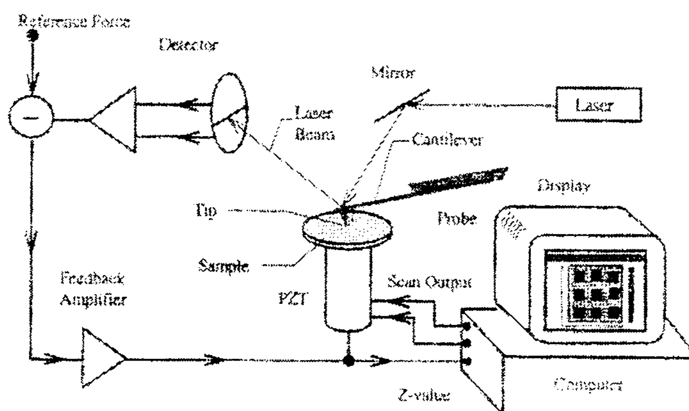

Figure 2.5. The essential elements of an AFM

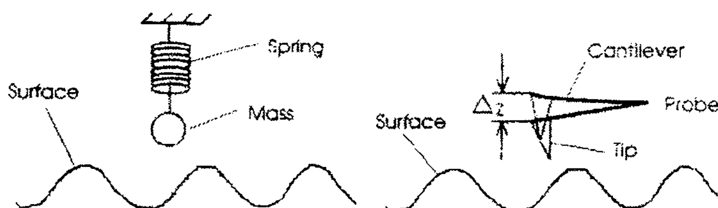

Figure 2.6. Attachment of the tip to the cantilever in an AFM

Two important modes of an AFM are contact mode and the tapping mode. In the contact mode, the static tip deflection is used as the feedback signal. In the tapping mode, the cantilever is externally oscillated at or close to its resonance

frequency. The oscillation amplitude, phase and resonance frequency are modified by tip-sample interaction forces; these changes in oscillation with respect to the external reference oscillation provide information about the sample's characteristics.

The AFM provides us with a true three dimensional surface profile compared to the two dimensional SEM image, with atomic resolution in ultra high vacuum environments. But an AFM can only image a maximum height of the order of micrometres and a maximum scanning area of around 150 by 150 micrometres whereas SEM can image an area on the order of millimetres by millimetres with a depth of field of the order of millimetres.

In the present work, AFM from Veeco was used for the morphological study.

2.5.4. Compositional analysis

Compositional analysis helps to check the stoichiometry of the deposited films. Some of the characterization tools used in the present investigation is described below.

2.5.4a. Energy dispersive x-ray (EDX) analysis

Energy dispersive x-ray (EDX) analysis is used for determining the elemental composition of a specimen. It often works as an integrated feature of a SEM, and cannot operate on its own without the latter. During EDX Analysis, the

specimen is bombarded with an electron beam inside the scanning electron microscope. The bombarding electrons (primary electrons) collide with the specimen, knocking some of them off in the process. The vacancy in the specimen atoms created by the ejection of an inner shell electron is eventually occupied by a higher energy electron from an outer shell. During this transition, the transferring electron gives up its excess energy in the form of x-rays.

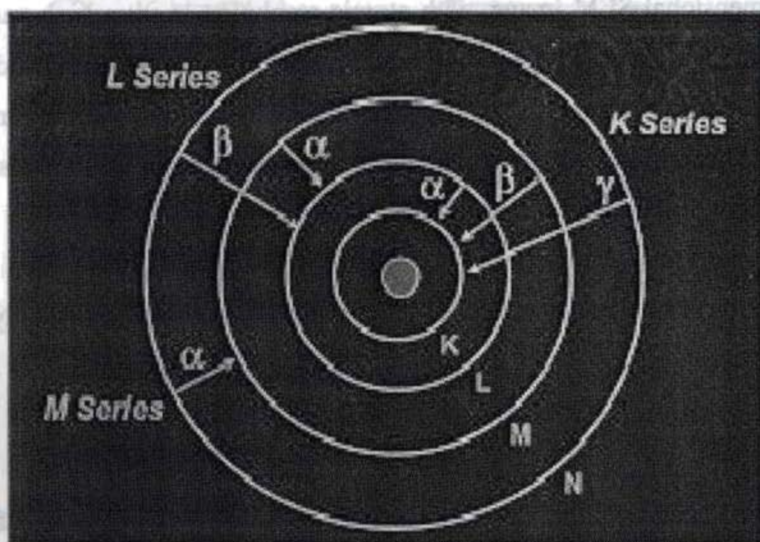

Figure 2.7. Electronic transitions giving rise to x-ray emission

The amount of energy released by the transferring electron depends on which shell it is transferring from, as well as which shell it is transferring to. Furthermore, the atom of every element releases x-rays, unique in energy during the transferring process, characteristic of that element. Thus, by measuring the energy of the x-rays emitted by a specimen during electron beam bombardment, the identity of the atom from which the x-ray was emitted can be established.

The output of an EDX analysis is an EDX spectrum, which is a plot of how frequently an x-ray is received for each energy level. An EDX spectrum normally displays peaks corresponding to the energy levels for which the most x-rays had been received. Each of these peaks is unique to an atom, and therefore corresponds to a single element. The higher a peak in a spectrum, the more concentrated the element is in the specimen. An EDX plot not only identifies the element corresponding to each of its peaks, but the type of x-ray to which it corresponds as well. For example, a peak corresponding to the amount of energy possessed by x-rays emitted by an electron in the L-shell going down to the K-shell is identified as a K_α peak. The peak corresponding to x-rays emitted by M-shell electrons going to the K-shell is identified as a K_β peak as shown in figure 2.7.

2.5.4b. X-ray fluorescence (XRF) analysis

X-ray fluorescence (XRF) is another technique used for elemental analysis. Here, a material emits characteristic "secondary" (or fluorescent) x-rays when excited by high energy x-rays or gamma rays. When materials are exposed to short wavelength x-rays or to gamma rays with energy greater than its ionization potential, ionization of their component atoms may take place. X-rays and gamma rays can be energetic enough to expel even the tightly held electrons from the inner orbitals of the atom. Such a removal of an electron renders the electronic structure of the atom unstable, and electrons in higher orbitals fall into the lower orbital to fill the hole left behind. During this transition, energy is released in the form of a photon, the energy of which is equal to the energy

difference of the two orbitals involved. Thus, the material emits radiation, which has energy characteristic of the atoms present. The intensity of each characteristic radiation is directly related to the amount of the corresponding element in the material. The term fluorescence is applied to the phenomena since absorption of higher energy radiation results in the re-emission of lower energy radiation.

Rigaku x-ray fluorimeter was used in the present study.

2.5.5. Optical studies

2.5.5a. Determination of band gap energy

In the present study, diffuse reflectance spectroscopy and transmission spectroscopy was used to determine the band gap of powder and thin film samples respectively.

i) Diffuse reflectance spectroscopy (DRS)

Diffuse reflection is the reflection of light from an uneven or granular surface such that an incident ray is seemingly reflected at a number of angles. Diffuse reflected rays from a sample do not obey the Snell's law as do the ordinary mirror-like specular reflections. The measurement of radiation diffusely reflected from a surface constitutes the area of spectroscopy known as diffuse reflectance spectroscopy (DRS). Specular reflection is due to the reflection at the

surface of single crystallites while diffuse reflection arises from the radiation penetrating into the interior of the solid and re-emerging to the surface after being scattered numerous times. Thus, the DRS spectra can exhibit both absorbance and reflectance features due to contributions from transmission, internal and specular reflectance components as well as scattering phenomena in the collected radiation.

Based on the optical properties of the sample, several models have been proposed to describe the diffuse reflectance phenomena. The Kubelka-Munk (KM) model put forward in 1931 [26, 27] is widely used and accepted in DRS. The KM theory is based on a continuum model where reflectance properties are described by differential equations for infinitesimally small layers. When the depth of the sample is infinite, the theory is solved to arrive at the remission function or the so-called KM function,

$$f(r_\infty) = \frac{(1 - r_\infty)^2}{2r_\infty} = \frac{k}{s} \qquad (2.12)$$

where, $r_\propto$ = $R_\propto$(sample)/$R_\propto$(standard), $R_\propto$ denotes the diffuse reflectance. Here the standard used is $BaSO_4$. $R_\propto$(standard) is taken as unity. The intensity of the diffusely reflected light therefore depends on the scattering coefficient s and the absorption coefficient k. The band gap is estimated from the plot of $\{(k/s).h\nu\}^2$ versus hν (hν is the photon energy) by extrapolating the graph to the x axis.

DRS was carried out using Jasco V 500 spectrophotometer in the present studies.

ii) Transmission spectroscopy

Intrinsic optical absorption of a single photon across the band gap is the dominant optical absorption process in a semiconductor. When the energy of the incident photon (hν) is larger than the band gap energy the excitation of electrons from the valence band to the empty states of the conduction band occurs. The light passing through the material is then absorbed and the number of electron hole pairs generated depends on the number of incident photons $S_0(\nu)$ (per unit area, unit time and unit energy). The photon flux $S(x,\nu)$ decreases exponentially inside the crystal according to the relation,

$$S(x, \nu) = S_0(\nu) \exp(-\alpha x) \qquad (2.13)$$

where, the absorption coefficient α, ($\alpha(\nu) = 4\pi k\nu/c$) is determined by the absorption process in semiconductors and k is the extinction coefficient.

For the parabolic band structure, the relation between the absorption coefficient (α) and the band gap of the material is given by [28],

$$\alpha = \frac{A}{h\nu}(h\nu - E_g)^r \qquad (2.14)$$

where, r = 1/2 for allowed direct transitions, r = 2 for allowed indirect transitions, r = 3 for forbidden indirect transitions and r = 3/2 for forbidden direct transitions. A is the parameter which depends on the transition probability. The absorption coefficient can be deduced from the absorption or transmission spectra using the relation,

$$I = I_0 e^{-\alpha t} \qquad (2.15)$$

where, I is the transmitted intensity and I_0 is the incident intensity of the light and t is the thickness of the film. In the case of direct transition, $(\alpha h\nu)^2$ will show a linear dependence on the photon energy ($h\nu$). A plot of $(\alpha h\nu)^2$ against $h\nu$ will be a straight line and the intercept on energy axis at $(\alpha h\nu)^2$ equal to zero will give the band gap energy.

The transmissions of the thin films were recorded using Jasco V570 spectrophotometer in the present studies.

2.5.5b. Photoluminescence (PL)

Photoluminescence spectroscopy is a contactless, non-destructive method of probing the electronic structure of materials [29]. Photoluminescence (PL) is the emission of light when a substance is irradiated with a shorter wavelength light. Quantum mechanically, photo-excitation causes electrons within the material to move into permissible excited states. When these electrons return to their equilibrium states, the excess energy is released radiatively or nonradiatively. The radiative emission on photo-excitation is what one refers to as photoluminescence.

The energy of the emitted light relates to the difference in energy levels between the two electron states involved in the transition between the excited state and the equilibrium state. The quantity of the emitted light is related to the relative contribution of the radiative process. The intensity and spectral content of the luminous output is a direct measure of various important material properties.

Radiative transitions in semiconductors also involve localized defect levels. The photoluminescence energy associated with these levels can be used to identify specific defects, and the amount of photoluminescence can be used to determine their concentration.

Two types of luminescence spectra can be distinguished: excitation and emission. The excitation spectrum gives the intensity variations of the exciting radiation over a range for a fixed emission wavelength. It gives information on the position of excited states just as the absorption spectrum does, except that the former reveals only the absorption bands that result in the emission of light. The observed differences between the absorption and excitation spectra can yield useful information. An emission spectrum provides information on the spectral distribution of the light emitted by a sample for a given excitation wavelength. The time resolved PL measurements are a powerful tool for the determination of the radiative efficiency that specifies the fraction of excited states which de-excite by emitting photons.

The emission and excitation spectra for the powder and thin film samples are recorded using Fluorolog - 3 spectroflurometer consisting of 150W Xenon arc lamp, monochromator and a CCD detector. A continuous source of light shines on to an excitation monochromator, which selects a band of wavelengths. This monochromatic excitation light is directed onto a sample, which emits luminescence. The luminescence is directed into a second emission monochromator which selects a band of wavelengths and shines them onto a photon counting detector (R928P PMT) ranging from 180-850 nm. The

reference detector monitoring the xenon lamp - a UV enhanced Si photodiode - requires no external bias and has good response from 190-980 nm The signal from the detector is reported to a system controller and host computer where the data can be manipulated and presented using special software.

2.5.5c. Color characterization

Color characterization of a spectral distribution is done to gauge the quality of its chromaticity. This is accomplished using color coordinates [30].

In 1931, the Commission Internationale de l'Eclairage (CIE) established an international standard for quantifying color known as CIE color coordinates. The chromaticity coordinates map all the visible colors with respect to hue and saturation on a two dimensional chromaticity diagram. The CIE coordinates are obtained from the three CIE tristimulus values, X, Y and Z. These tristimulus values are computed by integrating the product of the spectrum of the light source, $P(\lambda)$, and standard observer functions called the CIE color matching functions, $x_\lambda(\lambda)$, $y_\lambda(\lambda)$ and $z_\lambda(\lambda)$ (shown in figure 2.8) over the entire visible spectrum using the relations,

$$X = \sum_{\lambda=380nm}^{780} x_\lambda(\lambda) P(\lambda) \Delta\lambda \qquad (2.16)$$

$$Y = \sum_{\lambda=380nm}^{780} y_\lambda(\lambda) P(\lambda) \Delta\lambda \qquad (2.17)$$

$$Z = \sum_{\lambda=380nm}^{780} z_{\lambda}(\lambda)P(\lambda)\Delta\lambda \tag{2.18}$$

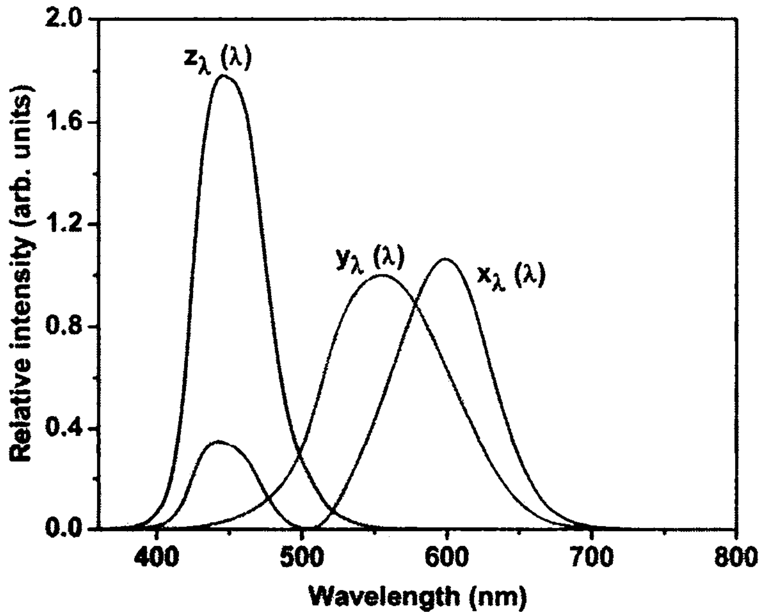

Figure 2.8. Plot of the CIE tristimulus (x, y, and z) functions

Once X, Y and Z are known, the CIE color coordinates are calculated using the relations,

$$x = \frac{X}{X+Y+Z}, y = \frac{Y}{X+Y+Z}, z = \frac{Z}{X+Y+Z} \tag{2.19}$$

Being constrained by the relation (x + y + z) = 1, any two of the three CIE color coordinates are independent.

Plotting of the CIE x versus CIE y color coordinate over the visual range of light leads to a horseshoe shaped diagram known as the CIE chromaticity diagram shown in figure 2.9.

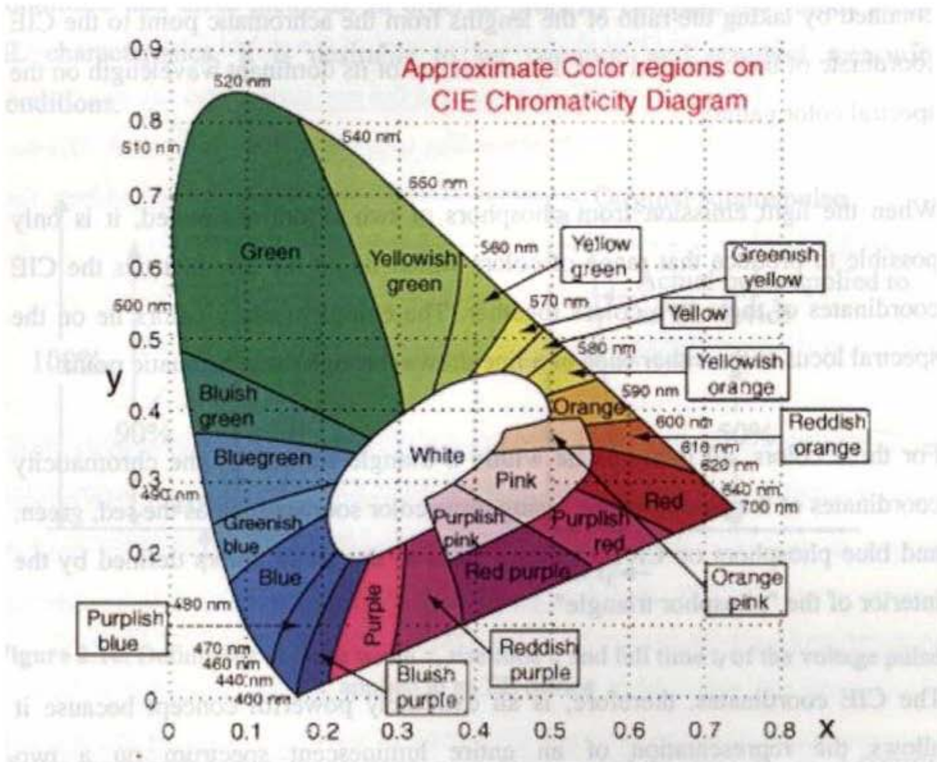

Figure 2.9. The CIE chromaticity diagram

The monochromatic spectral colors lie along the horse shoe shaped path called the spectral locus. All visible colors lie within the shape bounded by this path. The straight line from violet (400 nm) to red (700 nm) is called the purple line and cannot be produced by light of a single wavelength. The CIE coordinates for achromatic white is (x,y) = (0.33,0.33).

When the CIE coordinates of a color are specified, the dominant wavelength of the color is the intersection of the line connecting these CIE coordinates and those of white light with the upper arc of the diagram. The color purity is obtained by taking the ratio of the lengths from the achromatic point to the CIE coordinate of the color and the CIE coordinate of its dominant wavelength on the spectral color gamut.

When the light emission from phosphors of two colors are mixed, it is only possible to produce that range of colors which lie on the line that ties the CIE coordinates of these two colors together. The complementary colors lie on the spectral locus at the either ends of a line drawn through the achromatic point.

For three colors, all mixtures lie within a triangle formed by the chromaticity coordinates of the parent colors. Using three color sources such as the red, green, and blue phosphors on CRT monitors leads to the set of colors defined by the interior of the "phosphor triangle".

The CIE coordinates, therefore, is an extremely powerful concept because it allows the representation of an entire luminescent spectrum on a two dimensional plane.

The main drawback to the CIE coordinate system is the complexity involved in their calculation. Moreover, the CIE color space is a perceptionally nonuniform color space, i.e. equal distances at two different regions of the chromaticity diagram are not proportional to perceptual differences in observed hue.

2.5.6. Device characterization

Electroluminescent device characteristics depend strongly on the measuring conditions and drive methods. In order to properly compare the values for the EL characteristics, it is desirable to set common and standard measuring conditions.

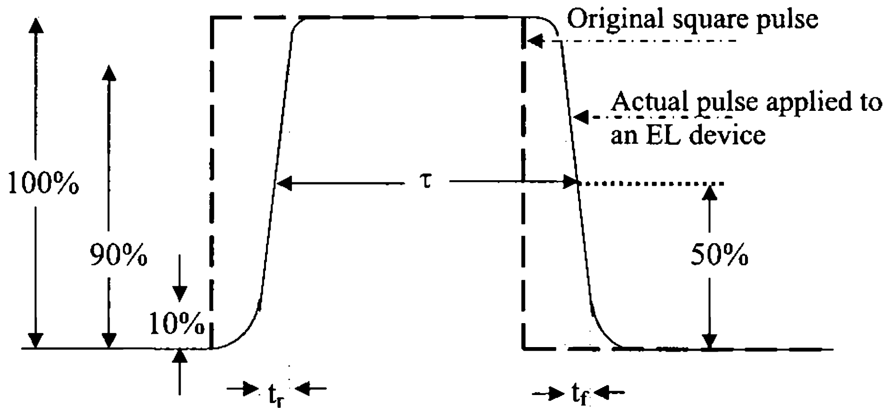

Figure 2.10. Definitions of pulse width τ, rise time t_r and fall time t_f of the voltage pulse applied to an EL device

The recommended driving voltage waveforms used to operate an ACTFEL device are sine waves, triangular waves or bipolar trapezoidal waves of alternate polarity and frequency 60 Hz or 1 KHz. The standard bipolar voltage waveform used for most of the electrical characterization techniques consists of a 1 KHz sequence of bipolar trapezoidal pulses with rise and fall times of 5 μs and a pulse width of 30 μs. In case a square wave pulse of alternate polarity is used, the following parameters should be specified as defined in figure 2.10.

It is to be noted that the polarity of the applied voltage pulse is defined with respect to the top electrode (i.e. the electrode farthest away the substrate). The voltage values should be indicated in zero-to-peak values, rather than in rms values, since luminance depends on the peak voltage value. The pulse width, τ, is defined by the full width at the half maximum of the actual (deformed) pulse drive waveform applied to an EL device, and the rise time t_r and the fall time t_f are defined by the time period corresponding to 10%-to-90% value and 90%-to-10% value, respectively, of the actual voltage. The recommended values for practical applications are $\tau = 40$ µs, $t_r \leq 8$ µs and $t_f \leq 8$ µs.

2.5.6.1. Luminance-Voltage (L-V) Characterization

The techniques frequently used to compare and contrast ACTFEL devices from an industrial viewpoint are measurements that explore its light output, the power required to generate that light and the color of light emitted. The optical response of an ACTFEL device to an electrical stimulus is critical in specifying the display performance.

The experimental setup used in the present study for luminance measurement is given in figure 2.11. The method requires a variable ac voltage supply (typically 0-300 V). A photometer, photomultiplier tube (PMT), CCD or a photodiode is usually used to measure the luminance as a function of the applied voltage. Here, we apply waveforms of steadily increasing amplitude to the ACTFEL device and measure the luminance at every step. Once the data is collected, plotting voltages on the x-axis and the corresponding luminances on the y-axis gives the

L-V curve. An L-V plot gives the luminous intensity output in a direction normal to the emitting surface, and is generally reported in either foot Lamberts (ft-L) or candelas per square meter (cd/m^2) [1ft-L = 3.426 cd/m^2].

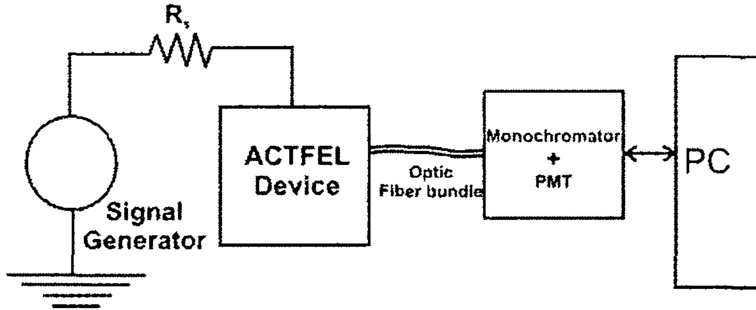

Figure 2.11. Experimental setup for luminance measurement

Several important ACTFEL parameters, namely, the threshold voltage (V_{th}) and luminance at V_{th}, + 40 V (L_{40}) can be determined from luminance versus voltage (L-V) measurements. A typical L-V plot is shown in figure 2.12.

The threshold voltage is typically defined to be the voltage where a luminance of 1 cd/m^2 is achieved. At this external voltage, the field inside the phosphor is high enough to cause electrons to excite the luminescent centers and generate light. As the voltage increases above threshold, the phosphor electric field increases proportionally, as does the electron energy distribution. Consequently, luminance sharply increases with voltage until the phosphor brightness saturates or until the phosphor layer experiences dielectric breakdown.

The significance of the parameter L_{40} is that most ACTFEL displays are driven at 40 V above threshold, which is the modulation voltage. When comparing L_{40}

values, it is important to consider both the threshold voltage and the frequency at which the device was driven. L_{40} increases almost linearly with both phosphor thickness (i.e. V_{th}) and frequency. As thickness increases, there are more luminescent centers that electrons can excite; and when frequency increases, the number of passes that electrons make across the phosphor layer increases.

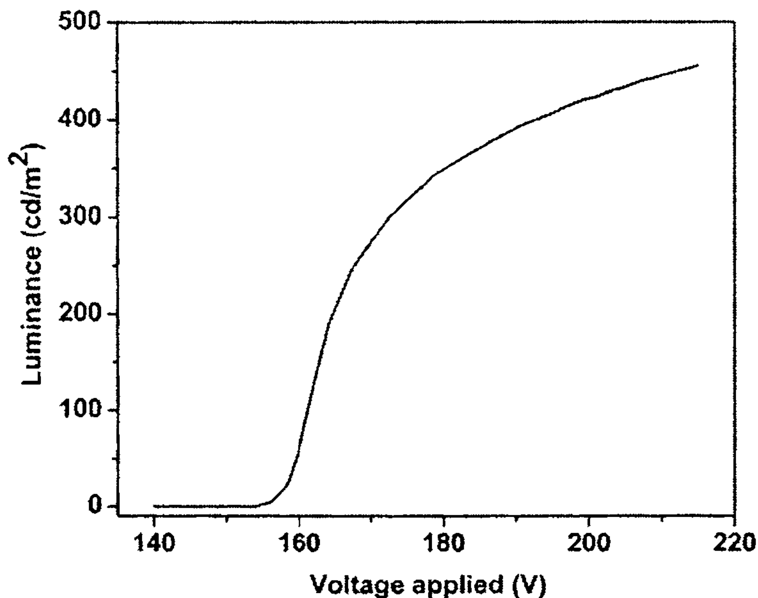

Figure 2.12. A typical luminance-voltage (L-V) curve

The L-V measurement is very sensitive to the nature of the driving waveform, driving voltage and its frequency. The measured luminance depends to some degree on the rise time, fall time and pulse width when bipolar trapezoidal waveforms are used to generate L-V data. The measured luminance at a fixed voltage increases quite noticeably with increasing frequency. This is because at higher frequencies, more pulses are applied to the ACTFEL device per unit time;

hence, the luminescent impurities are excited more often. Unfortunately, there is a point of diminishing returns with increasing frequency where the luminance either saturates or decreases at a certain frequency. This effect has to do with both device heating and the de-excitation time of the luminescent impurities. Additionally, when the period of the driving waveform is of the same order as the characteristic decay time of the luminescent impurity, there may be little or no increase in luminance with increasing frequency because many luminescent impurities may already be excited when the following pulse arrives. Essentially, the fraction of time per second that the driving waveform spends above the turn-on voltage determines the relative luminance of the device.

Besides the chemical composition, the thickness of the phosphor layer affects the observed luminance of the ACTFEL device. As the phosphor layer grows thicker (for a fixed doping concentration), more luminescent impurities get incorporated, and the carriers have a greater probability of impact excitation. Therefore, with all else being equal, ACTFEL devices with thicker phosphor layers will exhibit greater luminance than thinner devices.

The insulators affect the luminance characteristics of an ACTFEL device mainly through their effect on the voltage distribution through the device. An increase of insulator capacitance with respect to a fixed phosphor capacitance results in a greater percentage of the applied voltage being dropped across the phosphor layer, which leads to a lower threshold voltage. The two methods of increasing the insulator capacitance are to either decrease the thickness of the insulator layers or use an insulating material with larger dielectric constant.

The doping level of the luminescent impurity also is critical in determining the L-V characteristics of an ACTFEL device. At low dopant concentrations ($\leq$ 1% for most phosphor materials), the observed luminance increases monotonically with increasing luminescent impurity concentration. Then, an optimum luminance is achieved, and the luminance declines with increasing luminescent impurity concentration above this doping level. This decline is due to the disruption of phosphor crystallinity and the increased number of nonradiative transition paths that result from high luminescent impurity doping levels. Furthermore, at higher luminescent impurity doping levels, hysteresis in the L-V characteristics is sometimes observed.

In the present work, the fabricated devices were electrically excited using a 1.5 KHz trapezoidal waveform generated from a pulsed signal generator (Digilog Instruments Ltd.). The bipolar pulse train driving the device had a characteristic rise and fall time of 30 μs each and a stay time of 70 μs. A 0.32 m monochromator (Triax-320) coupled with Hamamatsu R928 photomultiplier tube was used to record the electroluminescent emission from the fabricated device.

References

1. J. George, *Preparation of Thin Films*, p.1, Marcel Dekker Inc., New York (1992).
2. T. Sei , Y. Nomura and T. Tsuchiya, *J. Non-Cryst. Solids*, **218**, 135 (1997).

3. Z. Ji, L. Kun, S. Yongliang and Y. Zhizhen, *J. Cryst. Growth*, **255**, 353 (2003).
4. Z. Yan, M. Koike and H. Takei, *J. Cryst. Growth*, **165**, 183 (1996).
5. S. H. Yang, *J. Electrochem. Soc.*, **150**, H250 (2003).
6. Z. Lou and J. Hao, *Appl. Phys. A*, **80**, 151 (2005).
7. J. Hao, Z. Lou, I. Renaud and M. Cocivera, *Thin Solid Films*, **467**, 182 (2004).
8. T. Miyata, T. Nakatani and T. Minami, *Thin Solid Films*, **373**, 145 (2000).
9. N. Honda, T. Suzuki, T. Yunogami, H. Suematsu, W. Jiang and K. Yatsui, *Jpn. J. Appl. Phys.*, **44**, 695 (2005).
10. T. Minami, Y. Kuroi, S. Dakata, *J. Vac. Sci. Technol. A*, **14**, 1736 (1996).
11. L. I. Maissel and R. Glang, *Handbook of Thin Film Technology*, p.22, McGraw-Hill, New York (1970).
12. L. Holland, *Vacuum Deposition of Thin films*, p.104, John Wiley & Sons Inc., New York (1956).
13. D. L. Smith, *Thin-film deposition*, p.431, Mc Graw - Hill, New York (1995).
14. F. L.Akkad, A. Punnose and J. Prabu, *J. Appl. Phys.*, **71**, 157 (2000).
15. M. Ohring, *Materials Science of Thin Films*, Second edition, p.161, Academic Press, San Diego (2002).
16. B. Chapman, Glow Discharge Processes, p.108, John Wiley & Sons Inc., New York (1980).
17. V. S. Smentkowski, *Prog. Surf. Sci.*, **64**, 1 (2000).
18. T. Venkatesan and S. M. Green, *The industrial physicist*, **2**, 22 (1996).
19. D. B. Chrisey and G. K. Hubler, *Pulsed Laser Deposition of Thin Films*, p.229, John Wiley and sons Inc., New York (1994).

20. T. Minami, T. Nakatani and T. Miyata, *J. Vac. Sci. Technol. A*, **18**, 1234 (2000).
21. T. Minami, T. Shirai, T. Nakatani and T. Miyata, *Jpn. J. Appl. Phys.*, **39**, L524 (2000).
22. Veeco Dektak 6M Manual 2004.
23. B. D. Cullity and S. R. Stock, *Elements of X ray diffraction*, Third edition, p.170, Prentice Hall, New Jersey (2001).
24. D. K. Schroder, *Semiconductor material and device characterization*, Second edition, p.651, John Wiley & Sons Inc., New York (1998).
25. P. E .J. Flewit and R. K. Wild, *Physical methods for material characterization*, Second edition, p.501, IOP publishing, London (2003).
26. P. Kubelka and F. Munk, *Zh. Tekh. Fiz.*, **12**, 593 (1931).
27. P. Kubelka, *J. Opt. Soc .Am.*, **38**, 448 (1948).
28. A. Goswami, *Thin Film Fundamentals*, p.418, New Age International (P) Limited, New Delhi (1996).
29. D. R. Vij (Ed.), *Luminescence of solids*, p.46, Plenum Press, New York (1998).
30. G. Wyszecki and W. S. Stiles, *Color Science: concepts and methods, quantitative data and formulae*, Second edition, p.131, John Wiley & Sons Inc., New York (1982).

Chapter 3

Growth of $ZnGa_2O_4$ phosphor thin films by pulsed laser ablation

3.1. Introduction

Spinel $ZnGa_2O_4$ is an attractive oxide phosphor for both cathodo- and electroluminescent applications [1, 2]. The excellent chemical stability of the oxides, relative to the more commonly used sulphides, has triggered immense research to promote their incorporation in future display systems. Moreover, thin film phosphor materials are widely investigated for use in display applications as they offer such advantages as high contrast ratio, high ambient visibility, high image resolution and good heat resistance.

The melting point of $ZnGa_2O_4$ is in excess of 1400°C [3]. Such high crystallization temperature restricts the use of glass substrates, which possess low softening temperature, for thin film electroluminescent (TFEL) applications. The current work, therefore, checks the possibility of $ZnGa_2O_4$ thin film growth at room temperature on amorphous glass and fused silica substrates.

The fabrication of complex oxide hosts is rather difficult due to their high melting point and unexpected compositional deviation [4]. Pulsed laser deposition (PLD) has been widely accepted for depositing oxide films as it helps to preserve the stoichiometry during film growth. The energy of the adatoms being of the order of 100 - 1000 eV [5], PLD technique would be an ideal choice for attempts to grow crystalline films at low temperatures. Several groups have explored this technique to deposit epitaxial $ZnGa_2O_4$ thin films on single crystalline substrates [6-11]. However, these works were carried out at substrate temperatures at and above 300°C. Lee *et al.* [12] has even reported that films

deposited below 400°C were amorphous regardless of the substrate used. The deposition on glass substrates yielded only randomly oriented polycrystalline films with poor crystallinity irrespective of processing conditions [8].

3.2. Experimental

A stoichiometric target of $ZnGa_2O_4$ was synthesized in the laboratory by high temperature solid state reaction of the constituent binary oxides, namely, ZnO (99.99%, Alfa Aesar) and Ga_2O_3 (99.99%, Alfa Aesar). Adequate amounts of the starting materials were weighed to an accuracy of ± 0.001 mg, hand mixed thoroughly in ethanol medium using an agate mortar and pestle and allowed to dry in an oven. The dried mixture was then pressed into an 8 mm thick disk of diameter 25 mm, placed in an alumina boat and introduced into the hot temperature zone of a horizontal tube furnace equipped with a proportional integral differential (PID) controller. The sintering was performed at 1350°C for 36 hrs in air. The x-ray diffraction pattern of the synthesized target is shown in figure 3.1. All the diffraction peaks were identified as those of spinel $ZnGa_2O_4$ [13]. There was no indication of contamination by crystalline phases of constituent oxides.

Thin films were grown by laser ablating the $ZnGa_2O_4$ target using an electro-optically Q-switched frequency doubled Nd:YAG laser (Spectra Physics INC, GCR 150). The second harmonic output at 532 nm (300 mJ) was focused onto the target, placed at 45° with respect to the laser beam, using a spherical convex lens to obtain a spot size of diameter 2 mm. The laser pulse width was 6-7 ns

with a repetition frequency of 10 Hz. The target was rotated continuously during deposition at the rate 23 rpm to ensure uniform pitting of the target surface by the laser beam. The substrate to target (S-T) distance, duration of deposition and laser power was optimized so as to obtain crystalline $ZnGa_2O_4$ thin films. The films were deposited at room temperature (300 K) varying the oxygen pressure from 0.01 mbar to 0.001 mbar using a mass flow controller (50 sccm, Bronkhorst). Fused silica and glass were used as substrates.

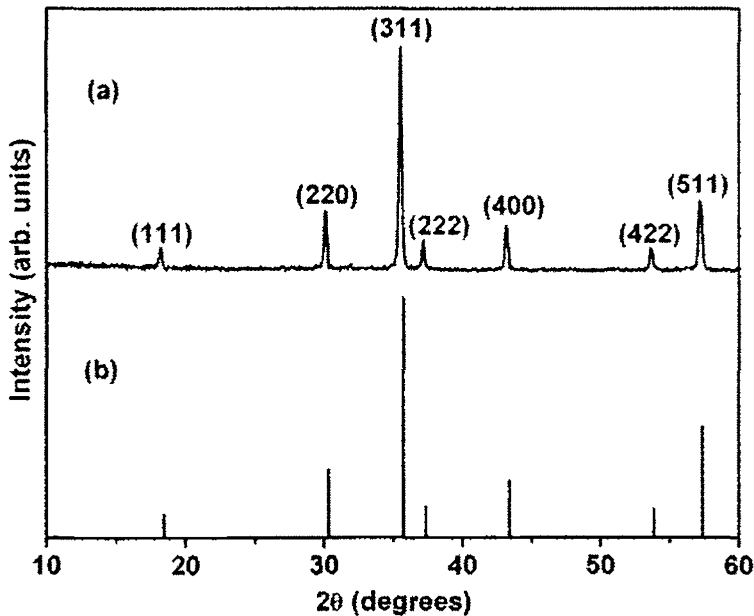

Figure 3.1. (a) XRD pattern of the $ZnGa_2O_4$ target synthesized at 1350^0C for 36 hrs in air (b) JCPDS data of $ZnGa_2O_4$ is shown for reference

The films were structurally characterized using an x-ray diffractometer (Rigaku) with Cu-K_α radiation (1.5414 Å). The surface morphology and cation

composition ratio (Zn/Ga) of the thin films were evaluated by scanning electron microscopy (SEM) and energy dispersive x-ray (EDX) analysis respectively. The thickness of the samples was measured using Dektak 6M stylus profiler. The transmission spectra of the films were recorded using UV-VIS-NIR spectrophotometer (Hitachi U 3410). The diffuse reflectance spectra (DRS) of bulk $ZnGa_2O_4$ was measured using JASCO V-570 spectrophotometer. $BaSO_4$ was used as the reference for DRS analysis. The photoluminescent (PL) emission and excitation spectra (PLE) were recorded using Jobin Yvon Fluoromax-3 spectrometer equipped with a 150 W xenon lamp.

3.3. Room temperature deposition of crystalline $ZnGa_2O_4$ thin films

The deposition parameters such as laser power density, deposition time and S-T distance were initially optimized at 0.8 J/cm^2/pulse, 2 hrs and 9 cm respectively to ensure the growth of well adhesive and transparent $ZnGa_2O_4$ phosphor thin films. The growth rate was found to be too low at lower laser powers and higher S-T distances. At higher laser energies, the films gave a brownish appearance adversely affecting the material transparency. At lower S-T distances, the films obtained were too powdery and nonadhesive. The average growth rate of the films deposited under the optimized conditions was 0.04 nm/s.

The oxygen pressure inside the deposition chamber also had a pronounced effect on the crystalline nature of the PLD grown films. A background oxygen pressure was essential to interact with and compensate the excess of Zn in the ablated

plume. Hence, the oxygen pressure was varied from 0.001 mbar to 0.01 mbar and the effect was studied at room temperature.

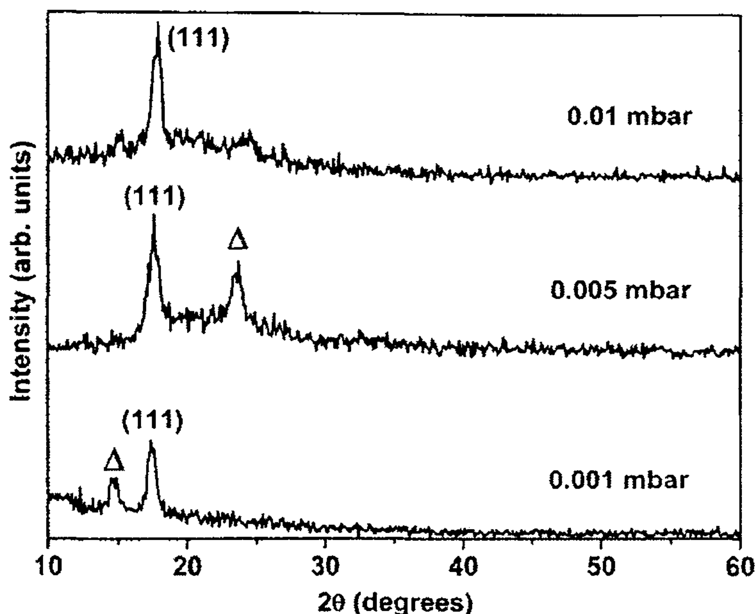

Figure 3.2. X-ray diffraction patterns of as-deposited $ZnGa_2O_4$ films on quartz substrates at various oxygen pressures, Δ – Ga_2O_3 peak

The x-ray diffraction patterns of as-deposited $ZnGa_2O_4$ films on fused silica substrates for various oxygen pressures is shown in figure 3.2. All the films oriented along the (111) plane of spinel $ZnGa_2O_4$ irrespective of oxygen pressure. In spinels, (111) is the most frequently observed twin and cleavage plane with minimum surface energy [14]. The films deposited at 0.001 mbar and 0.005 mbar exhibits the secondary phase of Ga_2O_3 [15, 16] in addition to the (111) peak of $ZnGa_2O_4$. Single phased spinel growth is exhibited by the film

grown at the oxygen pressure of 0.01 mbar. The stress induced in the films during deposition caused a shift in the (111) peak position to higher angles by an amount $\Delta\theta = 0.45^\circ$ as the oxygen pressure is increased from 0.001 to 0.01 mbar. Full width at half maximum (FWHM) of the as-deposited films was found to increase with oxygen pressure. The film deposited at 0.001 mbar exhibited the least FWHM value of 0.59°. The growth of crystalline films depend on the energy of the adatoms, for the adatoms reaching the substrate need to migrate on the substrate surface efficiently for proper orientation to assist film growth with lower energy configuration. As the pressure of the background gas inside the chamber is increased, the kinetic energy of the adatoms reaching the substrate decreases. This leads to less efficient migration of the adatoms over the substrate resulting in inferior crystalline films.

The EDX studies (figure 3.3.d) show that Zn/Ga ratio of the as-deposited films increased with oxygen pressure. That is, the increase in oxygen pressure has significantly reduced the loss of Zn in the films. Ablated species consist of Zn, Ga, Zn-O, Ga-O, and perhaps Zn-Ga-O molecules. Introduction of additional oxygen shall produce more Zn-O molecules through gas phase collisions of Zn species with oxygen. Increased oxygen partial pressure, therefore, lessens the probability of desorption of Zn species from the heated substrates and results in the incorporation of more Zn in the films [8].

A large deviation in the Zn/Ga ratio, from the expected value of 0.5, is attributed to the use of a stoichiometric target in the present study. Moreover, the vapor pressure of Zn is higher than that of Ga. Lee *et al.* [8, 12] suggests that the use

of mosaic $ZnGa_2O_4/ZnO$ ablation targets can compensate for the loss of Zn via evaporation. However, the film deposited at 0.01 mbar, that exhibited a single phase growth, possessed a cation composition ratio of 0.43.

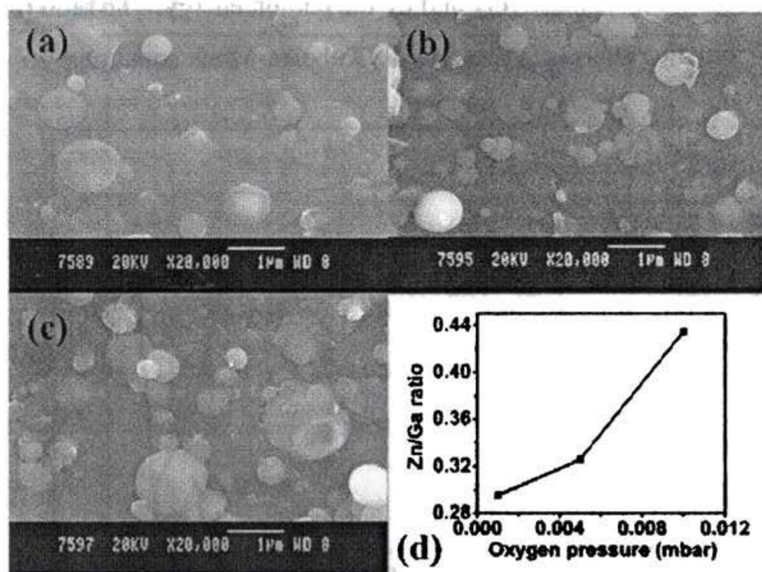

Figure 3.3. SEM images of as-deposited $ZnGa_2O_4$ films at oxygen pressures a) 0.001 mbar, b) 0.005 mbar and c) 0.01 mbar. (d) shows the variation of Zn/Ga ratio with increase in oxygen pressure

The SEM images of the laser ablated $ZnGa_2O_4$ films are also shown in figure 3.3 for various oxygen pressures. Numerous disk shaped particles are observed on the smooth surface of the film. These particles result from the ejection of the molten material from the target to the substrate at such high laser fluences [6].

The DRS of bulk $ZnGa_2O_4$ is as shown in figure 3.4. The band gap is obtained by converting the reflectance data to absorbance mode employing the Kubelka-

Munk (K-M) theory [17, 18]. The band gap was estimated to be 4.59 eV from the $\{(k/s).h\nu\}^2$ versus hν plot (inset of figure 3.4.), extrapolating the linear portion of the curve to hν = 0. Here, k and s denotes the absorption and scattering coefficients respectively and hν the photon energy. The ratio (k/s) was calculated from the reflectance data via the Kubelka-Munk equation.

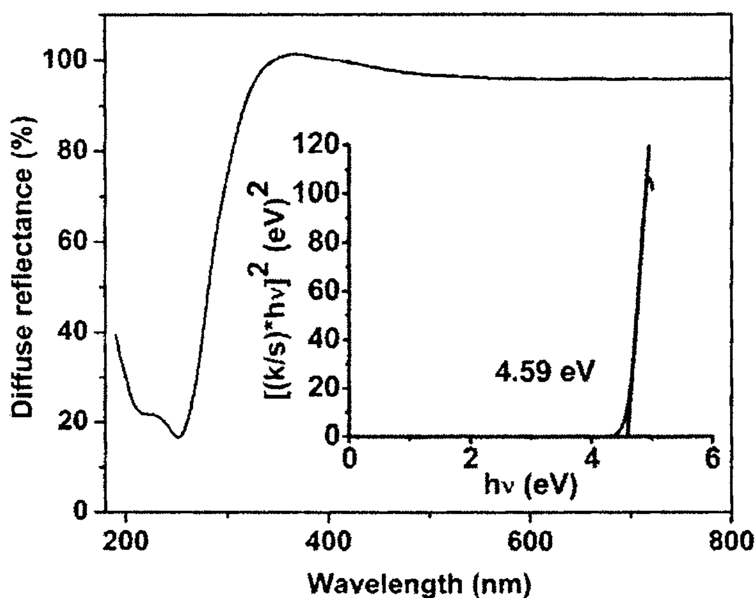

Figure 3.4. Diffuse reflectance spectrum of bulk $ZnGa_2O_4$. Inset shows the $\{(k/s).h\nu\}^2$ versus energy plot for band gap estimation

The band gap of the deposited films was obtained by recording the transmission spectra. The films exhibited an average transparency of 60% in the visible regime. It was observed that the transparency of the films reduced on increasing the reactive gas pressure within the chamber. The transmission spectra of $ZnGa_2O_4$ film deposited at 0.001 mbar pressure is shown in the figure 3.5. The

band gap was determined from the Tauc plot ie. $(\alpha h\nu)^2$ versus $h\nu$ curve (inset of figure 3.5) by extrapolating the linear portion of the curve to $h\nu = 0$. The band gap was found to be 4.7 eV, comparable to that of bulk $ZnGa_2O_4$.

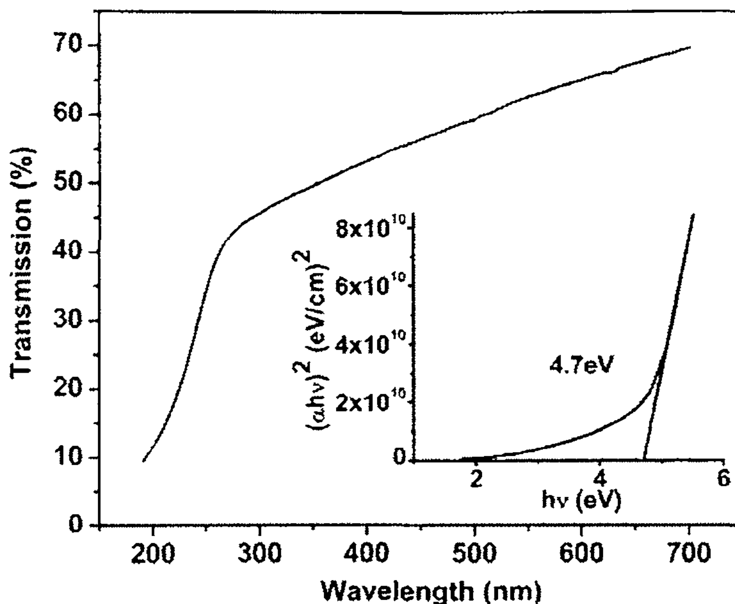

Figure 3.5. Transmission spectrum of $ZnGa_2O_4$ film grown on quartz substrate at 0.001 mbar. Inset shows the plot of $(\alpha h\nu)^2$ versus energy

The photoluminescent (PL) emission and excitation spectra (PLE) of bulk $ZnGa_2O_4$ and as-deposited $ZnGa_2O_4$ film at 0.001 mbar recorded at room temperature is shown in figure 3.6. An asymmetric broad band blue PL emission, extending from 350 to 700 nm, is observed in the case of bulk $ZnGa_2O_4$ under an excitation wavelength of 270 nm. The emission maximum at 437 nm (2.84 eV) corresponds to the $^4T_2 \rightarrow {}^4A_2$ transition arising from the self activated centers in the octahedral Ga-O group in the spinel lattice [19, 20]. The

interaction of the Ga^{3+} ions with the six oxygen ligands lifts off the degeneracy of the 3d energy levels in the regular octahedral crystal field giving rise to an energy level diagram [20] as shown in figure 3.7.

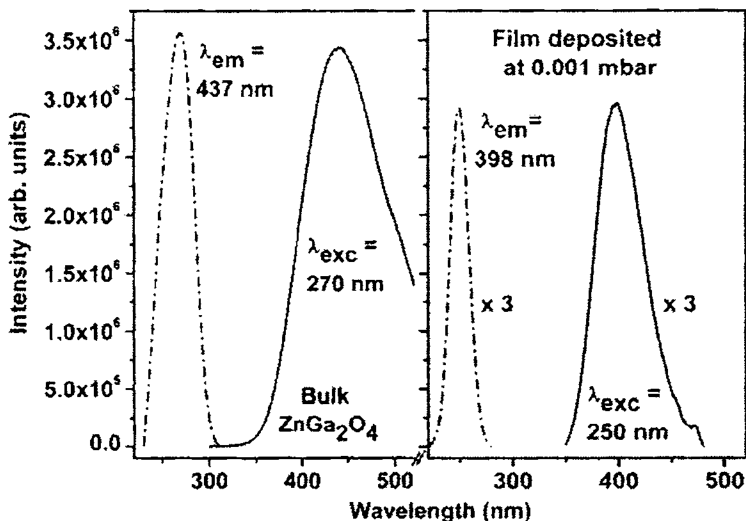

Figure 3.6. Room temperature PL emission (solid) and excitation (dotted) spectra of bulk $ZnGa_2O_4$ and as-deposited $ZnGa_2O_4$ film at 0.001 mbar

The room temperature PL emission spectra of $ZnGa_2O_4$ thin film deposited at 0.001 mbar also shows a broad band with maximum emission intensity at 398 nm (3.12 eV), under an excitation wavelength of 250 nm (figure 3.6). The blue emission corresponds to energy relaxation of electrons transiting from $^4T_1$ to $^4A_2$ energy levels of the distorted Ga-octahedral structure [21]. The peak emission wavelength of the as-deposited film is found to blue shift with respect to the bulk phosphor. This is due to the oxygen deficiency in the PLD synthesized films. Ga^{3+} ions now occupy a distorted octahedral position in the spinel

structure. The splitting of the degenerate 3d energy levels in such a crystal field [20] is also shown in figure 3.7.

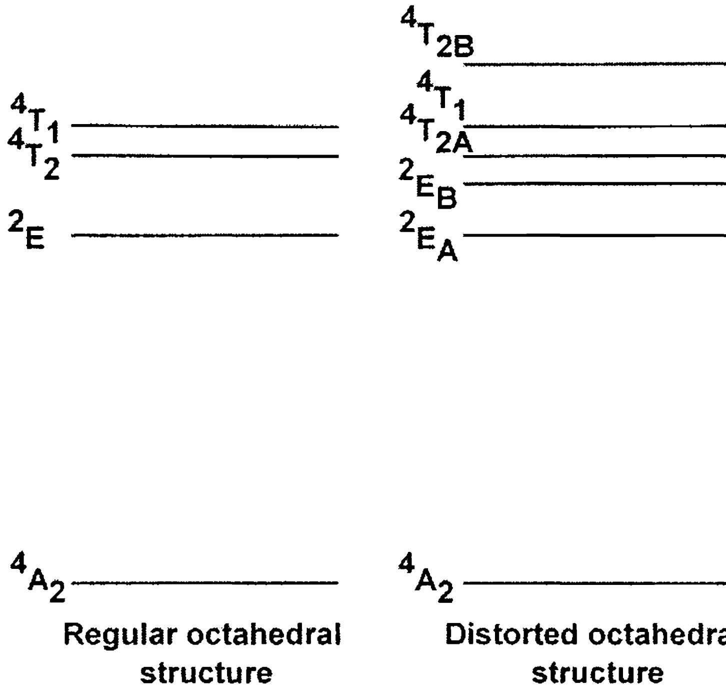

Figure 3.7. Crystal field splitting of the degenerate 3d energy levels in regular octahedral and distorted octahedral structures

Crystal field at octahedral symmetry, D_q, is related to the distance between the center ion and ligand ions (R), mean size of the d electron of the center ion (r) and ligand charge (Z) through the relation

$$D_q = \frac{3Ze^2r^4}{5R^5} \quad (3.1.)$$

The effect of ligand charge on the crystal field is the dominant factor here. The formation of oxygen vacancies reduces the ligand charge thereby leading to structural distortions in Ga–O octahedrons. The decrease in the crystal field due to a loss in site symmetry may be responsible for the blueshift observed [22, 23].

The luminescent intensity of the thin film is very poor compared to the bulk phosphor. This may be primarily due to the optical confinement of light due to planar interfaces in thin film phosphors. Factors like internal reflection, small interaction volume between incident beam and the solid and absorption of generated light by substrate materials also contribute to the decreased luminescent output.

3.4. Effect of post-deposition annealing in air

Post-deposition annealing in air was carried out to improve the crystallinity of the $ZnGa_2O_4$ films. The effect of post-annealing at 500°C in air on the XRD pattern for the films deposited at various oxygen pressures is shown in figure 3.8. All the films exhibited the secondary Ga_2O_3 phase on post-annealing. The evaporation of Zn from the films might have promoted this behavior in the post-annealed films. Such Zn deficiency phenomenon is observed in the $ZnGa_2O_4$ phosphor films owing to the high vapor pressure of Zn (192.2 Pa at 692.73 K) [24] compared to that of Ga.

The (111) peak of $ZnGa_2O_4$ totally disappeared on annealing the film deposited at 0.005 mbar. The film deposited at 0.01 mbar exhibited the secondary phase of

Ga_2O_3 that was absent before post-annealing. The film deposited at the lower oxygen pressure of 0.001 mbar showed a consistent behavior before and after air annealing.

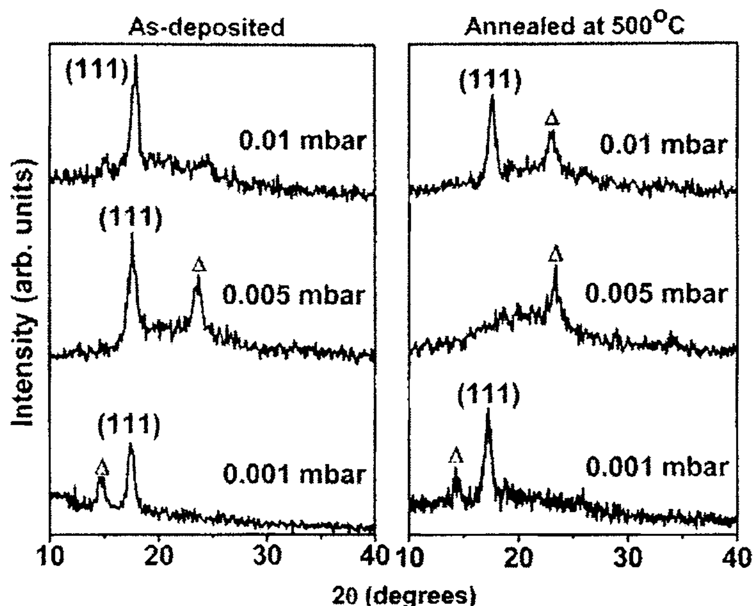

Figure 3.8. X-ray diffraction patterns of $ZnGa_2O_4$ thin films at various oxygen pressures, as-deposited (left) and post-annealed in air (right); Δ–Ga_2O_3 peak

The as-deposited films at 0.001 mbar were therefore post-annealed in air at different temperatures, the XRD patterns of which are shown in figure 3.9. The secondary phase of Ga_2O_3 was present at all annealing temperatures. Figure 3.10 shows the variation in the integral intensity and FWHM of the (111) spinel peak on post-annealing the $ZnGa_2O_4$ films deposited at 0.001 mbar at various temperatures in air ambient. The crystalline nature of the film improved on post-annealing in air at 400°C as is evident from the increase in the integral intensity

of the (111) diffraction peak and reduction in FWHM. The integral intensity of the (111) peak fell beyond 400°C due to the decrease in the atomic concentration of Zn on increasing the annealing temperature. EDX studies do confirm that the cation composition ratio decreased with increase in post-annealing temperature, as is shown in figure 3.11.

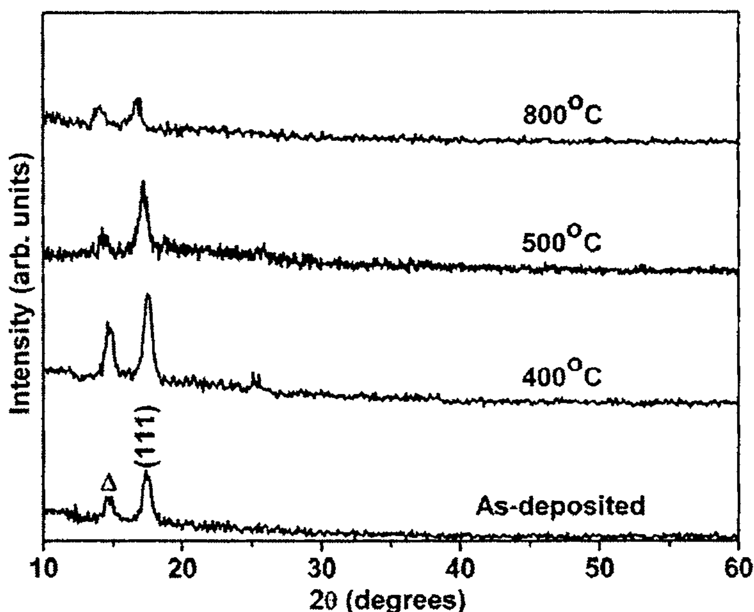

Figure 3.9. XRD patterns of of $ZnGa_2O_4$ thin films deposited at 0.001 mbar and post-annealed in air at various temperatures; Δ–Ga_2O_3 peak

The FWHM of the (111) spinel peak increased from 0.59° to 0.66° on increasing the post-annealing temperature from 400°C to 800°C (see figure 3.10). Due to the inverse relation between FWHM and grain size (given by Scherrer), a corresponding reduction in grain size is observed with increase in post-annealing temperature. Such reduction in grain size favors the luminance properties in low

voltage phosphors, reports Minami *et al.* [25], since thin films have a large surface area per unit volume.

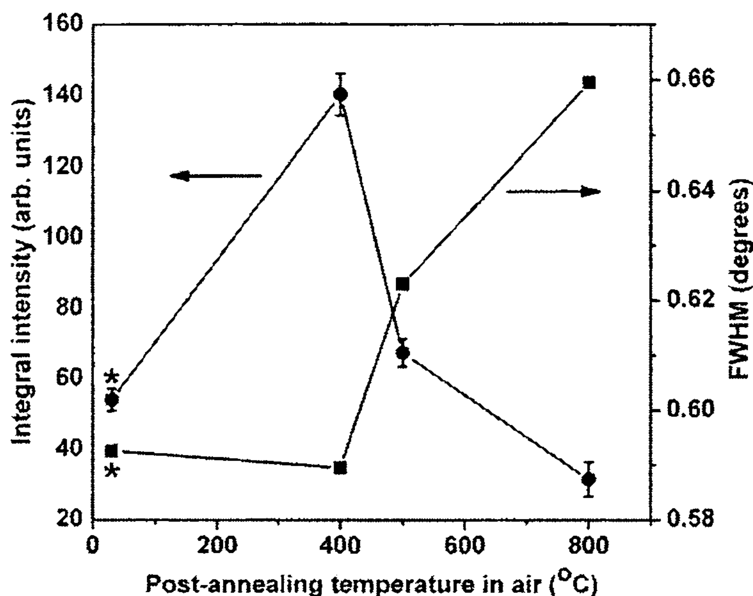

Figure 3.10. Variation of integral intensity and FWHM of the (111) spinel peak with post-annealing temperature, * denotes the corresponding values for as-deposited film

The 2θ value of the (111) peak shifts to lower diffraction angles (figure 3.9.) by an amount 0.68° which reflects an increase in the lattice parameter. Beyond its vapor pressure [24], Zn evaporation from the films will increase the concentration of oxygen vacancies to maintain charge balance in the film. Such oxygen deficiency leads to lattice expansion of the spinel structure due to cation-cation repulsion.

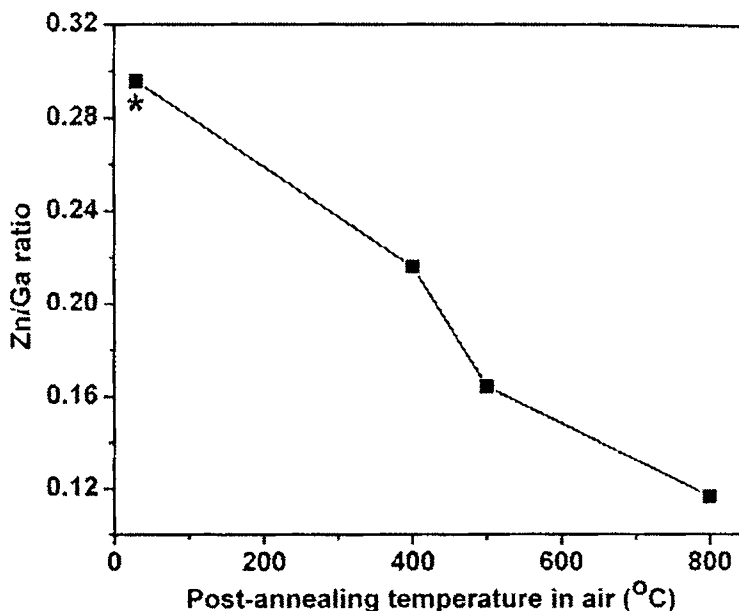

Figure 3.11. Variation of Zn/Ga ratio with post-annealing temperature for the films deposited at 0.001 mbar, * denotes the composition ratio of the as-deposited film

Figure 3.12 compares the effect of post-deposition annealing on the PL emission spectra of the as-deposited phosphor films at 0.001 mbar. Post-deposition annealing in air improved the luminescence of the $ZnGa_2O_4$ phosphor films in comparison to that of the as-deposited samples. The presence of Zn vacancies in the films has not affected the emission wavelength but enhanced the emission intensity.

The film annealed at 400°C showed more than a two fold increase in luminescence due to the improved crystallinity. The luminescence improved significantly on increasing the annealing temperature to 800°C, even when there

was an increase in FWHM. This is due to the large surface area per unit volume of $ZnGa_2O_4$ phosphor films, it being a low voltage phosphor [25]. Moreover, the reduction in grain size suppresses the backscattering of the incident photons, thereby improving the luminescent output [24]. It has also been reported that Zn deficient films exhibit better luminescent behavior than stoichiometric films. Here, excess Ga atoms can act as sensitizing sites [26].

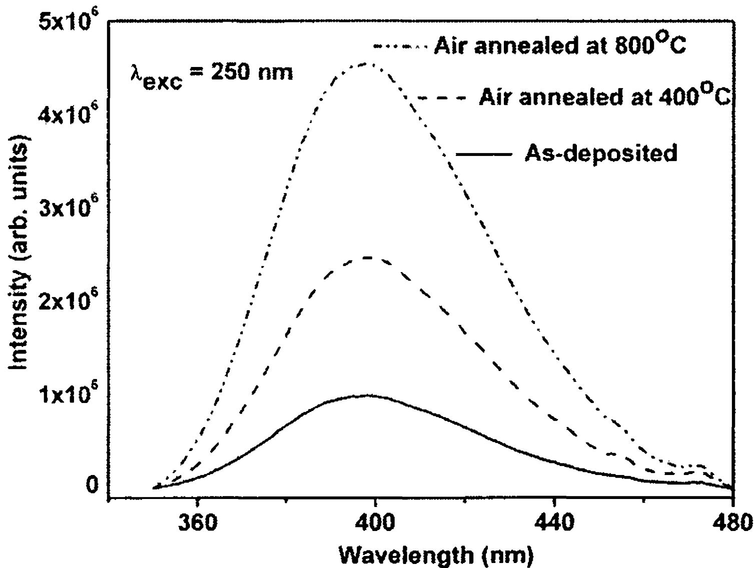

Figure 3.12. Room temperature PL emission spectra of the as-deposited and air annealed films

The PL emission of the samples was gauged using the Commission Internationale de l'Eclairage (CIE) chromaticity coordinates. The color coordinates of the synthesized $ZnGa_2O_4$ powder and the PLD grown films are given in table 3.1. The CIE 1931 2° color matching functions (CMFs) for the visible regime has been used for the same. The chromaticity coordinates

suggests that the films as well as the bulk phosphor exhibit bluish emission. CIE coordinates of bulk $ZnGa_2O_4$ powder synthesized in the laboratory was determined to be (x, y) = (0.138, 0.085). On analyzing the color coordinates of the films, one can understand that the blue emission of the films is less pure in comparison to that of the bulk.

Sample	Deposited at	Oxygen pressure (mbar)	Post-annealing temperature (°C)	(x,y)
Bulk $ZnGa_2O_4$	-	-	-	(0.138, 0.085)
Film	RT	0.001	-	(0.151, 0.034)
Film	RT	0.005	-	(0.148, 0.039)
Film	RT	0.01	-	(0.15, 0.035)
Film	RT	0.001	400°C	(0.147, 0.041)
Film	RT	0.001	800°C	(0.149, 0.037)

Table 3.1. CIE color coordinates of the synthesized $ZnGa_2O_4$ powder and the PLD grown thin films at room temperature (RT)

3.5 Conclusion

The chapter presents the relevant observations made during the attempt to deposit zinc gallium oxide phosphor thin films on amorphous substrates by pulsed laser deposition. Thin films of the spinel oriented along the (111) plane

could be deposited on quartz substrate at room temperature. Structural and optical properties of the deposited thin films were analysed. The crystallinity of the films prepared at the reduced processing temperature were found to be highly dependent on the deposition parameters like ambient oxygen pressure inside the deposition chamber, duration of deposition, laser power and substrate to target distance. A blue PL emission was obtained for the $ZnGa_2O_4$ films prepared at the very low processing temperatures. Post-deposition annealing in air could improve the crystallinity and the luminescent characteristics of the as-deposited films. It is therefore possible to deposit highly refractory oxide phosphor materials on thin, flexible and thermally unstable polymer substrates. The work also aims at the realization of zinc gallate active ACTFEL devices on low temperature substrates instead of ceramic substrates that withstand high temperature treatments.

References

1. S. Itoh, H. Toki, Y. Sato, K. Morimoto and T. Kishino, *J. Electrochem. Soc.*, **138**, 1509 (1991).
2. T. Minami, Y. Kuroi, T. Miyata, H. Yamada and S. Takata, *J. Lumin.*, **72-74**, 997 (1997).
3. M. Flynn and A. H. Kitai, *J. Electrochem. Soc.*, **148**, H149 (2001).
4. C. Sella, J. C. Martin and Y. Charreire, *Thin Solid Films*, **90**, 181 (1982).
5. D. B. Chrisey and G. K. Hubler; *Pulsed Laser Deposition of Thin Films*, p.229, John Wiley and sons Inc., New York (1994).
6. G. A. Hirata, J. McKittrick, L. E. Shea, O. A. Lopez and M. Avalos-Borja, *J.*

Soc. Inf. Disp., **4**, 347 (1996).

7. Y. E. Lee, D. P. Norton, J. D. Budai, C. M. Rouleau and J. W. Park, *J. Electroceram.*, **4**, 293 (2000).
8. Y. E. Lee, D. P. Norton, C. Park and C. M. Rouleau, *J.Appl.Phys.*, **89**, 1653 (2001).
9. S. S. Yi, I. W. Kim, J. S. Bae, B. K. Moon, S. B. Kim and J. H. Jeong, *Mater. Lett.*, **57**, 904 (2002).
10. I. Ahmad Md., M. Kottaisamy, N. Rama, M. S. R. Rao and S. S. Bhattacharya, *Scr. Mater.*, **54**, 237 (2006).
11. S. S. Yi, J. S. Bae, B. K. Moon, J. H. Jeong, I. W. Kim and H. L. Park, *Appl. Phys. A*, **76**, 433 (2003).
12. Y. E. Lee, D.P. Norton and J.D. Budai, *Appl. Phys. Lett.*, **74**, 3155 (1999).
13. JCPDS card No. 38-1240.
14. D. M. Saylor, B. E. Dasher, Y. Pang, H. M. Miller, P. Wynblatt, A. D. Rollett and G. S. Rohrer, *J. Am. Ceram. Soc.*, **87**, 724 (2004).
15. JCPDS card No. 76-0573.
16. JCPDS card No. 74-1776.
17. P. Kubelka and F. Munk, *Zh. Tekh. Fiz.*, **12**, 593 (1931).
18. P. Kubelka, *J. Opt. Soc. Am.*, **38**, 448 (1948).
19. I. K. Jeong, H. L. Park and S. I. Mho, *Solid State Comm.*, **105**, 179 (1998).
20. I. J. Hsieh, K. T. Chu, C. F. Yu and M. S. Feng, *J. Appl. Phys.*, **76**, 3735 (1994).
21. S. H. Yang, *J. Electron. Mater.*, **33**, L1 (2004).
22. J.S Kim, H.L. Park, C.M Chon, H.S. Moon and T.W. Kim, *Solid State Comm.*, **129**, 163 (2004).

23. P. D. Rack and P. H. Holloway, *Mater. Sci. Engng.*, **R21**, 171 (1998).
24. S. H. Yang, T. J. Hsueh and S. J. Chang, *Jpn. J. Appl. Phys.*, **46**, 4166 (2007).
25. T. Minami, Y. Kuroi and S. Takata, *J. Vac. Sci. Technol. A*, **14**, 1736 (1996).
26. I. J. Hsieh, M. S. Feng, K. T. Kuo, and P. Lin, *J. Electrochem. Soc.*, **141**, 1671 (1994).

Chapter 4

Synthesis of a novel white oxide phosphor :

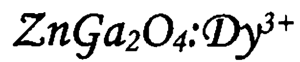

4.1. Introduction

A major challenge in the area of flat panel display (FPD) technology is the identification of new multicolor or white light emitting phosphor materials for industrial applications. A suitable blend of the available efficient blue, green and red phosphors and light emitting diodes (LEDs) [1] is the technique adopted for white light generation in the solid state lighting industry. The combination of a blue chip with yellow emitting phosphors [2, 3] or phosphor combinations [4-6] generated white light but the output varied with the driving conditions of the LED, suffered low reproducibility and low color rendering index due to color mixing. Higher color rendering properties could be attained by using multiphosphor blends and ultraviolet (UV) LEDs [7-9]. But the luminous efficiency of such systems was low owing to the re-absorption of emission colors and blending of two or three phosphors. A combination of UV LEDs with single phased doubly activated full color emitting phosphors [10-14] was later developed to generate white light. Codoping in a single host lattice gave desirable results with better luminous efficiency but the energy transfer between the activators, and thereby the output, were found to be sensitive to the activator concentrations. Therefore, the identification of singly activated single phase phosphors capable of UV excitation would be a better alternative.

Liu *et al.* [15] reported on the luminescent properties of a white afterglow phosphor $CdSiO_3$:Dy^{3+}. $CaAl_2O_4$:Dy^{3+} is another known white light long lasting phosphor [16]. White light emission from Eu^{3+} has been realized in the $CaIn_2O_4$ host lattices by suitably tuning the doping concentrations [17].

Rare earth (RE) ions serve as excellent activators in modern lighting and display fields owing to their characteristic emissions from 4f-4f or 5d-4f transitions. The phosphor hosts activated with RE ions possess a strong and broad absorption band in the UV or VUV region of the electromagnetic spectrum for efficient and effective excitation. This is because RE ions strongly absorb in the short wavelength of the UV region and weakly absorb in the near UV to blue spectral region. Trivalent dysprosium, a rare earth with $4f^9$ electronic configuration, is known to emit two intense fluorescence transitions, $^4F_{9/2} \rightarrow {}^6H_{15/2}$ in the blue and $^4F_{9/2} \rightarrow {}^6H_{13/2}$ in the yellow-orange wavelength region. The latter, being a hypersensitive transition ($\Delta L = 2$, $\Delta J = 2$), is strongly influenced by the crystal field environment. At a suitable yellow-to-blue intensity ratio, Dy^{3+} will emit white light [18]. Unlike the RE dopants Eu^{3+} and Tb^{3+} (in oxide hosts), the luminescence of Dy^{3+} cannot be excited using the common fluorescent lamps that have a strong and broad absorption band around 254nm. This is because the charge transfer absorption band (CTB) and $4f^9$ - $4f^85d$ excitation band of Dy^{3+} are located below 200nm. The excitation can occur only by the f-f transitions with low oscillator strength (10^{-6}) due to their forbidden features by the parity selection rule [19]. This drawback of Dy^{3+} luminescence can be overcome either by host sensitization [20, 21] or by impurity ion sensitization [19, 22]. Here, the effects of doping Dy^{3+} in $ZnGa_2O_4$ are investigated.

4.2. Experimental

Stoichiometric $ZnGa_2O_4$:Dy^{3+} powder phosphors were prepared by conventional high temperature solid state reaction. Adequate amounts of the starting

materials, namely ZnO (99.99%, Alfa Aesar), Ga_2O_3 (99.99%, Alfa Aesar) and Dy_2O_3 (99.99%, Indian Rare Earths Ltd.), weighed to an accuracy of ± 0.001 mg were hand mixed thoroughly under ethanol medium in an agate mortar and pestle and allowed to dry. The dried mixture was then placed in an alumina boat and introduced into the hot temperature zone of a horizontal tube furnace equipped with a proportional integral differential (PID) controller. The firing was done at 1350°C for 12 hours in air. The doping concentration of Dy^{3+} was varied in the range 0.25 to 3 at. %. For comparison, $Zn_{1-x}Ga_2O_4:Dy_x$ (x = 0, 0.02 ie. pure and 2 at. % doped sample where Dy^{3+} replaces Zn^{2+}) and $Ga_{2(1-x)}O_3:Dy_{2x}$ (x = 0.02 ie. 2 at. % doped sample) phosphors were also prepared via similar routes. The crystal structure of the powder phosphors was analyzed using x-ray powder diffraction method on a Rigaku diffractometer using Cu K_α radiation ($1.5414A^0$). The diffuse reflectance spectra (DRS) were recorded to analyze the band gap using JASCO V-570 spectrophotometer with an integrating sphere attachment, $BaSO_4$ being the reference. The room temperature photoluminescent emission (PL) and excitation (PLE) spectra were recorded using Spex Fluoromax-3 Spectrofluorimeter equipped with a 150W Xenon lamp as the excitation source.

4.3. Results and discussion

The x-ray diffraction patterns of the fired $ZnGa_{2(1-x)}O_4:Dy_{2x}$ samples matched well with the standard reflections of the host $ZnGa_2O_4$ for all dopant concentrations. The XRD patterns of $ZnGa_{2(1-x)}O_4:Dy_{2x}$ for x = 0.0025, 0.0075, 0.0125, 0.0175, 0.0225 and 0.0275 are shown in figure 4.1.

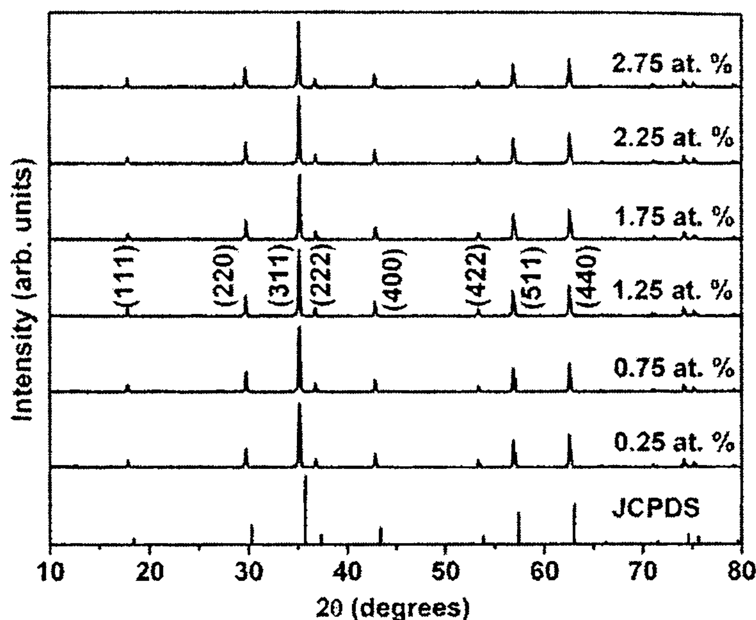

Figure 4.1. XRD patterns of $ZnGa_{2(1-x)}O_4$:Dy_{2x} (x = 0.0025. 0.0075, 0.0125, 0.0175, 0.0225, 0.0275); JCPDS data of $ZnGa_2O_4$ is given for reference

No peaks were detected that corresponded to either any of the starting materials or other allotropic forms. The absence of any secondary phase indicates that all the samples have crystallized in the spinel structure similar to that of the host and that the dopant ions have been successfully dissolved into the host lattice. Also, the structural analysis didn't show any solubility limit of the dopant in the oxide host within the selected range. Figure 4.2 shows the XRD patterns of $ZnGa_{1.96}O_4$:$Dy_{0.04}$, $Zn_{0.98}Ga_2O_4$:$Dy_{0.02}$, and $Ga_{1.96}O_3$:$Dy_{0.04}$. The diffraction patterns of $Zn_{0.98}Ga_2O_4$:$Dy_{0.02}$ and $Ga_{1.96}O_3$:$Dy_{0.04}$ also resembled their respective host reflections. JCPDS data of the normal spinel $ZnGa_2O_4$ and monoclinic Ga_2O_3 is given for reference [23, 24].

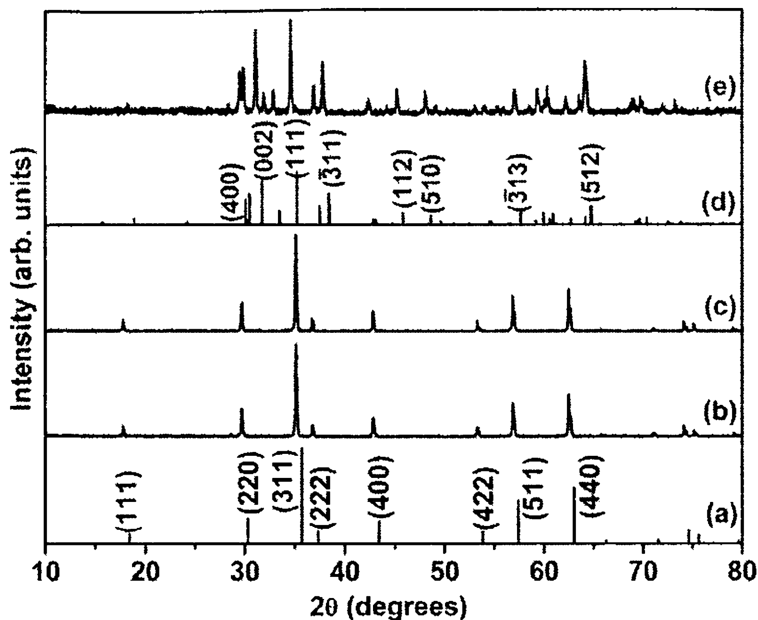

Figure 4.2. XRD patterns of (a) JCPDS data of $ZnGa_2O_4$ (b) $ZnGa_{1.96}O_4$:$Dy_{0.04}$ (c) $Zn_{0.98}Ga_2O_4$:$Dy_{0.02}$ (d) JCPDS data of Ga_2O_3 (e) $Ga_{1.96}O_3$:$Dy_{0.04}$

DRS of the 2.5 at. % Dy^{3+} doped sample is shown in figure 4.3. The band gap of the sample was determined to be 4.45 eV from the $[(k/s)\ h\nu]^2$ versus $h\nu$ curves [25, 26] (inset of figure 4.3) obtained from diffuse reflectance measurements. The band gap values of all the doped samples fall in the range 4.48 ± 0.05 eV, close to the reported value of 4.59 eV for pure $ZnGa_2O_4$. Apart from the main absorption band corresponding to the valence to conduction band transition in the host, a shoulder-like absorption band appears in the Dy^{3+} doped samples attributable to the 4f - 4f transitions of Dy^{3+} within its $4f^9$ ground state configuration. On increasing the dopant concentration, this shoulder-like absorption was found to increase (figure 4.4.). This ensures the fact that as x

increases, more and more dopant ions get incorporated into the host lattice. Also, all the doped samples have their main absorption at the fundamental absorption edge of the host.

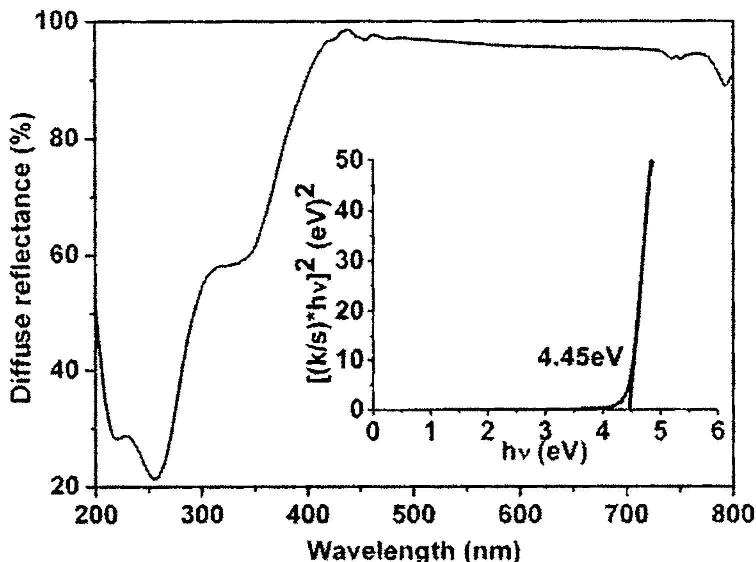

Figure 4.3. Diffuse reflectance spectra of $ZnGa_{1.95}O_4:Dy_{0.05}$ powder. Inset shows the $\{(k/s)h\nu\}^2$ versus hν plot used for bandgap estimation

Figure 4.5 shows the PL emission spectra of pure and 2.5 at. % Dy^{3+} doped $ZnGa_2O_4$ samples for an excitation wavelength of 270 nm. The undoped sample shows a strong broad blue luminescence with a peak at 439 nm resulting from the self-activated transition of regular O_h Ga-O groups [27]. The emission spectrum of the Dy^{3+} doped sample exhibits both the host emission band and the characteristic fluorescence transitions $^4F_{9/2} \rightarrow {}^6H_J$ (J = 15/2, 13/2, 11/2, 9/2) of Dy^{3+} ions. The host emission band extending from UV to the blue region, with

peak maximum at 441 nm, has been very much lowered in intensity in comparison to that of the bulk.

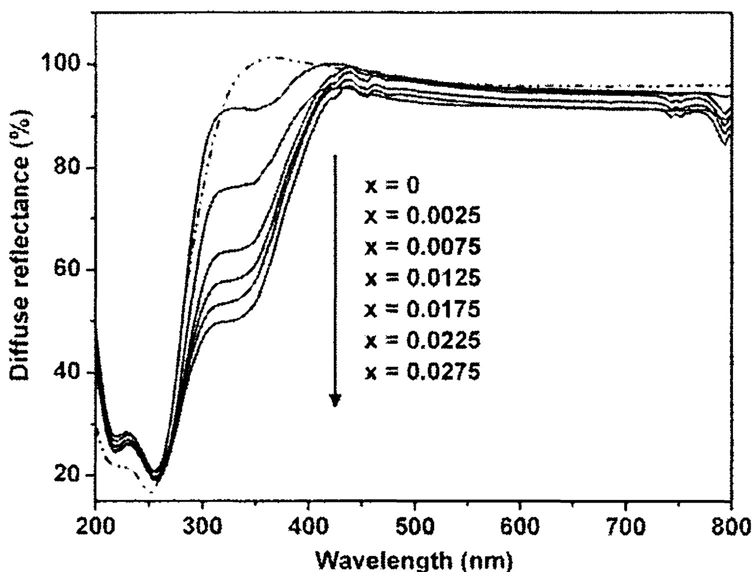

Figure 4.4. Diffuse reflectance spectra of bulk $ZnGa_2O_4$ (dotted) and $ZnGa_{2(1-x)}O_4:Dy_{2x}$ (solid) varying the dopant concentrations

There are four groups of characteristic lines in the dopant emission spectra - lines in the blue region (450-510 nm), lines in the yellow region (560-610 nm) and two groups of line spectra in the red region (660-720 nm and 755-800 nm) with their peak maxima at 499 nm, 589 nm, 692 nm and 778 nm respectively. These emissions correspond to the spectral transitions $^4F_{9/2} \rightarrow {}^6H_{15/2}$, $^4F_{9/2} \rightarrow {}^6H_{13/2}$, $^4F_{9/2} \rightarrow {}^6H_{11/2}$ and $^4F_{9/2} \rightarrow {}^6H_{9/2}$ respectively, the dominant one being $^4F_{9/2} \rightarrow {}^6H_{15/2}$. The crystal field had sufficient strength to lift off the degeneracy of the free ion states of Dy^{3+} in the lattice so that well resolved Stark levels of the multiplet manifolds could be observed in the spectra.

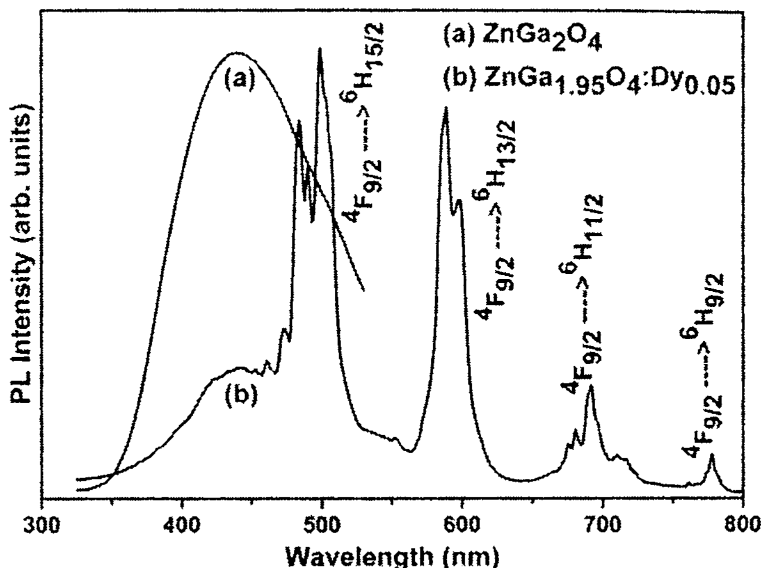

Figure 4.5. Room temperature PL emission spectra of (a) pure $ZnGa_2O_4$ host and (b) 2.5 at. % Dy^{3+} doped sample, λ_{exc} = 270nm

The integral intensity of the blue emission ($^4F_{9/2} \rightarrow {}^6H_{15/2}$) is stronger than that of the yellow ($^4F_{9/2} \rightarrow {}^6H_{13/2}$) and red emissions ($^4F_{9/2} \rightarrow {}^6H_{11/2}$ and $^4F_{9/2} \rightarrow {}^6H_{9/2}$) for all dopant concentrations, as is evident from figure 4.6. This spectral property of Dy^{3+} provides some information on the site occupation of Dy^{3+} in the host lattice. It is well known that the $^4F_{9/2} \rightarrow {}^6H_{13/2}$ yellow emission of Dy^{3+} is a hypersensitive transition that is strongly influenced by the crystal field environment [18]. When Dy^{3+} is located at a low symmetry local site (without an inversion symmetry), the yellow emission dominates the PL spectrum. On the other hand, the blue emission $^4F_{9/2} \rightarrow {}^6H_{13/2}$ will be dominant in the emission spectrum if Dy^{3+} occupies a high symmetry local site (with inversion symmetry) [20]. In the host lattice of $ZnGa_2O_4$, Zn^{2+} ions occupy tetrahedral sites (T_d point

symmetry without inversion center) coordinated by four oxygen atoms and Ga^{3+} ions occupy octahedral sites (O_h point symmetry with inversion center) coordinated by six oxygen atoms.

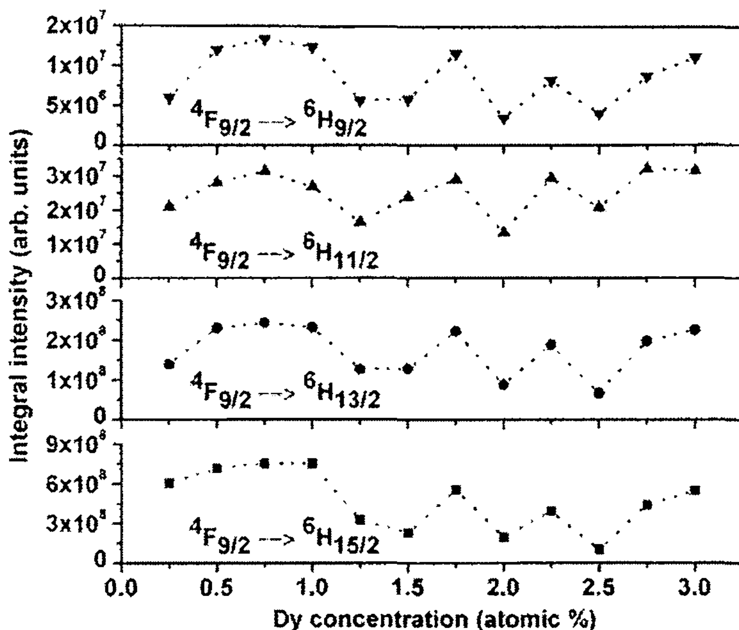

Figure 4.6. Variation of the integral intensity of the characteristic transitions of Dy^{3+} with dopant concentration

Since the blue emission dominates in the spectrum of all the samples, one can be sure that Dy^{3+} replaces Ga^{3+} more in the spinel structured host. Moreover, the ionic radii of Dy^{3+} (0.0912 nm) is more compatible with Ga^{3+} (0.062 nm) for six coordination than that for four coordination (0.047 nm) [28]. Though the ionic radii of Zn^{2+} is 0.074 nm for six coordination, Dy^{3+} ions rarely substitutes at its tetrahedral site due to charge imbalance.

The integral intensity of the $^4F_{9/2} \rightarrow {}^6H_J$ transitions of Dy_{3+} ions is found to vary irregularly with dopant concentration in figure 4.6. This may be because the energy levels of Dy^{3+} ions in the spinel host may be highly sensitive to the lattice variations. On increasing the dopant incorporation into the host, the lattice parameter, calcualetd from the XRD data, was also found to vary irregularly. This will inturn influence the local field around the dopant ions and further affect other parameters such as the lifetime of excited states and transition probability [29].

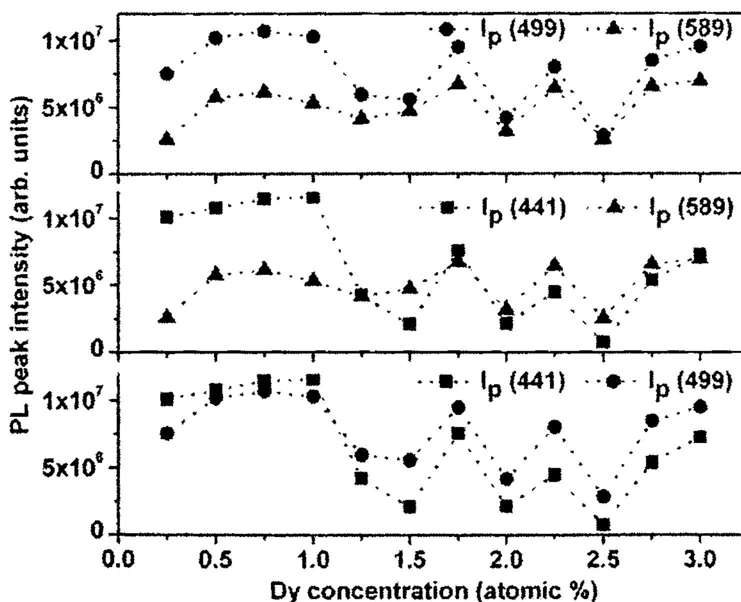

Figure 4.7. Variation in the PL peak intensities I_p at 441 nm, 499 nm and 589 nm with dopant concentration

The room temperature PL emission spectra of all the $ZnGa_{2(1-x)}O_4:Dy_{2x}$ samples were recorded at an excitation wavelength of 270 nm. Figure 4.7 shows the

variation in the PL peak intensities at 441 nm, 499 nm and 589 nm (abbreviated as I_p (441), I_p (499) and I_p (589) respectively) with dopant concentration. For dopant concentrations at and below 1 at. %, the blue emission band of the host is more intense than the luminescent transitions of the activator. Beyond 1 at. % doping, the host emission weakens and the characteristic luminescent transitions of the activator ions predominate the PL spectrum. The peak intensity of the Dy^{3+} $^4F_{9/2} \rightarrow {}^6H_{15/2}$ transition is always greater than that of the $^4F_{9/2} \rightarrow {}^6H_{13/2}$ fluorescent transitions for any dopant concentration. To the naked eye, these luminescent emissions from the doped samples appear blue for x = 0.0025 to 0.01 and white for x = 0.0125 to 0.03.

The PLE spectrum (figure 4.8) of the Dy^{3+} doped sample, recorded at the emission wavelength of 499 nm, consists of a strong excitation band extending from 255 to 320 nm with peak maximum at 266 nm and a convolution of several weak lines (at 365, 399, 420, 425, 442 nm) in the longer wavelength region. The weak lines positioned between 320 and 445 nm are due to the f-f transitions of Dy^{3+} within its $4f^9$ ground state configuration [20]. The origin of the strong band can be correlated taking into consideration the excitation of the host. The excitation spectrum of pure $ZnGa_2O_4$ is also composed of a strong broad band ranging from 220 to 320 nm with a maximum at 271 nm, whose spectral profile almost matches that of the doped sample. This indicates that the Dy^{3+} doped samples strongly absorbs at the fundamental absorption edge of the host. Moreover, the emission band of the sensitizer ions (here, Ga^{3+}) overlaps the parity forbidden absorption band of the activator (here, Dy^{3+}) ions only to a small extent.

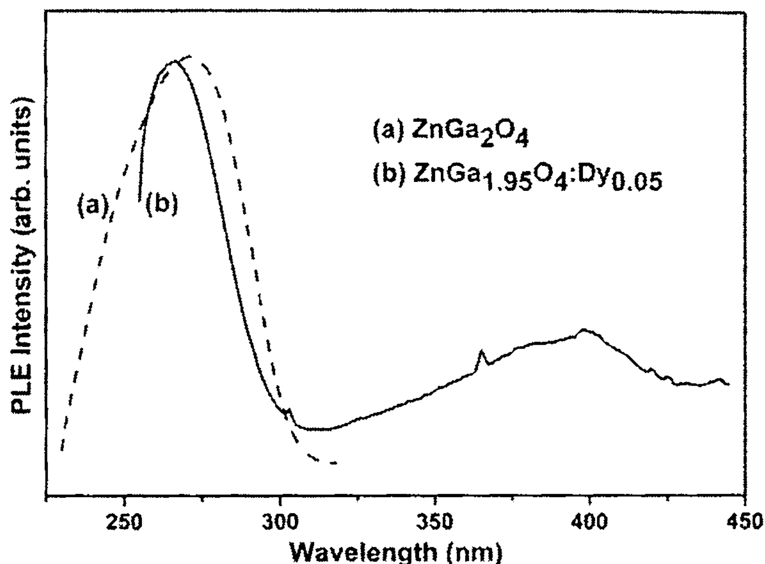

Figure 4.8. Room temperature PLE spectra of (a) pure $ZnGa_2O_4$ host (λ_{em} = 439nm) and (b) 2.5 at. % Dy^{3+} doped sample (λ_{em} = 499nm)

A luminescent material comprising of a sensitizer (S) and an activator (A) can exhibit either a radiative or a nonradiative energy transfer. Radiative transfer of energy is not very much efficient in the case of intrashell transitions due to the low magnitude of the oscillator strength for absorption [30]. The transfer rate of the nonradiative resonance transfer mechanism depends both on the spectral overlap of the S emission band and the A absorption band and on the interaction between the initial and final states of the transfer between the S and the A. The interaction can be either an exchange interaction or an electric multipolar interaction; the transfer rate in either case depending on the distance R between S and A. The R dependence is exponential for exchange interactions and R^{-n} (n = 6 for dipole - dipole interactions and 8 for dipole - quadrupole interactions) for

electric multipolar interactions. Thus, spectral overlap and distance R significantly affects energy transfer rate [31]. The energy transfer efficiency, η_T, was calculated using the relation [32],

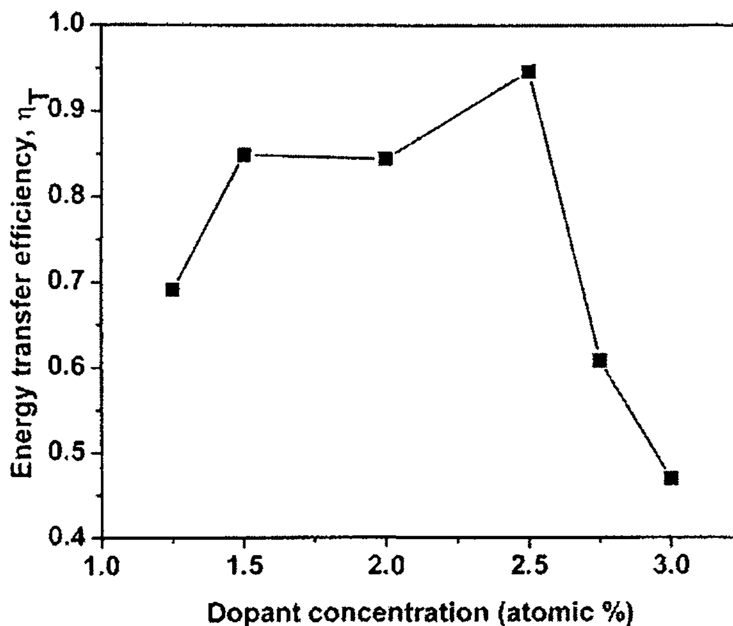

Figure 4.9. Variation of η_T with dopant concentration

$$\eta_T = 1 - \frac{I_S}{I_{S0}} \quad (4.1.)$$

where, I_S and I_{S0} are the luminescence intensity of the sensitizer (Ga^{3+}) in the presence and absence of the activator (Dy^{3+}). The variation of η_T with dopant concentration is shown in figure 4.9. The transfer efficiency was found to increase gradually with Dy^{3+} content and reached the maximum for the sample

doped with 2.5 at. % of Dy^{3+}. Hereafter, it decreased mainly due to cross-relaxation [33] ie. energy transfer from one Dy^{3+} to another by transitions that are matched in energy. This occurs because as one increases the dopant concentration, the activator ions come more and more closer.

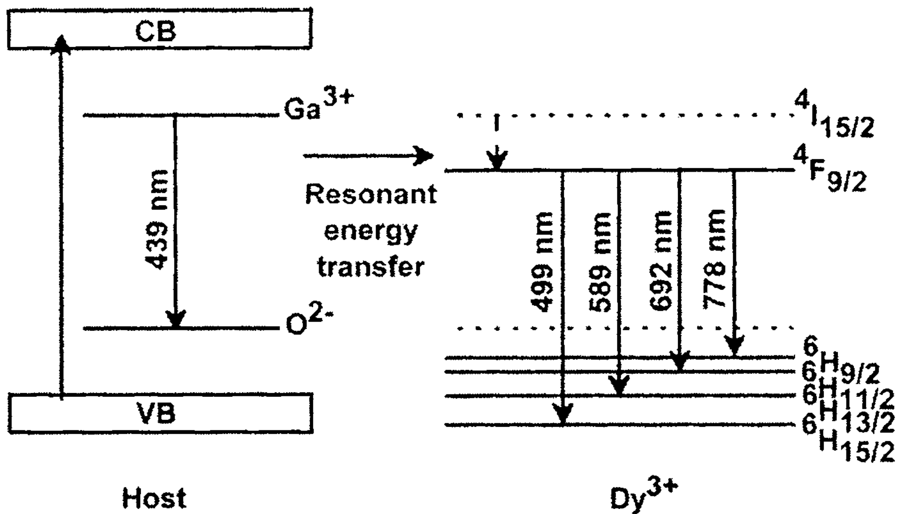

Figure 4.10. A simple model illustrating the white emission from $ZnGa_2O_4:Dy^{3+}$

A simple model illustrating the luminescent process from $ZnGa_2O_4:Dy^{3+}$ is given in figure 4.10. In this phosphor system, under UV light illumination, the band-to-band transition in the host lattice gets excited. The 439 nm emission originates from the charge transfer between Ga^{3+} at regular O_h sites and its surrounding O^{2-} [34]. The energy of the emission can only be nonradiatively transferred due to the poor spectral overlap between the $ZnGa_2O_4$ emission band and the $4f^9$ intraconfigurational absorption lines of Dy^{3+}. Since the allowed 4f - 5d absorption band of the activator ions lie far outside the zinc gallate emission

band, the energy transfer by electric multipolar interactions is less probable [31]. Thus, the nonradiative resonant energy transfer mechanism in Dy^{3+} activated $ZnGa_2O_4$ is most likely to be mediated by exchange interactions. And this will be more favoured, smaller the value of R. For this, Dy^{3+} ions must replace Ga^{3+} at its octahedral site. The presence of the host emission band in the emission spectrum of the doped sample, with reduced intensity, suggests that the host sensitized energy transfer is incomplete in $ZnGa_2O_4$:Dy^{3+} and that only a significant amount of the emitted energy is transferred from the sensitizer to the activator.

A comparison was made between the PL emission spectra of host $ZnGa_2O_4$ along with the emission spectra of $Zn_{1-x}Ga_2O_4$:Dy_x, $ZnGa_{2(1-x)}O_4$:Dy_{2x} and $Ga_{2(1-x)}O_4$:Dy_{2x} prepared under similar synthetic conditions for a doping concentration of 2 at.% (figure 4.11). The emission spectra of $Zn_{0.98}Ga_2O_4$:$Dy_{0.02}$ exhibits the UV to blue emission band of the host itself whereas that of $ZnGa_{1.96}O_4$:$Dy_{0.04}$ includes the emission band of $ZnGa_2O_4$ and the characteristic fluorescence transitions $^4F_{9/2} \rightarrow {}^6H_J$ of the dopant. The blue emission of the $Zn_{0.98}Ga_2O_4$:$Dy_{0.02}$ sample is more intense than the host. But the $ZnGa_{1.96}O_4$:$Dy_{0.04}$ compound gives weaker $ZnGa_2O_4$ emission and strong dysprosium emissions. In the former case, since Dy^{3+} is ought to substitute for Zn^{2+} at its tetrahedral site, the energy transfer via exchange interactions is greatly reduced owing to larger S-A distance (R), thereby suppressing Dy^{3+} emissions. In the latter case, Dy^{3+} emission gets enhanced as R is greatly reduced. The PL emission intensity of $Ga_{1.96}O_4$:$Dy_{0.04}$ is much stronger than

$ZnGa_{2(1-x)}O_4:Dy_{2x}$ indicating that host sensitization is more effective in the former.

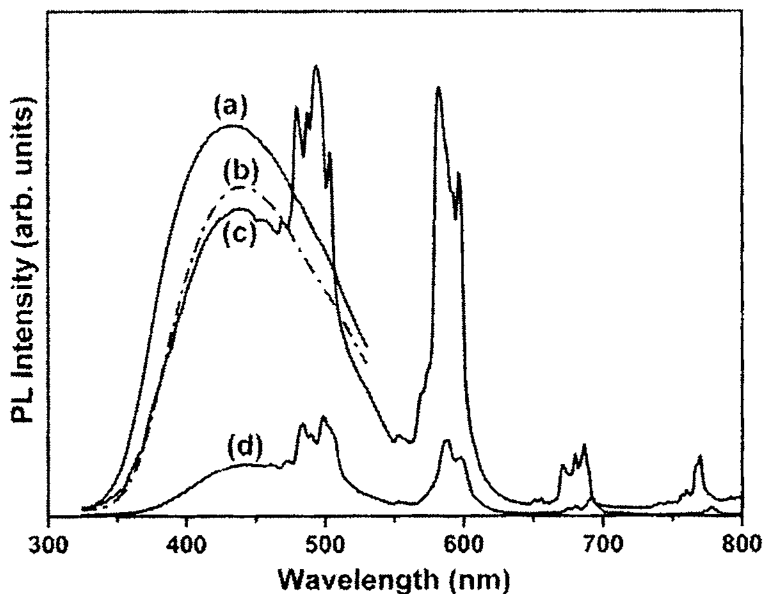

Figure 4.11. Room temperature PL emission spectra of (a) $Zn_{0.98}Ga_2O_4:Dy_{0.02}$, (b) pure $ZnGa_2O_4$, (c) $Ga_{1.96}O_4:Dy_{0.04}$ and (d) $ZnGa_{1.96}O_4:Dy_{0.04}$, λ_{exc} = 270nm

Host sensitized white luminescence is therefore exhibited by $ZnGa_{2(1-x)}O_4:Dy_{2x}$ for all dopant concentrations above 1 at. %. Figure 4.12 shows the variation of the integral intensity ratio for various dopant concentrations. Su *et al.* [18] points out that the yellow-to-blue (Y/B) intensity ratio does not vary too much with dopant concentration when Dy^{3+} substitutes for an element with the same valency in the host matrix. In the case of $ZnGa_2O_4:Dy^{3+}$, the dopant ion replaces Ga^{3+} ions of the host, as is evident from ionic radii considerations and PL emission spectra (explained above). The Y/B ratio, I_{589}/I_{441}, varies significantly

with activator incorporation, if only the host emission was considered. But the ratio, $I_{589}/(I_{441}+I_{499})$, showed little variation with respect to dopant concentration. This asserts the fact that the white luminescence observed is due to the simultaneous occurrence of the multicolor dopant emissions on host sensitization. The Y/B ratio of $Ga_{1.96}O_3$:$Dy_{0.04}$, which gave white luminescence, was found to be 0.266.

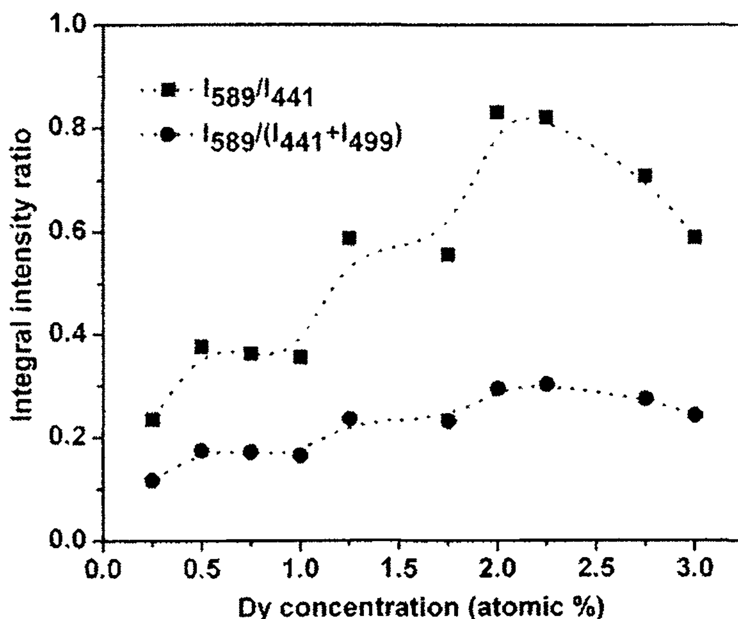

Figure 4.12. Variation of the integral intensity ratio (Y/B ratio) with dopant concentration

The PL emissions of the samples were gauged employing the CIE (Commission Internationale d'Eclairage) coordinates (figure 4.13). The CIE coordinates of the Dy^{3+} doped samples lie in between that of the $ZnGa_2O_4$ host (x = 0.14, y = 0.09) and that for achromatic white (x = 0.33, y = 0.33). The 2.5 at. % Dy^{3+} doped

sample shows the best white emission and its CIE coordinates were calculated to be x = 0.31 and y = 0.3 and it lies just to the left of achromatic white in the chromaticity diagram.

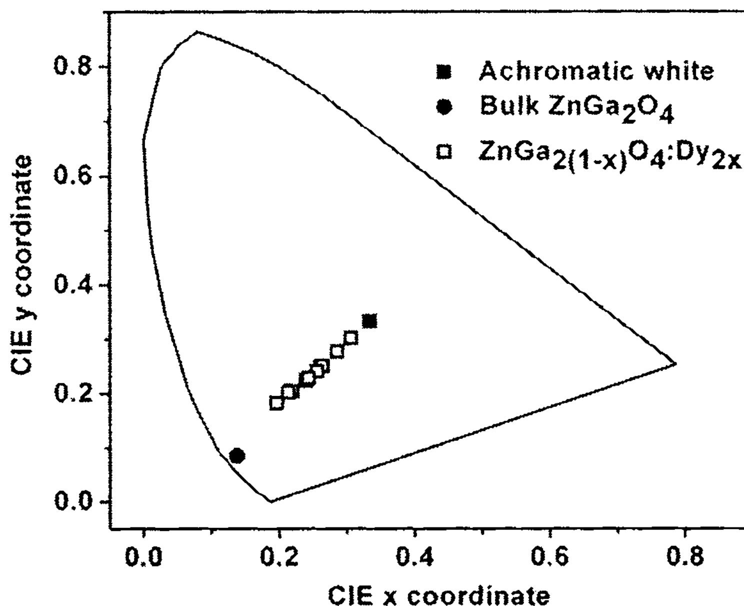

Figure 4.13. CIE chromaticity diagram of the $ZnGa_{2(1-x)}O_4:Dy_{2x}$ ($0.0025 \leq x \leq 0.025$), CIE coordinates of $ZnGa_2O_4$ host and achromatic white is shown for comparison

The chromaticity coordinates are better than that of the commercial $Y_3Al_5O_{12}$:Ce phosphor (λ_{ex} = 467 nm) reported to be (0.31, 0.27) [10]. The color coordinates of certain white emitting oxide phosphors like $CdSiO_3:Dy^{3+}$, $CaIn_2O_4$:0.5% Eu^{3+}, $SrIn_2O_4:Dy^{3+}$are found to be (0.39, 0.38) [15], (0.29, 0.31) [17], (0.3, 0.33) [21] respectively. The $Ga_{1.96}O_3:Dy_{0.04}$ sample prepared, for comparison, showed higher luminescent intensity than the Dy^{3+} doped $ZnGa_2O_4$ sample but the CIE coordinates was calculated to be x = 0.26, y = 0.24. That is, the white emission

of $Ga_{1.96}O_3$:$Dy_{0.04}$ phosphor is much inferior to that of $ZnGa_{1.95}O_4$:$Dy_{0.05}$ phosphor. The chromaticity diagram also suggests that color tuning from blue to white is possible on varying the dopant content in the spinel host.

4.4. Conclusions

$ZnGa_{2(1-x)}O_4$:Dy_{2x} phosphors were prepared by conventional solid state reaction technique. The doped samples exhibit the normal spinel phase as the host. The photoluminescent studies reveal the fact that Dy^{3+} ions replace Ga^{3+} ions in the host lattice at their octahedral sites. For dopant concentrations above 1 at. %, the Dy^{3+} doped samples give white luminescence. This emission results from a nonradiative resonant energy transfer between the host and the activator mediated by exchange interactions. The poor spectral overlap between the sensitizer's emission band and the activator's forbidden absorption band accounts for the reduced PL emission intensity of the doped samples. The best white emission is obtained for the 2.5 at. % doped sample that presented the maximum enrgy transfer efficiency, the CIE coordinates of which is found to be (x,y) = (0.31, 0.3). The present investigation highlights the possibility of Dy^{3+} doped $ZnGa_2O_4$ as an active layer in white emitting oxide based alternating current thin film electroluminescent (ACTFEL) devices.

References

1. P. Thiyagarajan, M. Kottaisamy and M. S. R. Rao, *J. Phys. D: Appl. Phys.*, **39**, 2701 (2006).

2. J. H. Yum, S. Y. Seo, S. Lee and Y. E. Sung, *J. Electrochem.Soc.*, **150**, H47 (2003).
3. J. K. Park, M. A. Lim, C. H. Kim, H. D. Park, J. T. Park and S. Y. Choi, *Appl. Phys. Lett.*, **82**, 683 (2003).
4. Y. Sato, N. Takahashi and S. Sato, *Jpn. J. Appl. Phys.*, **35**, L838 (1996).
5. Y. D. Huh, J. H. Shim, Y. Kim and Y. R. Do, *J. Electrochem. Soc.*, 150, H57 (2003).
6. J. S. Kim, J. Y. Kang, P. E. Jeon, J. C. Choi, H. L. Park and T. W. Kim, *Jpn. J. Appl. Phys.*, **43**, 989 (2004).
7. S. Neeraj, N. Kijima and A. K. Cheetham, *Chem. Phys. Lett.*, **387**, 2 (2004).
8. Y. Hu, W. Zhuang, H. Ye, D. Wang, S. Zhang and X. Huang, *J. Alloys Compd.*, **390**, 226 (2005).
9. J. S. Kim, P. E. Jeon, Y. H. Park, J. C. Choi, and H. L. Park, *Appl. Phys. Lett.*, **82**, 3696 (2004).
10. J. S. Kim, P. E. Jeon, J. C. Choi, H. L. Park, S. I. Mho and G. C. Kim, *Appl. Phys. Lett.*, **84**, 2931 (2004).
11. N. Lakshminarasimmhan and U. V. Varadaraju, *J. Electrochem. Soc.*, **152**, H152 (2005).
12. W. J. Yang and T. M. Chen, *Appl. Phys. Lett.*, **88**, 101903 (2006).
13. Y. H. Won, H. S. Jang, W. B. Im, D. Y. Jeon and J. S. Lee, *Appl. Phys. Lett.*, **89**, 231909 (2006).
14. S. H. Lee, J. H. Park, S. M. Son, J. S. Kim and H. L. Park, *Appl. Phys. Lett.*, **89**, 221916 (2006).
15. Y. Liu, B. Lei and C. Shi, *Chem. Mater.*, **17**, 2108 (2005).
16. B. Liu, C. Shi and Z. Qi, *Appl. Phys. Lett.*, **86**, 191111 (2005).

17. X. Liu, C. Lin and J. Lin, *Appl. Phys. Lett.*, **90**, 081904 (2007).
18. Q. Su, Z. Pei, L. Chi, H. Zhang, Z. Zhang and F. Zou, *J. Alloys Compd.* **192**, 25 (1993).
19. Q. Su, Z. Pei, J. Lin and F. Xue, *J. Alloys Compd.* **225**, 103 (1995).
20. W.Y. Shen, M.L. Pang, J. Lin and J. Fang, *J. Electrochem. Soc.* **152**, H25 (2005).
21. X. Liu, C. Lin, Y. Luo and J. Lin, *J. Electrochem. Soc.*, **154**, J21 (2007).
22. J. Lin and Q. Su, *J. Alloys Compd.*, **210**, 159 (1994).
23. JCPDS Card no. 38-1240.
24. JCPDS Card no. 76-0573.
25. P. Kubelka and F. Munk, *Zh. Tekh. Fiz.*, **12**, 593 (1931).
26. P. Kubelka, *J. Opt. Soc. Am.*, **38**, 448 (1948).
27. I.K. Jeong, H.L. Park and S. Mho, *Solid State Commun.*, **105**, 179 (1998).
28. R. D. Shannon, *Acta Cryst.*, **A32**, 751 (1976).
29. X. Wang, C. N. Xu and H. Yamada, *Jpn. J. Appl. Phys.*, **44**, L912 (2005).
30. Z. Xu, Y. Li, Z. Liu and D. Wang, *J. Alloys Compd.*, **391**, 202 (2005).
31. G. Blasse and A. Bril, *J. Chem. Phys.*, **47**, 1920 (1967).
32. P. I. Paulose, G. Jose, V. Thomas, N. V. Unnikrishnan and M. K. R. Warrier, *J. Phys. Chem. Solids*, **64**, 841 (2003).
33. J. L. Sommerdijk, A. Bril and F. M. J. H. Hoex-Strik, *Philips Res. Rep.*, **32**, 149 (1977).
34. J. S. Kim, H. I. Kang, W. N. Kim, J. I. Kim, J. C. Choi, H. L. Park, G. C. Kim, T. W. Kim, Y. H. Hwang, S. I. Mho, M. C. Jung and M. Han, *Appl. Phys. Lett.*, **82**, 2029 (2003).

Chapter 5

Growth of RF magnetron sputtered $ZnGa_2O_4:Dy^{3+}$ thin films

5.1. Introduction

The recent interest in developing emissive flat panel displays (FPDs), *e.g.*, full color low voltage field emission displays (FEDs), large area plasma displays (PDPs), and electroluminescent displays (ELDs) demand the quest for efficient and stable tricolor or full color phosphors. Extensive research has now been triggered in the domain of oxide phosphors owing to their excellent chemical stability over the conventional sulphide phosphors.

It has been reported that as-deposited polycrystalline oxide phosphor thin films on glass substrates often exhibit poor crystallinity and inferior luminescent properties. Efforts to alleviate these limitations have focused on increasing light scattering centers using surface modification, reducing defect density by high temperature post-deposition annealing [1] and controlling the oxidation state and crystal symmetry of the activator [2-4]. Several groups have investigated the epitaxial growth of $ZnGa_2O_4$ thin films on single crystal substrates [5, 6], comparing their properties to polycrystalline films deposited on glass substrates in an attempt to delineate the effects of microstructure on luminescent properties.

The present work aims at the growth of $ZnGa_2O_4:Dy^{3+}$ phosphor thin films on low temperature substrates using the commercial technique - rf magnetron sputtering. Sputter deposition is a relatively low cost production technique suitable for fabrication of affordable flat panel displays for the mass consumer markets [7]. The technique has been effectively used by several research groups [8-11] to deposit $ZnGa_2O_4:Mn^{2+}$ thin films as the emitting layer in EL devices.

The analysis, therefore, is intended to serve as an initial step towards the realization of oxide phosphor based TFEL devices on low temperature substrates without any post-deposition treatments (discussed in the next chapter).

5.2. Experimental

Thin films of $ZnGa_2O_4:Dy^{3+}$ were deposited on quartz substrates by RF magnetron sputtering. The target used was $ZnGa_{1.95}O_4:Dy_{0.05}$ powder prepared by the solid state reaction of constituent oxides. The starting materials, namely ZnO (99.99%, Alfa Aesar), Ga_2O_3 (99.99%, Alfa Aesar) and Dy_2O_3 (99.99%, Indian Rare Earths Ltd.), were mixed stoichiometrically in ethanol medium and then fired at 1350°C for 12 hrs. The doping concentration was fixed at 2.5 at. %. The deposition was carried out on fused silica substrates placed 4.5 cm away from the target in an Argon (Ar) ambient of 0.015 mbar at an RF power 125 W for two hours. The substrate temperature was varied between room temperature and 700°C. The thickness of the samples was measured using Dektak 6M stylus profiler and the average growth rate was found to be 0.2 nm/s. The films were structurally characterized by x-ray diffraction (XRD) technique using a Rigaku x-ray diffractometer with Cu K_α radiation at 30 kV, 20 mA and 5° (2θ) min^{-1} scanning rate. The transmission spectra were recorded using JASCO V-570 spectrophotometer. Room temperature photoluminescence (PL) emission and excitation spectra (PLE) were recorded using Jobin Yvon Fluoromax-3 spectrometer equipped with a 150 W xenon lamp. X-ray fluorescence (XRF) technique was used to study the cation composition ratio of the deposited films. Morphological analysis was done by using scanning electron microscopy (SEM) and atomic force microscopy (AFM).

5.3. Results and discussion

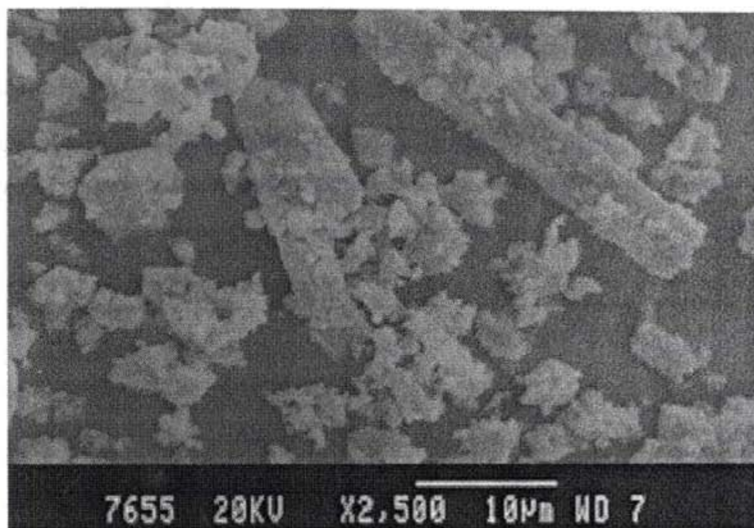

Figur 5.1. Scanning electron micrograph of $ZnGa_{1.95}O_4:Dy_{0.05}$ powder target

SEM image of the 2.5 at. % Dy^{3+} doped $ZnGa_2O_4$ target is shown in figure 5.1. The sintered powder exhibits uniform mosaic rod-like structures of $ZnGa_2O_4$ surrounded by fine particles of the same [12].

The x-ray θ - 2θ diffraction patterns of $ZnGa_2O_4:Dy^{3+}$ films (figure 5.2) matches well with the standard reflections of the bulk [13]. Highly adhesive thin films with (311) orientation could be grown even at room temperature. The broadening of the (311) peak with substrate temperature may be attributed to the strain induced in the films by the uniform incorporation or substitution of dopant ions into the host lattice. The decline in crystalline nature may also be due to the increase in Ga/Zn ratio with substrate temperature [14], as evident from XRF

studies. Also, it was observed that nucleation of grains with (311) plane as preferred orientation subdues with substrate temperature and the film growth is promoted along other planes like (440), (511) and (400). This is because surface energy plays a crucial role in film texturing, the surface area to volume ratio being large in thin films. So higher substrate temperatures provide sufficient thermal energy to promote film growth thermodynamically along the densest direction [15].

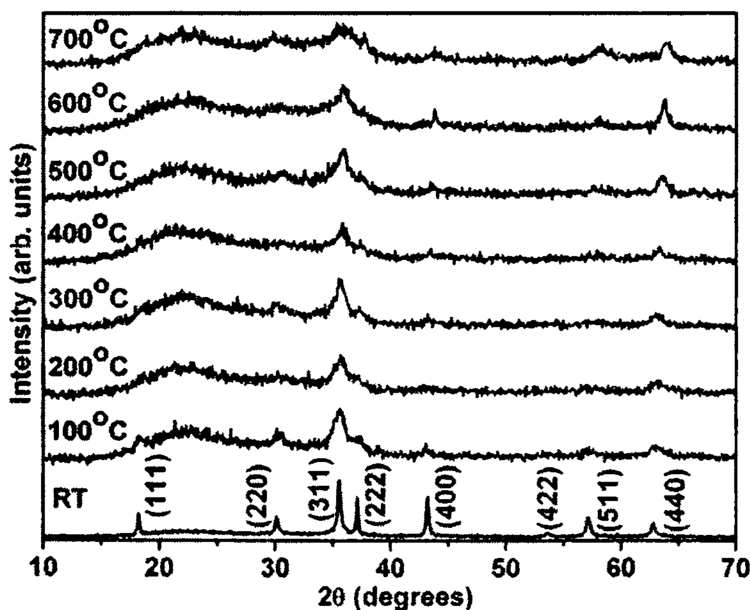

Figure 5.2. XRD patterns of $ZnGa_2O_4:Dy^{3+}$ films on quartz substrates varying the substrate temperature

The variation of FWHM and lattice constant with substrate temperature is shown in figure 5.3. The lattice constant is found to decrease with substrate temperature. As the temperature of the substrate is increased, one should expect

higher vacancy concentration in the deposited films due to the loss of Zn. The subsequent lowering of crystallinity in the films is quite evident from the increase in FWHM with substrate temperature. Minami *et al.* [16] has reported that such reduction in grain size favours the luminance properties in low voltage phosphors because of their large surface area per unit volume.

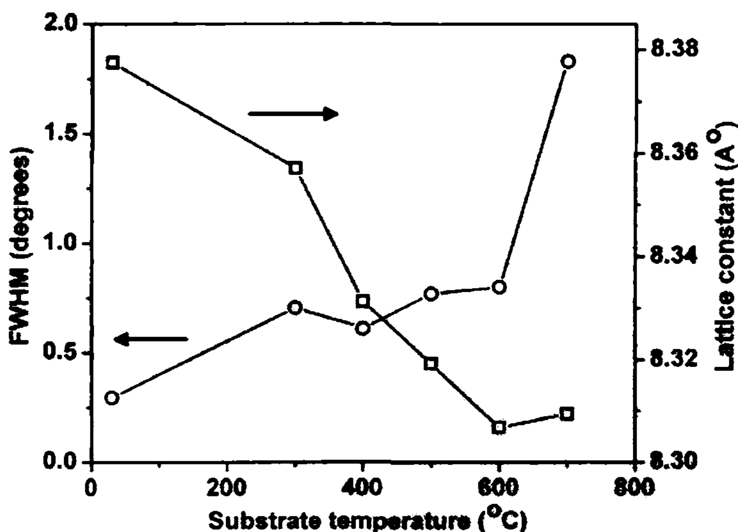

Figure 5.3. Variation of FWHM and lattice constant of $ZnGa_2O_4:Dy^{3+}$ films with substrate temperature

But as the temperature is raised to 700°C, FWHM drastically rises collapsing the crystallinity which in turn is found to affect the luminescent properties adversely. This can also be attributed to the partial formation of the binary compound β-Ga_2O_3 in the film, Zn/Ga ratio being very low as evident from XRF data.

AFM images of films deposited at substrate temperatures 200°C, 400°C and 600°C is shown in figure 5.4. AFM images reveal that the films exhibit a granular shaped microstructure. The surface roughness of the films was found to be highly dependent on the substrate temperature and had a strong effect on the PL response of the films.

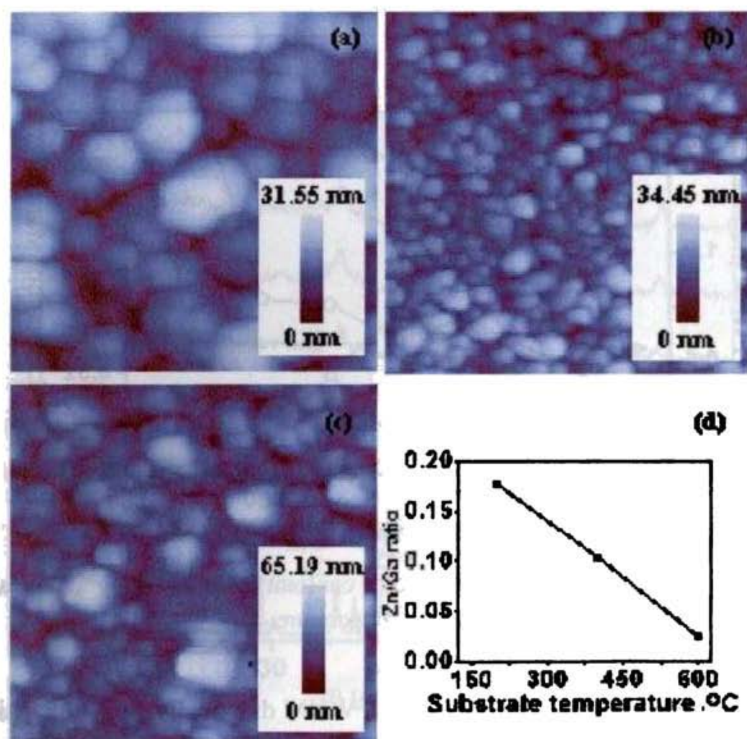

Figure 5.4. AFM images of films deposited at substrate temperatures (a) 200°C, (b) 400°C and (c) 600°C. (d) shows Zn/Ga ratio with substrate temperature

The variation in Zn/Ga ratio of the films with substrate temperature is also shown in figure 5.4. Reduction in Zn/Ga ratio with substrate temperature is due to the re-evaporation of Zn at higher substrate temperatures, vapor pressure of

Zn being higher compared to Ga [17]. Lee *et al.* [18] reported that control of Zn/Ga stoichiometry requires the use of mosaic $ZnGa_2O_4$/ZnO targets to compensate for Zn loss due to evaporation. On the other hand, these excess Ga atoms act as sensitizing sites in the host influencing the luminescent properties positively [19].

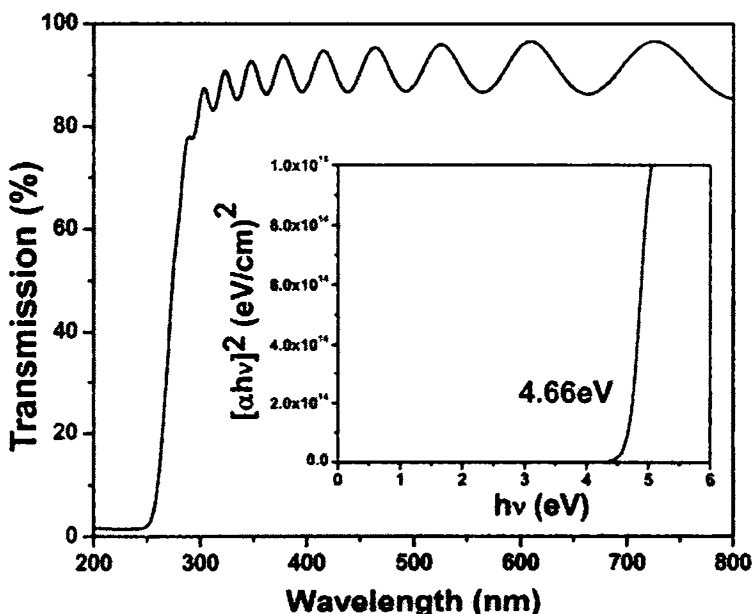

Figure 5.5. Transmission spectrum of $ZnGa_2O_4:Dy^{3+}$ film deposited on quartz substrate at 600°C. Inset shows the Tauc plot for determining band gap

The transmission spectrum of the film coated at a substrate temperature of 600°C is shown in figure 5.5. Almost 90% transparency is observed in the visible region and a strong absorption occurs around the band edge of the host. The band gap of the sample was determined to be 4.66 eV from the $[\alpha h\nu]^2$ versus hν

curve (inset of figure 5.5). All the deposited films exhibited similar characteristics and the band gap values lie in the range 4.4 ± 0.3 eV [20].

Figure 5.6 compares the room temperature photoluminescent emission and excitation spectra of bulk $ZnGa_2O_4$ phosphor and $ZnGa_2O_4:Dy^{3+}$ film deposited at 600°C. The bulk sample exhibits a strong blue emission band peaking at 439 nm attributed to the self-activated transition of regular O_h Ga-O groups [21].

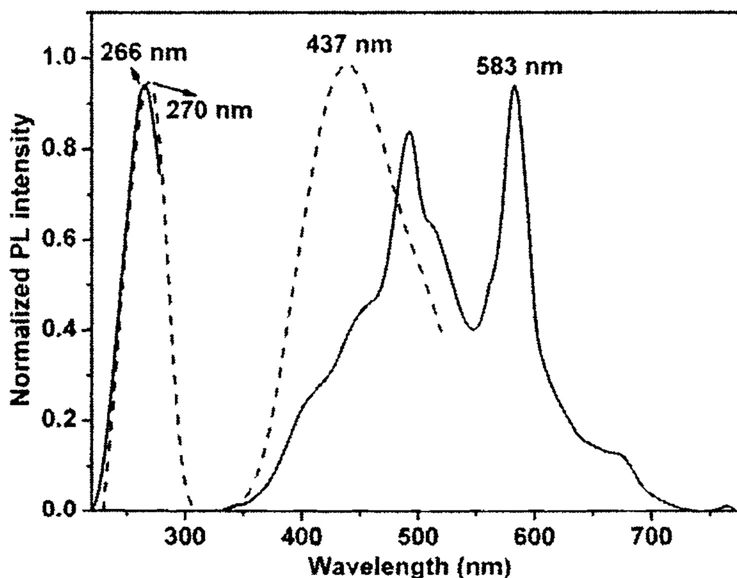

Figure 5.6. PL emission and excitation spectra of bulk $ZnGa_2O_4$ (dotted) [λ_{exc} = 270 nm and λ_{em} = 439 nm] and $ZnGa_2O_4:Dy^{3+}$ film deposited at 600°C (solid) [λ_{exc} = 266 nm and λ_{em} = 583 nm]

The film, on the other hand, exhibits characteristic fluorescence transitions $^4F_{9/2} \rightarrow {}^6H_J$ (J = 15/2, 13/2, 11/2, 9/2) of dopant ions along with a less intense emission band of the host extending from UV to blue. The characteristic lines of

the Dy^{3+} emission spectra, falls in the blue, yellow and red regions of the electromagnetic spectrum with their peak maxima at 494 nm, 583 nm, 676 nm and 765 nm respectively. The dominant emission is the one corresponding to the spectral transition $^4F_{9/2} \rightarrow {}^6H_{13/2}$. The excitation spectrum of the film, recorded at the dominant emission wavelength of 583 nm, gave a broad intense band with a maximum at 266 nm. This was quite similar to the broad band (peak maximum at 270 nm) exhibited by the host excitation spectra recorded at an emission wavelength of 439 nm. Such excellent overlap between the two excitation spectra suggests that the film strongly absorbs at the host band edge [22]. Moreover, the host emission is greatly suppressed in the Dy^{3+} doped film and the fluorescent emission of the dopant is found to dominate the spectrum. All these facts strongly support an efficient nonradiative resonant energy transfer from the host lattice to the dopant ions mediated by exchange interactions in $ZnGa_2O_4:Dy^{3+}$ films (explained in detail in the previous chapter).

The photoluminescent emission spectra of the film deposited at 600°C is compared to that of the target powder in figure 5.7. The luminescent emission from the film had a reduced intensity (for the same slit width) and a larger FWHM than the bulk as expected. Despite having the same spinel structure, the film has a higher vacancy concentration than the powder due to the excess Ga^{3+} content. The effects of vacancy defects, excess Ga^{3+} ions and lower crystallinity would perturb randomly the atomic configuration and the associated crystal field surrounding the Dy^{3+} ions in the film. Consequently, the ground level and the excited level of the optically active electrons in the dopant ions tend to spread leading to the broader emission band in the films [23]. It can be observed that

the crystal field splitting of each of the characteristic transitions of the dopant ion is therefore less prominent in the film than in the bulk.

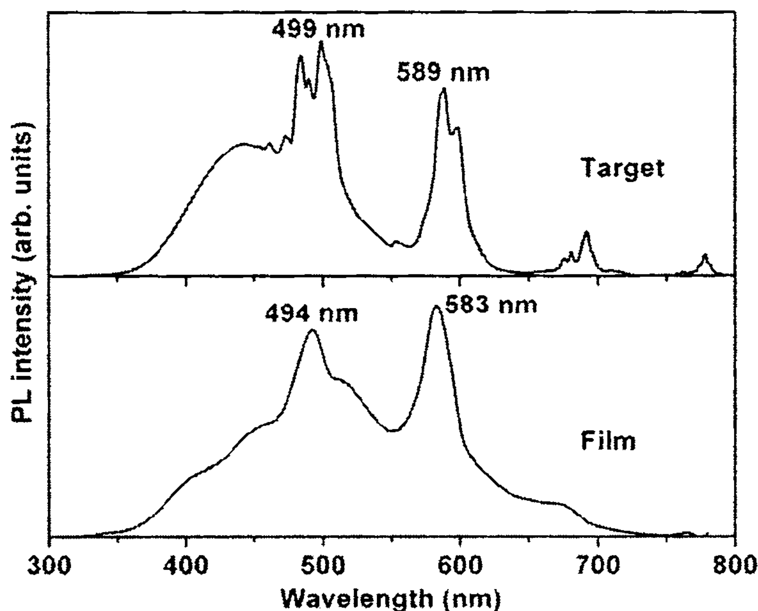

Figure 5.7. PL emission spectra of $ZnGa_{1.95}O_4$:$Dy_{0.05}$ target and sputter deposited film at 600°C

The PL emission spectra of films deposited on quartz substrates at various substrate temperatures is shown in figure 5.8 for an excitation wavelength of 266 nm. No luminescence was exhibited by the film deposited at room temperature. The films deposited at 100°C and 200°C gave extremely weak emissions due to the improper incorporation of the Dy^{3+} ions. However, at and above 300°C, the films exhibited a white emission due to the simultaneous characteristic fluorescence transitions $^4F_{9/2} \rightarrow {}^6H_J$ (J = 15/2, 13/2, 11/2, 9/2) of Dy^{3+} ions along with a less intense emission band of the host. The weak host emission band was

found to blueshift with substrate temperature. This is suggestive of the fact that the substrate heating has resulted in the migration of Ga^{3+} ions to the tetrahedral sites [21] in the Zn deficient films. The PL emission intensity was observed to be a maximum for the substrate temperature of 600°C. The PL intensity of the film deposited at 700°C falls due to the simultaneous effect of reduced crystallinity and low Zn/Ga ratio.

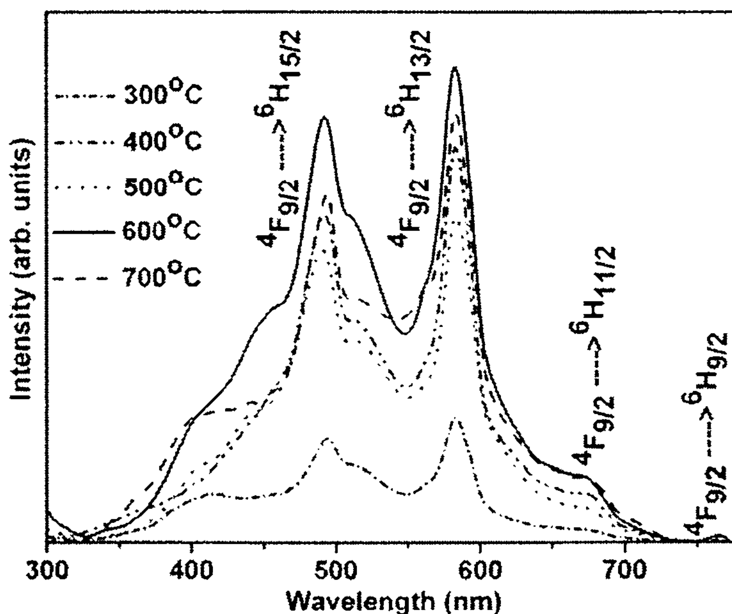

Figure 5.8. PL emission spectra of $ZnGa_2O_4:Dy^{3+}$ films deposited at various substrate temperatures, λ_{exc} = 266 nm

The $^4F_{9/2} \rightarrow {}^6H_{13/2}$ spectral transition is more intense in comparison to $^4F_{9/2} \rightarrow {}^6H_{15/2}$ in the PL emission spectrum of the films. This spectral property of Dy^{3+} provides some information on the site occupation of Dy^{3+} in the host lattice. The $^4F_{9/2} \rightarrow {}^6H_{13/2}$ transition of Dy^{3+} ions is a hypersensitive transition with $\Delta J = 2$

and is strongly influenced by the crystal field environment. The ($^4F_{9/2} \rightarrow {}^6H_{13/2}$) transition becomes dominant in the emission spectrum when Dy^{3+} ions are located at a low symmetry local site (without an inversion symmetry center) [24]. Here, in the host lattice, Zn^{2+} ions occupy tetrahedral sites (T_d point symmetry without inversion center) and Ga^{3+} ions occupy octahedral sites (O_h point symmetry with inversion center). The ionic radii of Zn^{2+}, Ga^{3+} and Dy^{3+} ions for six coordination are respectively 0.074 nm, 0.062 nm and 0.0912nm. But Dy^{3+} ions rarely substitute Zn^{2+} due to charge imbalance.

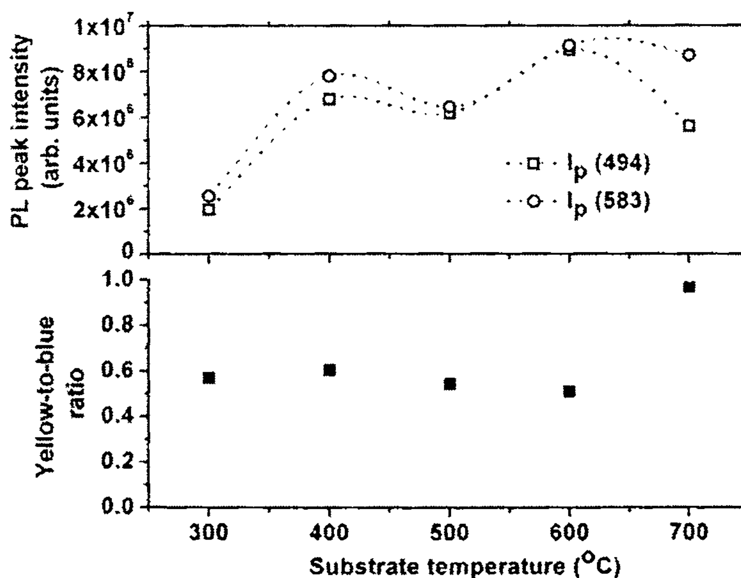

Figure 5.9. Variation of the PL peak intensity and Y/B ratio of the films with substrate temperature

Also, a constant yellow-to-blue (Y/B) intensity ratio [25] (figure 5.9.) of the films is suggestive of the fact that Dy^{3+} replaces Ga^{3+}. Since Zn deficient films are being deposited at high substrate temperatures, Ga^{3+} ions have a strong

tendency to occupy tetrahedral sites [26] or vacant interstitial sites without an inversion centre. The replacement of these Ga^{3+} ions by the dopant Dy^{3+} ions therefore enhances its $^4F_{9/2} \rightarrow {}^6H_{13/2}$ spectral transition. The film deposited at 700°C shows an appreciable deviation in the Y/B ratio. This may be because one cannot totally exclude the possibility of Dy^{3+} ions occupying the abundantly present Zn^{2+} vacancy sites in this film [25]. Figure 5.9 also shows the variation of the PL peak intensity of the films with substrate temperature. It is quite obvious that the peak intensity of $^4F_{9/2} \rightarrow {}^6H_{13/2}$ transition of Dy^{3+} ions is always higher than that of $^4F_{9/2} \rightarrow {}^6H_{15/2}$ fluorescent transition for all the films.

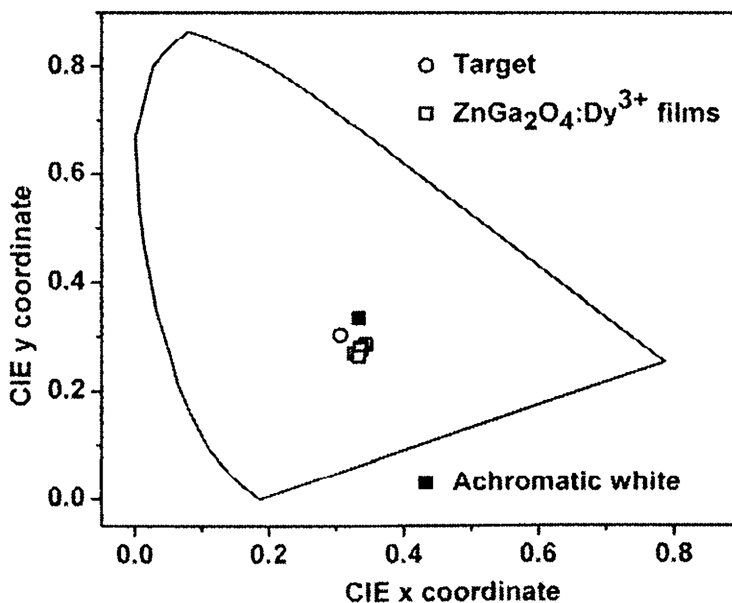

Figure 5.10. CIE color coordinate diagram $ZnGa_2O_4$:Dy^{3+} films, the CIE coordinates of the target used and achromatic white is shown for reference

The quality of the luminescent emissions from the sputter deposited films was gauged using CIE (Commission Internationale d'Eclairage) 1931 coordinates. The CIE coordinates of all the films deposited at various substrate temperatures lie in and around the position of achromatic white in the coordinate diagram (figure 5.10). The CIE chromaticity coordinates of the film deposited at 600°C, which gives the maximum PL emission intensity, was determined to be (x, y) = (0.34, 0.28). The chromaticity coordinates of the $ZnGa_{1.95}O_4:Dy_{0.05}$ powder target with 2.5 atomic % Dy content was found to be (0.31, 0.3). Table 5.1 gives the chromaticity coordinates of the target and the deposited films.

Sample	Substrate temperature (°C)	CIE chromaticity coordinates (x, y)
$ZnGa_{1.95}O_4:Dy_{0.05}$	-	(0.31, 0.3)
Films	300	(0.33, 0.27)
	400	(0.34, 0.29)
	500	(0.34, 0.28)
	600	(0.34, 0.28)
	700	(0.33, 0.26)

Table 5.1. CIE chromaticity coordinates of the target and the sputter deposited $ZnGa_2O_4:Dy^{3+}$ films

5.4. Conclusions

$ZnGa_2O_4:Dy^{3+}$ phosphor thin films were deposited on amorphous quartz substrates by radio frequency magnetron sputtering and the effect of substrate

temperature on its structural and luminescent properties were investigated. Polycrystalline films could be deposited even at room temperature. The crystalline behavior, Zn/Ga ratio and surface morphology of the films were found to be highly sensitive to substrate temperature. No luminescence was observed for the as-deposited film at room temperature that exhibited spinel phase growth. But the films deposited at and above a substrate temperature of 300°C exhibited white luminescence under UV illumination even without any post-deposition annealing treatments. The photoluminescent (PL) emission can be attributed to the combined effect of multicolor emissions from the single luminescence center Dy^{3+} via host sensitization. Maximum PL emission intensity was observed for the film deposited at 600°C, the CIE chromaticity coordinates of the emission determined to be (x, y) = (0.34, 0.28). $ZnGa_2O_4:Dy^{3+}$ can therefore act as an active layer in ACTFEL displays. The work also suggests the use of low temperature substrates other than the conventional ceramic substrates for device fabrication.

References

1. S. S. Yi, I. W. Kim, H. L. Park, J. S. Bae, B. K. Moon and J. H. Jeong, *J. Cryst. Growth*, **247**, 213 (2003).
2. S. H. Yang, *J. Electron. Mater.*, **33**, L1 (2004).
3. S. S. Yi, J. S. Bae, K. S. Shim, J. H. Jeong, H. L. Park and P. H. Holloway, *J. Cryst. Growth*, **259**, 95 (2003).
4. J. S. Bae, Y. H. Kim, J. K. Jang, K. S. Shim, J. K. Lee, J. H. Jeong, S. S. Yi and H. L. Park, *Appl. Phys. A*, **78**, 1073 (2004).

5. Y. E. Lee, D. P. Norton and J. D. Budai, *Appl. Phys. Lett.*, **74**, 3155 (1999).
6. S. H. Yang, T. J. Hsueh and S. J. Chang, *Jpn. J. Appl. Phys.*, **46**, 4166 (2007).
7. J. H. Kim and P. H. Holloway, *J. Appl. Phys.*, **95**, 4787 (2004).
8. M. Flynn and A. H. Kitai, *J. Electrochem. Soc.*, **148**, H149 (2001).
9. T. Minami, T. Maeno, Y. Kuroi and S. Takata, *Jpn. J. Appl. Phys.*, **34**, L684 (1995).
10. M. Flynn and A. H. Kitai, *J. Appl. Phys.*, **97**, 094502 (2005).
11. T. Minami, H. Toda and T. Miyata, *J. Vac. Sci Technol. A*, **19**, 1742 (2001).
12. A. R. Phani, S. Santucci, S. Dinardo, L. Lozzi, M. Passacantando, P. Picozzi and C. Cantalini, *J. Mater. Sci.*, **33**, 3969 (1998).
13. JCPDS Card No. 38-1240.
14. Y. E. Lee, D. P. Norton, C. Park and C. M. Rouleau, *J. Appl. Phys.*, **89**, 1653 (2001).
15. Y. J Kim, Y. H. Jeong, K. D. Kim, S. G. Kang, K. G. Lee, J. I. Han, Y. K. Park and K. I. Cho, *J. Vac. Sci. Technol. B*, **16**, 1239 (1998).
16. T. Minami, Y. Kuroi and S. Takata, *J. Vac. Sci. Technol. A*, **14**, 1736 (1996).
17. P. D. Rack, J. J. Peterson and M. D. Potter, *J. Mater. Res.* **16**, 1429 (2001).
18. Y. E. Lee, D. P. Norton, J. D. Budai, C. M. Rouleau and J. W. Park, *J. Electroceram.* **4**, 293 (2000).
19. I. J. Hsieh, M. S. Feng, K. T. Kuo and P. Lin, *J. Electrochem. Soc.*, **141**, 1617 (1994).
20. S. Itoh, H. Toki, Y. Sato, K. Morimoto and T. Kishino, *J. Electrochem. Soc.*, **138**, 1509 (1991).
21. I. K. Jeong, H. L. Park and S. Mho, *Solid State Commun.*, **105**, 179 (1998).

22. Z. Xu, Y. Li, Z. Liu and D. Wang, *J. Alloys Compd.* **391**, 202 (2005).
23. C. F. Yu and P. Lin, *Jpn. J. Appl. Phys.*, **35**, 5726 (1996).
24. M. L. Pang, W. Y. Shen and J. Lin, *J. Appl. Phys.* **97**, 033511 (2005).
25. Q. Su, Z. Pei, L. Chi, H. Zhang, Z. Zhang and F. Zou, *J. Alloys Compd.*, **192**, 25 (1993).
26. J. B. Gruber, B. Zandi, U. V. Valiev and Sh. A. Rakhimov, *J. Appl. Phys.* **94**, 1030 (2003).

Chapter 6

Fabrication of $ZnGa_2O_4:Dy^{3+}$ active ACTFEL devices on glass substrate

6.1. Introduction

Many binary and ternary sulphides have been identified that can serve as the light emitting layers of alternating current thin film electroluminescent (ACTFEL) displays [1-6]. High luminance blue [7], red [8-10], green [11-14] and yellow [15, 16] oxide phosphors, superior to the hygroscopic sulfides in terms of chemical stability, have also been reported as efficient active layers of monochrome TFEL displays. Even high luminance multicolor emitting TFEL devices have been fabricated using multicomponent oxide phosphor systems [17-21]. But commercialization of oxide phosphor electroluminescence for flat panel displays on glass substrates requires the deposition of phosphors at temperatures 700°C or lower.

Spinel $ZnGa_2O_4$ serves as an excellent host for activator incorporation and hence has excellent potential to be a vital part in future display systems [22]. Till date, high luminance green emitting TFEL devices have been reported [23-27] with efficiencies approaching 1 lm/W. These devices were fabricated by depositing the active $ZnGa_2O_4:Mn^{2+}$ emitting layers onto thick ceramic sheets of $BaTiO_3$ using rf magnetron sputtering accompanied by high temperature post-annealing treatments.

In the present work, white light generating ACTFEL devices were fabricated using $ZnGa_2O_4:Dy^{3+}$ as the active emitting layer on low temperature glass substrates without any post-deposition treatments. Such white light emitting electroluminescent displays using singly activated single phased phosphor layers

has the advantage of maintaining the simple device fabrication sequence of a monochrome TFEL display and producing full color flat panel displays using filters of the three primary colors. The effect of the presence of a ZnO buffer layer in between the substrate and the active layer on device performance has also been discussed.

6.2. Experimental

TFEL devices were fabricated using an asymmetric standard double insulating structure as shown in figure 6.1. Every layer, except for the thermally evaporated rear electrode, of the metal-insulator-semiconductor-insulator-metal (MISIM) structure was an oxide material.

Commercially available transparent ITO/ATO coated nippon electric glass (NEG) substrates (Planar Systems of Beaverton, Oregon) served as the platform for device fabrication. The transparent ITO (indium tin oxide) and ATO (aluminium titanium oxide) layers constituted the bottom electrode and bottom dielectric of the EL device. The ATO insulator layer is engineered such that the high dielectric constant of the TiO_2 and the large band gap (low leakage) of the Al_2O_3 suitably combines to form a very low leakage insulator layer with a moderate relative dielectric constant (ε_r = 10-12). The substrates of dimension 1"x1" was placed 4.5 cm away from the powder targets for sputter depositing uniform transparent layers of the active phosphor material $ZnGa_2O_4:Dy^{3+}$ and the top dielectric material $BaTa_2O_6$ (barium tantalate, BTO).

The $ZnGa_2O_4:Dy^{3+}$ powder target was synthesized in the laboratory by the conventional high temperature solid state reaction. Stoichiometric amounts of the starting materials, namely ZnO (99.99%, Alfa Aesar), Ga_2O_3 (99.99%, Alfa Aesar) and Dy_2O_3 (99.99%, Indian Rare Earths Ltd.), were hand mixed in ethanol medium and subsequently fired at 1350°C for 12 hours in air. The doping concentration of Dy^{3+} was fixed at 2.5 at. %.

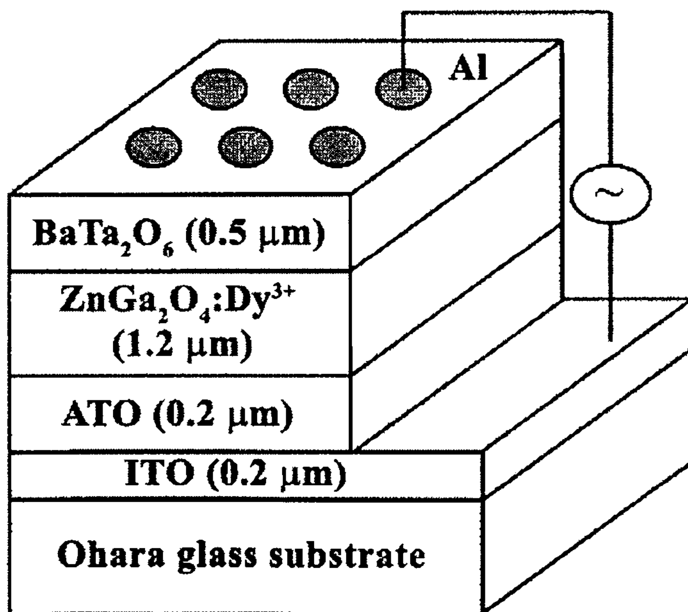

Figure 6.1. Schematic view of the fabricated TFEL structure

A powder target of $BaTa_2O_6$ (99%, Alfa Aesar) was used to sputter deposit the top dielectric layer. Table 6.1 specifies the sputtering conditions of each of these layers.

Target	Calcined $ZnGa_2O_4:Dy^{3+}$ powder	Barium Tantalate powder	ZnO powder
Target to substrate distance (cm)	4.5	6	4.5
Base Pressure (mbar)	$6*10^{-6}$	$6*10^{-6}$	$6*10^{-6}$
Ambient gas	Ar	Ar	Ar
Working pressure (mbar)	0.015	0.01	0.01
RF power (W)	125	100	100
Substrate temperature (°C)	600	RT	RT
Duration of deposition (hrs)	2	2	1/4
Thickness (μm)	~ 1	~ 0.5	~ 0.15

Table 6.1. Conditions for sputter depositing the active phosphor layer, the top dielectric layer and the ZnO layer on the NEG/ITO/ATO substrate

To complete the MISIM structure, aluminum (Al) dots, 3 mm in diameter and 100 nm in thickness, were thermally evaporated onto the top of the $BaTa_2O_6$ insulating layer to serve as the rear opaque electrode. Al serves here not only as a top electrode but also as an optical reflector. The EL emission is out coupled from the substrate side of the standard device structure.

Devices were also fabricated by inserting a ZnO buffer layer in between the substrate and the phosphor layer. A powder target of ZnO (99.99%, Alfa Aesar) was used to sputter deposit the buffer layer. Table 6.1 specifies the sputtering conditions of the same.

A Rigaku x-ray diffractometer with Cu K_α radiation was used for structural characterization. The device was electrically excited using a 1.5 KHz trapezoidal waveform generated from a pulsed signal generator (Digilog Instruments Ltd.). The bipolar pulse train driving the device had a characteristic rise and fall time of 30 μs each and a stay time of 70 μs. A 0.32 m monochromator (Triax-320) coupled with Hamamatsu R928 photomultiplier tube was used to record the electroluminescent output from the fabricated device.

6.3. Results and discussion

X-ray diffraction pattern of the as-deposited $ZnGa_2O_4$:Dy^{3+} phosphor film on the polycrystalline NEG/ITO/ATO substrate at a temperature of 600°C, in comparison to that of the substrate, is shown in figure 6.2. The diffraction pattern of the substrate comprises of the polycrystalline ITO layer only and no peaks are possible from either amorphous glass or amorphous ATO. The as-deposited film has crystallized in the cubic spinel structure and exhibits the spinel peaks - (311), (400) and (440) - of the host. Broadening of these peaks reveals the reduced crystalline nature of the deposited film, mainly attributed to the Zn deficiency at the chosen substrate temperature. The peaks corresponding to that of the substrate (denoted by asterisks) has reduced very much in intensity

because only weaker x-rays can be detected from the underlying layers due to the presence of the film layer of thickness above 1 micron over the substrate.

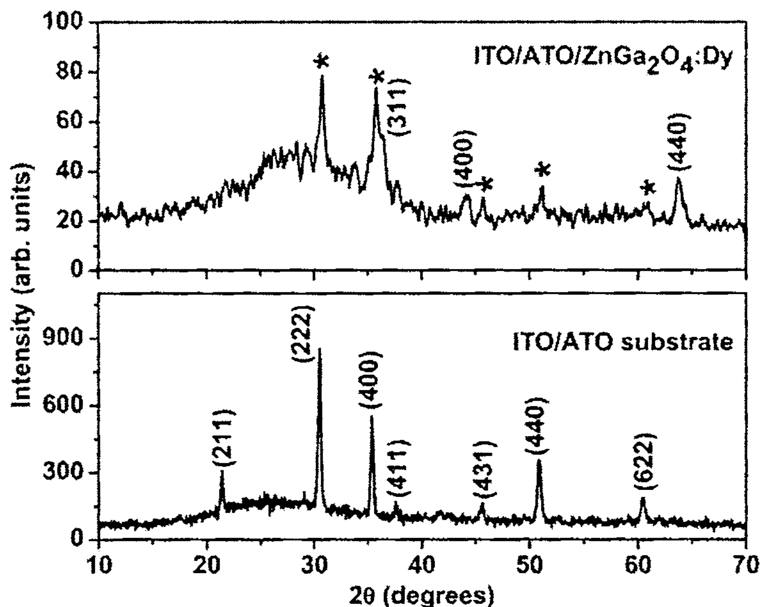

Figure 6.2. XRD pattern of the $ZnGa_2O_4:Dy^{3+}$ film deposited on NEG/ITO/ATO substrate at 600°C, the asterisk denotes the peaks of the substrate and the diffraction pattern of the substrate is shown for comparison

XRD pattern of BTO film deposited on glass substrate at room temperature is shown in figure 6.3. This specific material was chosen as the top insulator since it has a high dielectric constant (ε_r = 20) for good charge coupling to the phosphor layer, low leakage for good power efficiency, and a high breakdown field (F_{BD} = 3.5 MV/cm) to support ACTFEL operation. Additionally, BTO can be deposited without substrate heating and is amorphous [28], as is obtained in the present work. Moreover, this dielectric material possesses a self-healing propagation mode that shall reduce the possibilities of device breakdown [29].

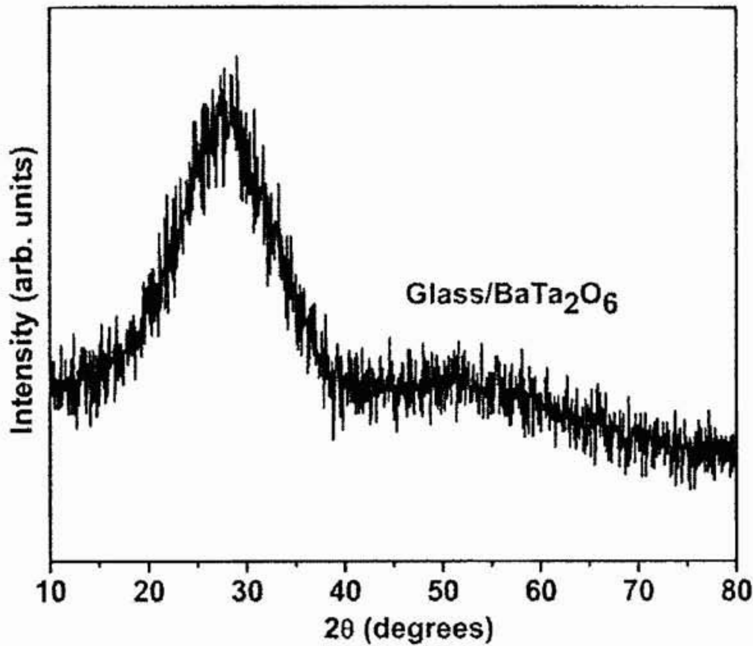

Figure 6.3. XRD pattern of the $BaTa_2O_6$ film deposited on glass substrate at room temperature, the diffraction pattern of BTO powder target is shown below

6.3.1. Glass/ITO/ATO/ $ZnGa_2O_4:Dy^{3+}$/BTO/Al TFEL device

The luminance-voltage (L-V) curve of the MISIM structured ACTFEL device NEG/ITO/ATO/$ZnGa_2O_4:Dy^{3+}$/BTO/Al (device A) is shown in figure 6.4 for the drive frequency 1.5 KHz. The dependence of luminance on the applied ac voltage across the device is related by a formula,

$$L = L_0 \exp\left(-\left(\frac{V_0}{V}\right)^{-\frac{1}{2}}\right), \qquad (6.1.)$$

where L is the luminance, V is the applied voltage and L_o and V_o are constants determined by the phosphor material, device structure and exciting condition [30, 31]. A semilog plot of the square root of the voltage dependence upon luminance is shown in the inset of figure 6.4. The linearity of the semilog curve reveals that the device satisfies the exponential luminance voltage relation, which inturn asserts that the mechanism of electroluminescence is through impact ionization.

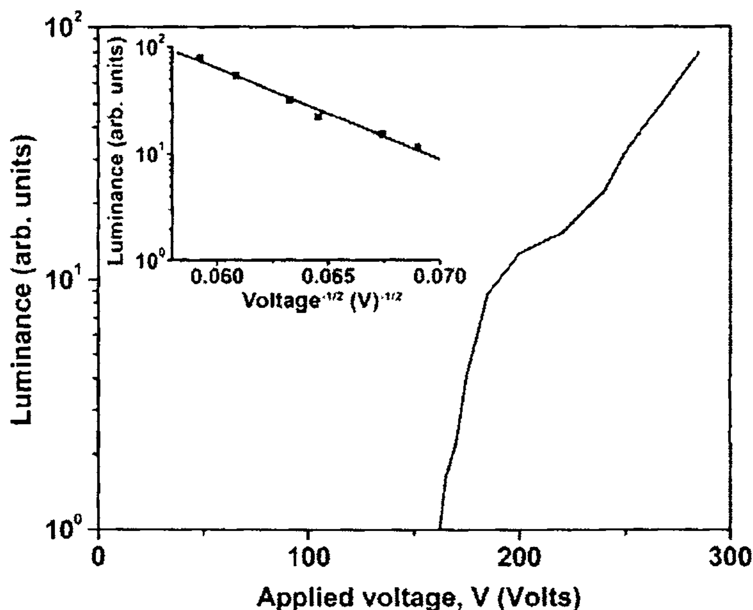

Figur 6.4. Luminance-voltage curve of Device A at 1.5 KHz, a semilog plot between luminance and $V^{-1/2}$ is shown in the inset

Direct impact excitation of luminescent centers by hot electrons is widely accepted to be the dominant excitation mechanism in most TFEL devices. Probe layer experiments on EL excitation mechanism in ACTFEL devices by Marello

et al. [32] suggested that the excitation need not be only via hot electron impact. Okamoto *et al.* [33] also gives further evidence of a host to activator resonant energy transfer to be the cause of EL emissions in Tb activated ZnS phosphors. So EL emission from $ZnGa_2O_4:Dy^{3+}$ active phosphor layer may be the result of a two stage process or a direct impact excitation process. In the former case, on applying an electric field above the threshold value, the electrons, tunnel injected into the phosphor layer from the phosphor/insulator interface on the cathode side, impact ionizes the abundant Ga^{3+} ions present in the active layer. The energy transferred to the host lattice by hot carrier collisions is then nonradiatively resonant transferred to the dopant Dy^{3+} ions and the excitation and de-excitation at these luminescent centers results in EL emission. One cannot rule out the possibility of luminescence by direct impact excitation and subsequent de-excitation in Dy^{3+} centers. To distinguish whether the excitation is due to energy transfer or via direct impact by hot electrons, a probe of pulse width less than that of life time of broad host emission band is required [33]. On using a wider pulse, the energy transfer would already have been completed by the time the excitation pulse is removed so that the delay in the activator emission intensity cannot be observed.

The room temperature EL emission spectrum of the as-deposited device A is shown in figure 6.5. The curves for applied voltages, V, in the range 185 to 285 V has been shown at the drive frequency 1.5 KHz. The emission spectra exhibits the characteristic fluorescence transitions $^4F_{9/2} \rightarrow {}^6H_J$ (J = 15/2, 13/2, 11/2, 9/2) of the dopant ions. The characteristic lines of the Dy^{3+} emission falls in the blue, yellow and red regions of the electromagnetic spectrum with their maxima at

491 nm, 581 nm, 676 nm and 764 nm respectively. The simultaneous occurrence of multicolor emissions has rendered whiteness to the EL output.

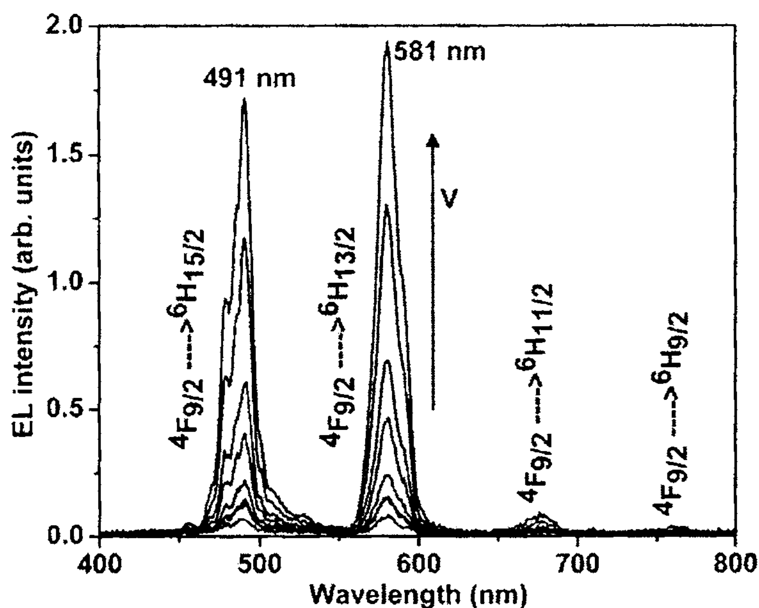

Figure 6.5. EL emission spectrum of $ZnGa_2O_4:Dy^{3+}$ active ACTFEL device at a drive frequency 1.5 KHz for applied voltage V in the range 185 to 285 V

With increase in applied voltage across the device, the intensity of the EL emission improves without any shift in the position of the emission peaks. This implies that Dy^{3+} ions have been uniformly incorporated into the $ZnGa_2O_4$ host [34]. Among the fluorescent emissions of the dopant ion, the $^4F_{9/2} \rightarrow {}^6H_{13/2}$ spectral transition is more intense in the EL output for all applied voltages. The hypersensitive $^4F_{9/2} \rightarrow {}^6H_{13/2}$ transition becomes dominant when Dy^{3+} ions replace Ga^{3+} ions that have a strong tendency to occupy tetrahedral sites [35] or vacant interstitial sites without an inversion centre [36] in the Zn deficient film

deposited at the chosen high substrate temperature. Also, one cannot totally exclude the possibility of Dy^{3+} ions occupying the abundantly present Zn^{2+} vacancy sites in this film.

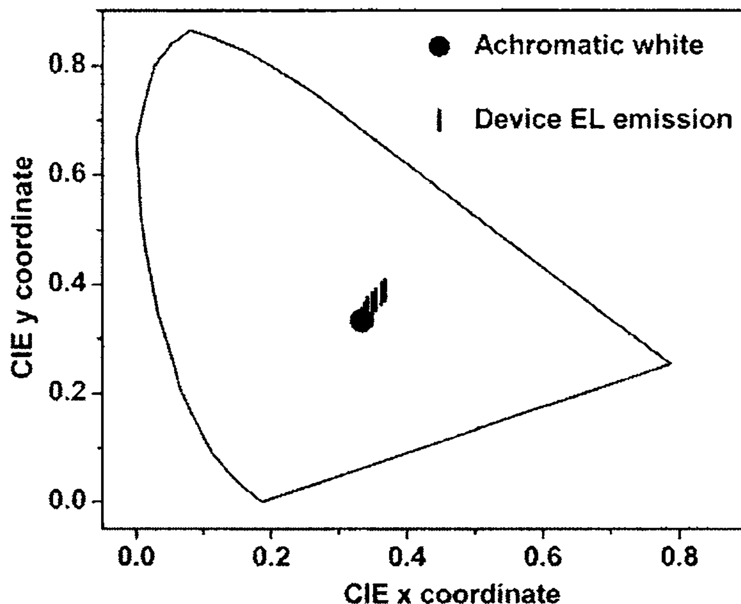

Figure 6.6. Color coordinate diagram plotting the CIE coordinates of the EL emissions from device A at various applied voltages

The step observed in the L-V curve (figure 6.4) is significant of the generation of a positive space charge within the phosphor layer [37]. This is presumed to result from band-to-band impact ionization or trap-to-band impact ionization. In the present case, the presence of trap centers can be attributed to (a) the valence mismatch between Dy^{3+} and Zn^{2+} and (b) the presence of vacancies and other point defects in the as-deposited film. Since Zn has a higher vapor pressure than

Ga [38], there is more chance for Zn vacancies to be created at the processed substrate temperature.

The quality of the electroluminescent emissions was gauged using CIE (Commission Internationale d'Eclairage) 1931 coordinates. The CIE coordinates corresponding to the EL emissions, for various voltages applied across the device, lie in and around the position of achromatic white in the coordinate diagram (figure 6.6).

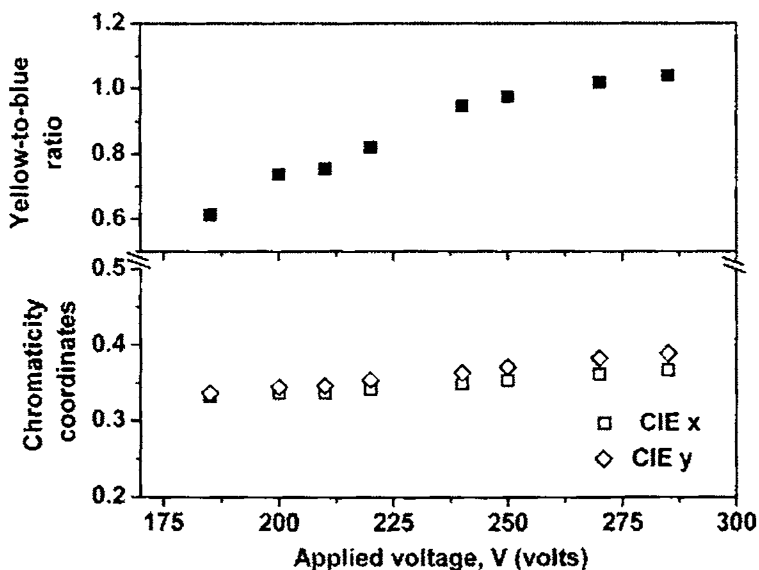

Figure 6.7. Variation in the CIE coordinates (x and y) and Y/B ratio of the EL emissions from Device A at various applied voltages

The variation in the chromaticity coordinates and the yellow-to-blue (Y/B) intensity ratio of the device for various applied voltages has been plotted in figure 6.7. The chromaticity coordinates of the emission ranges from (0.33, 0.34)

at 185 V to (0.37, 0.39) at 285 V. It is observed that the CIE x and y coordinates vary little with increase in applied voltage. That is, the EL output is independent of variations in the applied voltage and this assures color stability [39]. It was also observed that the EL output turns more yellowish with increase in applied voltage as evident from the increase in Y/B ratio from 0.61 to 1.04 with V.

6.3.2. Glass/ITO/ATO/ZnO/$ZnGa_2O_4:Dy^{3+}$/BTO/Al TFEL device

The luminescent properties of oxide thin-film phosphors can further be enhanced by improving the crystalline quality via high temperature post-annealing [40] or by increasing light scattering centers and reducing pinhole defects via surface modification [41]. The inferior crystallinity of as-deposited polycrystalline thin film phosphors are mostly due to limitations of the substrate which is usually an amorphous-like transparent conducting electrode, indium tin oxide (ITO), or various insulating layers on glass. Reducing the defect density by high temperature post-annealing processes is but tedious due to low softening temperature of the glass substrate.

Another possible method of obtaining polycrystalline thin film phosphors with enhanced crystallinity is by depositing a highly crystallized buffer layer onto the amorphous-like substrate. ZnO is chosen here as the buffer layer material as it is relatively easy to obtain high quality polycrystalline films by any conventional technique. Several groups have studied the effects of inserting a ZnO buffer layer in between the thin film phosphor material and ITO coated glass substrates [42, 43].

A device was fabricated (device B) with ZnO buffer layer inserted between the active phosphor layer and the substrate. The MISIM structure of the device was NEG/ITO/ATO/ZnO/$ZnGa_2O_4$:Dy^{3+}/BTO/Al.

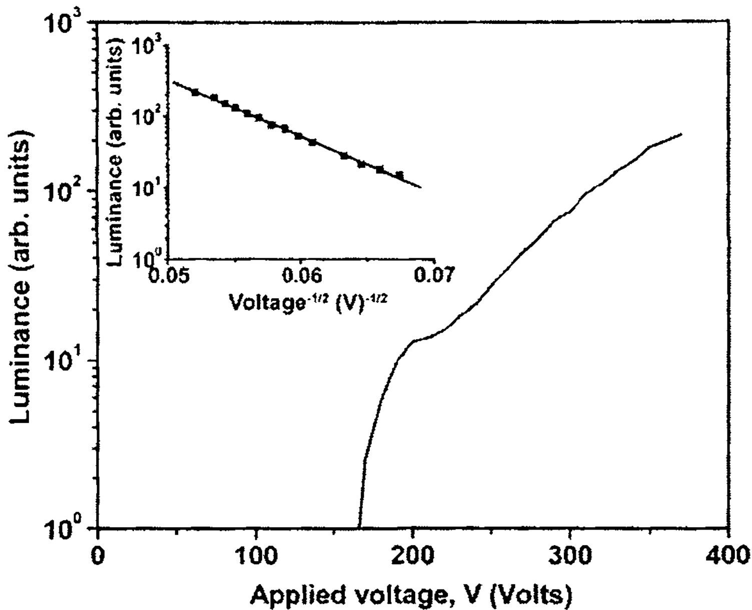

Figur 6.8. Luminance-voltage curve of device B driven at 1.5 KHz, the semilog plot between luminance and $V^{-1/2}$ is shown in the inset

The L-V curve of the device driven by a trapezoidal pulse at 1.5 KHz is shown in figure 6.8. The linearity of the semilog curve, plotted between luminance and $V^{-1/2}$ (inset of figure 6.8), reveals that the device satisfies the exponential luminance voltage relation. The step in the L-V curve denotes the generation of a positive space charge within the active layer. The behavior of the L-V curves is similar to that before the insertion of the buffer layer.

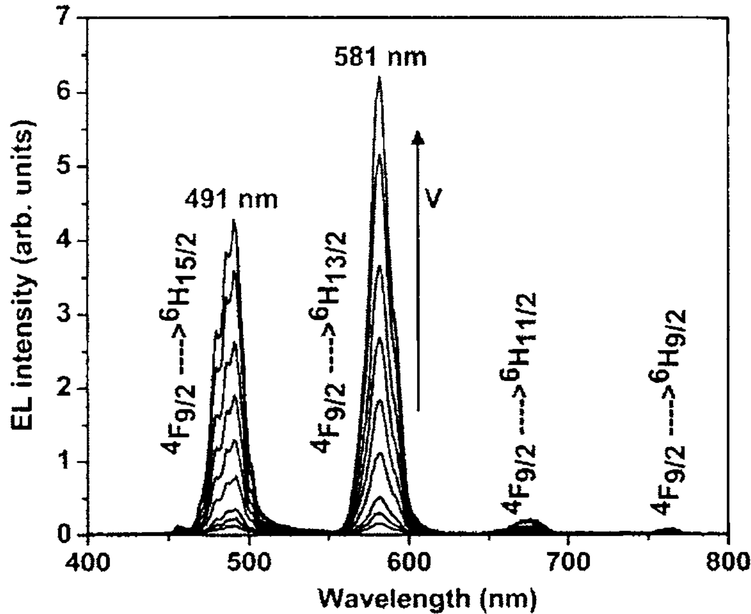

Figure 6.9. EL emission spectrum of device B at the drive frequency 1.5 KHz for applied voltage V in the range 200 to 370 V

The room temperature EL emission spectrum of the as-deposited device B driven at 1.5 KHz is shown in figure 6.9. The emission spectra, has been shown for applied voltages, V, in the range 200 to 370 V. The EL output includes the Dy^{3+} characteristic lines, as expected, in the visible region. The simultaneous presence of the multicolor characteristic fluorescence transitions $^4F_{9/2} \rightarrow {}^6H_J$ (J = 15/2, 13/2, 11/2, 9/2) of the dopant ion renders whiteness to the luminescent output. The hypersensitive $^4F_{9/2} \rightarrow {}^6H_{13/2}$ spectral transition is more intense in the EL output for all applied voltages, as observed for the device without the buffer layer. The position of the emission peaks was insensitive to the variations in

applied voltage. But the EL intensity increased with increase in applied voltage. This supports the uniform incorporation of the dopant in the active layer.

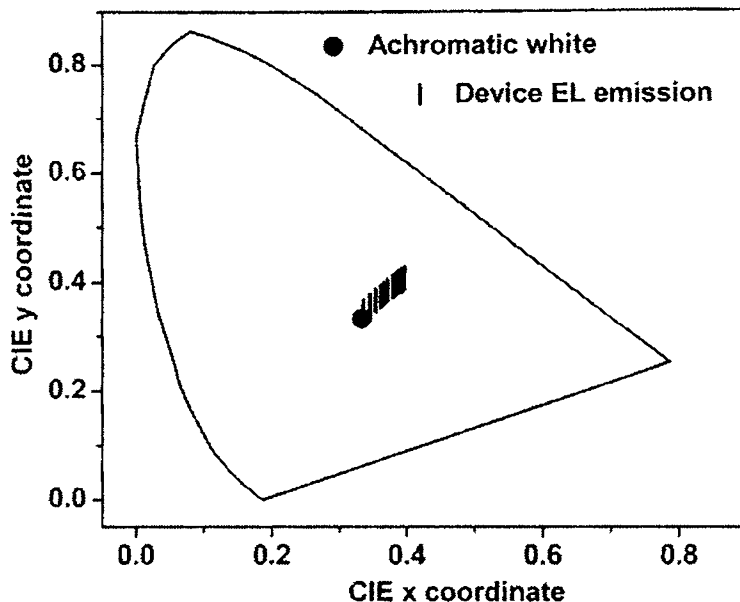

Figure 6.10. Color coordinate diagram plotting the CIE coordinates of the EL emissions from device B at various applied voltages

The EL emissions from device B for various applied voltages were quantified using color coordinates; the CIE chromaticity diagram is shown in figure 6.10. The chromaticity coordinates of the emission ranges from (0.34, 0.35) at 200 V to (0.4, 0.41) at 370 V. The CIE coordinates corresponding to the EL emissions, for various voltages applied across the device, lie in and around the position of achromatic white in the coordinate diagram. Figure 6.11 gives the variation in the chromaticity coordinates and Y/B ratio of device B for various applied voltages.

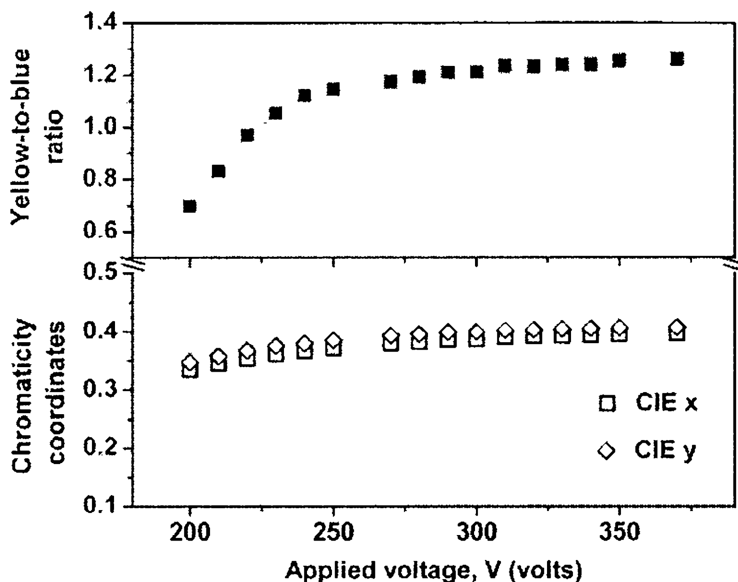

Figure 6.11. Variation in the CIE coordinates (x and y) and Y/B ratio of the EL emissions from device B at various applied voltages

Color stability is ensured over a wider range of the applied voltage when a ZnO layer is inserted between the active layer and the substrate. Yellowishness in the EL emission is found to improve with applied voltage, as evident from the increase in the ratio from 0.7 to 1.26.

6.3.3. Effect of the presence of the ZnO interfacial layer

The presence of the ZnO buffer layer has inturn improved the performance of device B. It was observed that device B could withstand the applied electric field over a wider range (upto 370 V) without breakdown, when compared to device A (upto 285 V). Morever, the intensity of the EL output has very much increased

in device B than device A, as evident from figure 6.12. Device A couldn't withstand voltages above 285 V due to melting of the Al dots [34]. The melting point of Al is 660°C. The local temperature of the device could be much higher at the high frequency of the drive voltage like 1.5 KHz. Melting of the metallic electrode was indicative of the fact that the device would breakdown on increasing the applied voltage further.

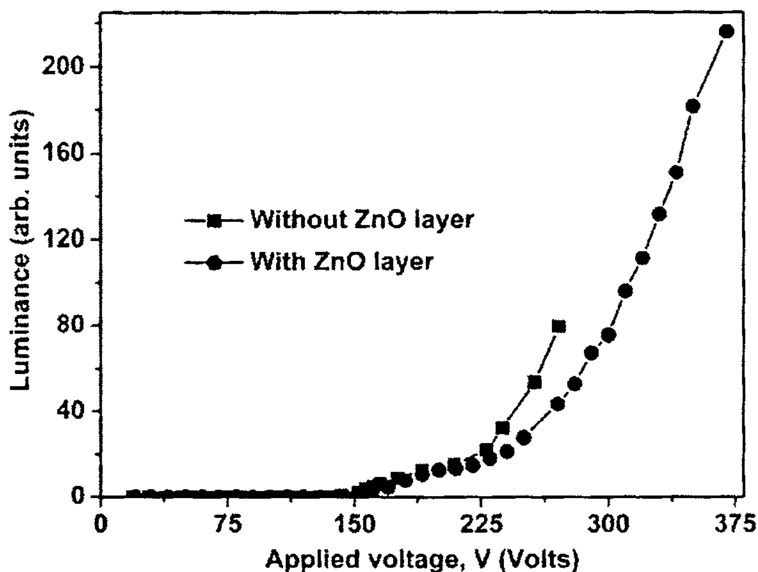

Figure 6.12. Comparison between luminance-voltage curves of device A and B

The surface modification, via the presence of the ZnO buffer layer, might have reduced the density of pinhole defects in the active layer, thereby minimizing the amount of leakage currents and subsequently improving the device performance. But it is observed that for the same applied voltage, device A gives a better output than device B in its operating range. This is because at a fixed V, some

voltage might be dropped across the buffer layer, thereby reducing the electric field across the active layer. That is, ZnO layer acts as a better interfacial layer and not as a charge accelerating layer. However, the presence of the space charge has reduced the increase in the threshold voltage, usually observed with insertion of the buffer layer [44]. The slope of the L-V curves is found to reduce with the insertion of the ZnO layer for device B.

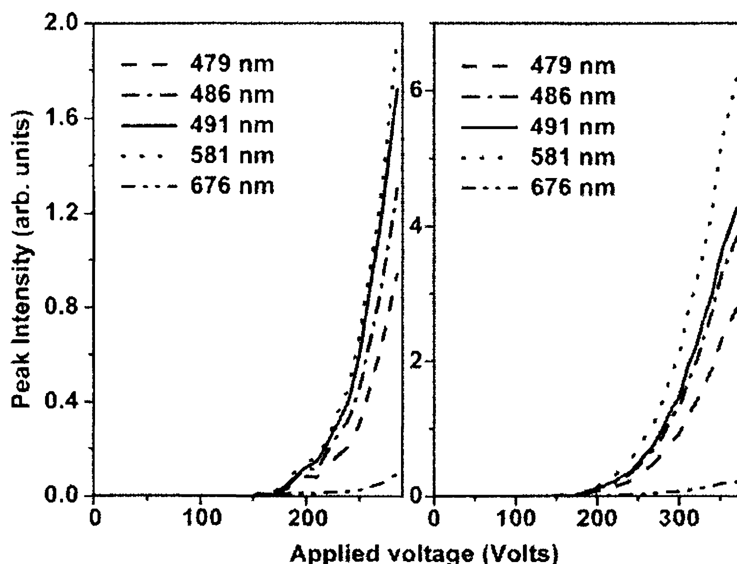

Figure 6.13. Comparison between EL peak intensity versus applied voltage for various emission lines of device A (left) and B (right)

A comparison between the EL peak intensity of various emission lines in the EL spectra with variations in applied voltage has been shown for both cases in figure 6.13. Every characteristic dopant transition had a different emission threshold as a function of voltage [9]. The 581 nm line was found to have the

lower threshold and higher slope as compared to the other observed emission lines.

6.4. Conclusion

An ACTFEL device could be fabricated on glass substrate in the standard MISIM structure - NEG/ITO/ATO/phosphor layer/BTO/Al. Devices were fabricated with and without a ZnO buffer layer. EL emission could be observed even without post-deposition annealing. The white emission results from the simultaneous occurrence of multicolor transitions characteristic of the dopant ion. The L-V curves measured for a drive frequency of 1.5 KHz obeyed the exponential luminance-voltage relation. The step in the L-V curves denotes the generation of space charge within the active layer. The device performance improved on introducing a highly crystallized ZnO buffer layer between the phosphor layer and the substrate. The better interface reduces the density of undesirable microstructural features, such as point defects, grain boundaries, strain, etc., related to nonradiative centers and thereby improves the luminescent output. The luminescence characteristics have to be much improved to find application in TFEL devices. However, the white emission and low processing temperature makes this phosphor suitable for FPD applications.

References

1. N. Miura, T. Ishikawa, T. Sasaki, T. Oka, H. Ohata, H. Matsumoto and R. Nakano, *Jpn. J, Appl. Phys.*, **31**, L46 (1992).

2. S. S. Sun, R. T. Tuenge, J. Kane and M. Ling, *J. Electrochem. Soc.*, **141**, 2877 (1994).
3. M. J. Russ and D. I. Kennedy, *J. Electrochem. Soc.*, **114**, 1066 (1967).
4. T. Ogura, A. Mikami, K. Tanaka, K. Taniguchi, M. Yoshida and S. Nakajima, *Appl. Phys. Lett.*, **48**, 1570 (1986).
5. K. Hirabayashi, H. Kozawaguchi and B. Tsujiyama, *Jpn. J. Appl. Phys.*, **26**, 1472 (1987).
6. K. Ohmi, S. Tanaka, H. Kobayashi and T. Nire, *Jpn. J. Appl. Phys.*, **31**, L1366 (1992).
7. X. Ouyang, A. H. Kitai and T. Xiao, *J. Appl. Phys.*, **79**, 3229 (1996).
8. P. Wellenius, A. Suresh and J. F. Muth, *Appl. Phys. Lett.*, **92**, 021111 (2008).
9. P. Wellenius, A. Suresh, J. V. Foreman, H. O. Everitt and J. F. Muth, *Mater. Sci. Eng. B*, **146**, 252 (2008).
10. J. Hao, Z. Lou, I. Renaud and M. Cocivera, *Thin Solid Films*, **467**, 182 (2004).
11. T. Minami, T. Miyata, S. Takata, I. Fukuda, *Jpn. J. Appl. Phys.*, **30**, L117 (1991).
12. J. P. Bender, J. F. Wager, J. Kissick, B. L. Clark and D. A. Keszler, *J. Lumin.*, **99**, 311 (2002).
13. G. Stuyven, P. D. Visschere, K. Neyts and A. Kitai, *J. Appl. Phys.*, **93**, 4622 (2003).
14. T. Miyata, T. Nakatani and T. Minami, *Thin solid films*, **373**, 145 (2000).
15. T. Minami, Y. Kobayashi, T. Miyata and M. Yamazaki, *Thin Solid Films*, **443**, 91 (2003).

16. T. Minami, Y. Kobayashi, T. Shirai, T. Miyata and S. Suzuki, *Jpn. J. Appl. Phys.*, **41**, L478 (2002).
17. T. Minami, H. Yamada, Y. Kubota and T. Miyata, *Jpn. J. Appl. Phys.*, **36**, L1191 (1997).
18. T. Minami, T. Nakatani, T. Miyata and T. Shirai, *Surf. Coat. Technol.*, **146 – 147**, 508 (2001).
19. T. Minami, M. Yamazaki, T. Miyata and T. Shirai, *Jpn. J. Appl. Phys.*, **40**, L864 (2001).
20. T. Minami, Y. Kobayashi, T. Miyata and S. Suzuki, *Jpn. J. Appl. Phys.*, **41**, L577 (2002).
21. T. Minami, T. Nakatani and T. Miyata, *J. Vac. Sci. Technol. A*, **18**, 1234 (2000).
22. S. Itoh, H. Toki, Y. Sato, K. Morimoto and T. Kishino, *J. Electrochem. Soc.*, **138**, 1509 (1991).
23. M. Flynn and A. H. Kitai, *J. Electrochem. Soc.*, **148**, H149 (2001).
24. T. Minami, T. Maeno, Y. Kuroi and S. Takata, *Jpn. J. Appl. Phys.*, **34**, L684 (1995).
25. M. Flynn and A. H. Kitai, *J. Appl. Phys.*, **97**, 094502 (2005).
26. T. Minami, H. Toda and T. Miyata, *J. Vac. Sci Technol. A*, **19**, 1742 (2001).
27. T. Minami, Y. Kuroi and S. Takata, *J. Vac. Sci Technol. A*, **14**, 1736 (1996).
28. J. F. Bender, M.S. thesis, Oregon State University, p.123, 2003.
29. Y. A. Ono, *Electroluminescent displays*, p.64, World scientific, Singapore, (1995).
30. P. Zalm, *Philips Res. Rep.*, **11**, 353 (1956).
31. P. Zalm, *Philips Res. Rep.*, **11**, 417 (1956).

32. V. Marello, L. Samuelson, A. Onton and W. Reuter, *J. Appl. Phys.*, **52**, 3590 (1981).
33. K. Okamoto and S. Miurs, *Appl. Phys. Lett.*, **49**, 1596 (1986).
34. T. Feng, M.S. thesis, University of Florida, p.105, 2001.
35. J. B. Gruber, B. Zandi, U. V. Valiev and Sh. A. Rakhimov, *J. Appl. Phys.*, **94**, 1030 (2003).
36. M. L. Pang, W. Y. Shen and J. Lin, *J. Appl. Phys.*, **97**, 033511 (2005).
37. J. C. Hitt and J. F. Wager, *J. Appl. Phys.* **90**, 2711 (2001).
38. L. E. Shea, R. K. Datta and J. J. Brown, Jr, *J. Electrochem. Soc.*, **141**, 2198 (1994).
39. Z. Hao, J. Zhang, X. Zhang, X. Sun, Y. Luo, S. Lu and X. J. Wang, *Appl. Phys. Lett.*, 90, 261113 (2007).
40. Y. E. Lee, D. P. Norton, J. D. Budai, C. M. Rouleau and J. W. Park, *J. Electroceram.*, **4**, 293 (2000).
41. S. S. Yi, J. S. Bae, B. K. Moon, J. H. Jeong, I. W. Kim and H. L. Park, *Appl. Phys. A*, **76**, 433 (2003).
42. Y. J. Kim, S. M. Chung, Y. H. Jeong and Y. E. Lee, *J. Vac. Sci. Technol. A*, **19**, 1095 (2001).
43. S. H. Yang, T. J. Hsueh and S. J. Chang, *Jpn. J. Appl. Phys.*, **46**, 4166 (2007).
44. S. Shih, P. D. Keir, J. F. Wager and J. Viljanen, *J. Appl. Phys.*, **78**, 5775 (1995).

Chapter 7

Summary and future recommendations

7.1. Summary

The luminescence of spinel structured oxides activated with transition and rare earth elements has been studied for many years. $ZnGa_2O_4$ received immense attention owing to its intrinsic blue emission character and high thermal stability that may lead to potential use in flat panel displays (FPDs). The present work focused on the deposition of transparent zinc gallate phosphor thin films at lower processing temperatures so as to promote the use of glass substrates in display applications.

Synthesis of a novel white phosphor:

Bulk phosphors were prepared by the conventional high temperature solid state reaction technique. The undoped $ZnGa_2O_4$ powder exhibited the spinel phase and could be synthesized without contamination by constituent oxides. It exhibited the self-activated blue emission characteristic of the material. A singly activated single phased white oxide phosphor - dysproium (Dy) doped $ZnGa_2O_4$ - was also identified. White phosphors do form an integral part of the solid state lighting industry as well as of white florescent screens for display applications. The use of a singly doped phosphor eliminates the inherent drawbacks exhibited by the conventionally used blue/UV LED's and multiphosphor/doubly activated phosphor blends to generate white light. Moreover, the development of a white phosphor that can be filtered to produce an RGB display has the advantage of maintaining the simple device fabrication sequence of a monochrome TFEL display (i.e., no patterning of the thin film phosphor or insulator layers) and

achieving RGB colors by laminating a patterned color filter to the EL device at the end of the process.

The luminescence mechanism in $ZnGa_2O_4:Dy^{3+}$ was proposed as the host to activator nonradiative resonant energy transfer, based on variations in the emission intensities of the Dy^{3+} ions and host lattice (sensitizer) with doping level. The doped samples exhibited the strong broad excitation band whose spectral profile matched well with that of the host. Also, the emission band of the sensitizer ions (here, Ga^{3+}) overlaps the parity forbidden absorption band of the activator (here, Dy^{3+}) ions, though to a small extent. The energy transfer efficiency was found to be a maximum for the sample synthesized with 2.5 at. % dopant concentration. The Dy^{3+} doped samples gave blue luminescence at and below 1 at. % as their spectra was more dominated by the host emission. Above 1 at. %, the samples exhibited white luminescence arising from the simultaneous occurrence of multicolor dopant emissions that dominated the emission spectrum. The 2.5 at. % doped sample also gave the best white emission with chromaticity coordinates (0.31, 0.33) matching well with that of achromatic white [(0.33, 0.33)]. Such sensitized luminescence is an important process in technological applications for luminescent materials. The luminescence of the $ZnGa_2O_4:Dy^{3+}$ samples could be tuned from blue to white by varying the dopant concentration.

Room temperature deposition of oxide phosphor films using PLD:

The undoped $ZnGa_2O_4$ phosphor thin films were grown using pulsed laser deposition (PLD) technique. The aim of the work was to grow refractory oxide

phosphor thin films at lower processing temperatures. So a technique was so chosen that could provide the adatoms enough energy at room temperature itself to assist film growth. The $ZnGa_2O_4$ target synthesized in the laboratory was ablated using the second harmonic (532 nm) of a Nd:YAG laser. The laser fluence and substrate to target distance were so optimized as to grow well adhesive thin films on fused silica substrates at room temperature. The ambient oxygen pressure was varied from 0.001 mbar to 0.01 mbar. The as-deposited films at lower oxygen pressures exhibited the secondary phase growth of β-Ga_2O_3. Single-phased films with (111) plane could be grown at 0.01 mbar. These films exhibited the blue luminescence, as that of bulk, with a blue shift in the emission spectrum due to the reduced crystal field effects at the distorted octahedral sites. Being a low voltage phosphor, the films gave an improved luminous output on post-deposition annealing in air. The growth of luminescent oxide phosphor thin films at room temperature itself would open up the possibilities of using the economical glass substrates during device fabrication.

White luminescence from $ZnGa_2O_4$:Dy^{3+} thin films:

With the intention of fabricating a device with $ZnGa_2O_4$:Dy^{3+} active layer, the commercial technique - rf magnetron sputtering - was used to deposit thin films of the same. Powder targets were synthesized. The dopant concentration was fixed at 2.5 at. %. The rf power, substrate to target distance and argon pressure were optimized at 125 W, 4.5 cm and 0.015 mbar respectively to grow transparent well-adhesive thin films of $ZnGa_2O_4$:Dy^{3+} on quartz substrates. The as-deposited films at room temperature were polycrystalline in nature but exhibited the main (311) peak of spinels. These films didn't, however, exhibit

any luminescent behavior. So substrates were heated prior to deposition in the range 100 - 700°C (in steps of 100°C) to improve the dopant incorporation. The films grown at and above the substrate temperature of 300°C gave the characteristic fluorescence transitions of the dopant ion. The maximum PL intensity was for the film deposited at 600°C whose chromaticity coordinates was (0.34, 0.28). All these films gave white luminescence with their CIE coordinates lying around achromatic white.

ACTFEL device fabrication on glass substrates:

Conventionally, ceramic substrates are used in device fabrication so that the luminescent response of the refractory active layer could be enhanced by high temperature processing after deposition. Such post-deposition treatments restrict the use of glass substrates in oxide phosphor based devices. In the present work, an alternating current driven thin film electroluminescent (ACTFEL) device was fabricated on commercial glass substrate with $ZnGa_2O_4:Dy^{3+}$ oxide phosphor as the active layer. The device - Glass/ITO/ATO/phosphor/$BaTa_2O_6$/Al - had the standard MISIM (metal-insulator-semiconductor-insulator-metal) structure instead of the inverted MISIM structure usually used for oxide phosphor based devices. The ACTFEL device gave a white EL emission, the intensity of which increased with applying voltage. The EL emission could further be improved in intensity by inserting a highly crystallized interfacial layer of ZnO between the substrate and the phosphor layer. Both the devices obeyed the luminance-voltage relation. The step in their L-V curves denotes the build-up of space charge in the device. The use of glass substrates would promote the fabrication from an industrial viewpoint to meet the demands at the consumer end.

7.2. Recommendations for future work

The $ZnGa_2O_4:Dy^{3+}$ phosphor material can be excited only below 300 nm. This property can be utilized to use it for secret encryptions transparent under visible light and luminescent under far-UV for military applications.

The PLD work can be extended with the higher harmonics of Nd:YAG laser to deposit $ZnGa_2O_4$ films with (311) peak at low processing temperatures. It has been reported that device fabrication is possible on glass substrates using PLD technique also. So one can even explore this technique for activated zinc gallate phosphor materials. The use of amorphous transparent electrodes like InGaZnO also can be tried for transparent display applications. A further increase in the luminescent intensity - both PL and EL response - can be had if one uses mosaic targets for film growth instead of stoichiometric targets to control the Zn/Ga stoichiometry in the $ZnGa_2O_4$ films. The addition of flux materials like Li in the target would also enhance the luminescent output. The dopant concentrations could be varied in the target to study the effect on the EL response. The physics of the device can better be understood by exploring its electrical characteristics.

Today, a number of high temperature plastics are commercially available for use as substrates. An eye should be kept on these materials so as to promote the use of these high temperature transparent plastic substrates with low coefficients of thermal expansion for ACTFEL device fabrications.